Title	顕微ナノメカニックス計測法による金ナノ接点の弾性・塑性応答の解析
Author(s)	劉, 佳明
Citation	
Issue Date	2025-03
Type	Thesis or Dissertation
Text version	ETD
URL	http://hdl.handle.net/10119/19943
Rights	
Description	Supervisor: 大島 義文, 先端科学技術研究科, 博士

Doctoral Dissertation

Study of elastic and plastic responses of gold nanocontacts using microscopic nanomechanical measurement method

Liu Jiaming

Supervisor Oshima Yoshifumi

Graduate School of Advanced Science and Technology
Japan Advanced Institute of Science and Technology
(Materials Science)

March 2025

Abstract

In this thesis, the elastic and plastic responses of gold nanocontacts (NC) was invesgated by microscopic nanomechanical measurement method (MNMM). Specifically, for the elastic response, we estimated the local Young's modulus of the internal local regions of the Au NCs. For the plastic response, we estimated the critical resolved shear stress (CRSS) required for slip to occur in the Au NCs. The Au NCs were fabricated using our developed in situ TEM holder, which is equipped with a quartz length-extension resonator (LER) as a force sensor for directly evaluating the force gradient (spring constant).

For nanocrystals, the Young's modulus exhibits both orientation dependence and size dependence. In devices made from nanomaterials, distribution of local Young's modulus is non-uniform. It is important to measure the local Young's modulus of nanocrystals. Our approach is based on the idea that under uniform shape and size conditions, a material with uniform Young's modulus will undergo uniform deformation under stress. However, if the Young's modulus is non-uniform, the deformation in different regions will vary. By measuring the local strain and its ratio to the overall strain, we can estimate the local Young's modulus for each region. Using our self-developed in situ TEM holder, we stretched Au NCs and observed their crystal structure through TEM, precisely measured the evolution of lattice spacing to obtain the local strain. Notably, the pixel size of the CCD we use is approximately 25 pm, while the maximum elastic elongation of the Au lattice is less than 10 pm, much smaller than the size of a single pixel. As a result, traditional methods cannot capture the stretching of the Au lattice. We fully utilized the large number of pixels in the TEM images and assumed that the TEM intensity follows a Gaussian distribution, enabling sub-pixel measurement of the Au lattice positions. In this way, we obtained the elongation of local regions during stretching. Additionally, we directly measured the force gradient (spring constant) applied to the Au NCs using FM method, and with the geometric information observed from TEM, we successfully estimated the local

Young's modulus and studied its size dependence.

When the amount of stretching exceeds the material's elastic limit, it transitions from elastic deformation to plastic deformation. In nanocrystals, plastic deformation primarily occurs in the form of slip, and the necessary shear stress required for slip to occur in the slip direction is called as the CRSS. For bulk materials, the yield limit can be estimated by measuring the stress-strain curve. However, for nanomaterials, both stress and strain are extremely small, making direct measurement very difficult. We captured the energy dissipation associated with plastic deformation to estimate the maximum elastic deformation of Au NCs. Using the geometric information observed through TEM and the mechanical response obtained from FM method, we estimated the yield stress of Au nanocontacts with various size and orientation. For [110] Au NCs, with conductance values of 60 G_0 and 30 G_0, the yield stress was $2.0 \pm 0.1\ GPa$, regardless of size. In contrast, for [111] Au NCs with conductance of 30 G_0, the yield stress was $3.0 \pm 0.1\ GPa$. Considering the partial slip system in FCC metals, we found that the Schmid factor for [110] direction Au nanocontacts is $\sqrt{2}/3$ (≈ 0.47), the CRSS was calculated to be $0.94 \pm 0.1\ GPa$. Similarly, for [111] direction Au nanocontacts, the Schmid factor is $2\sqrt{2}/9$ (≈ 0.31), yielding an estimated CRSS of $0.94 \pm 0.1\ GPa$. These two results are consistent. Therefore, we conclude that the CRSS for the $\{11\bar{1}\}$<112> slip system in Au NCs is $0.94 \pm 0.1\ GPa$.

In conclusion, a method for estimating the elastic and plastic responses of nanomaterials has been proposed. We studied Au NCs as an example, and our results had shown unique properties from bulk Au. This method is expected to be improved by introducing aberration-correct device to obtain better TEM resolution. The understanding of mechanics in atomic scale provide essential information for fundamental understanding and applications such as atomic scale nanodevices.

Keywords: nanomechanical, in-situ TEM, local Young's modulus, CRSS, dissipation energy.

Contents

Chapter 1 Introduction

Introduction

This chapter introduces the background of this study. Section 1.1 presents the unique properties of nanomaterials and explains the necessity of studying mechanical properties at the nanoscale. Due to limitations in experimental techniques, early studies on the mechanical properties of nanomaterials were demined in theoretical and simulation levels. Section 1.2 reviews previous experimental studies on the mechanical properties of nanomaterials, highlighting advancements and limitations in previous experimental methods, and discusses the advantages and necessity of using in situ measurement techniques.

1.1 Mechanical properties of nanomaterials

Nanomaterials (particularly with sizes below 10 nm) have attracted wide attention due to their potential in nanoscience and nanotechnology[1–3]. Nanomaterials are reported to have unique and novel physical and chemical properties, such as high stiffness, orientation dependency, excellent thermal and electrical conductivity[4–8]. These unique properties of nanomaterials have given them potential in applications as functional components in catalysts and nanoelectromechanical systems (NEMS) and so on[8–10]. Among these unique properties, the mechanical properties of nanomaterials have garnered significant attention due to their properties can be modulated by strain or stress during their application. However, the mechanisms behind the unique mechanical properties of nanomaterials, particularly how their properties are modulated, still remain unclear. Having a deeper understanding of the mechanical properties of nanomaterials is crucial for the design and optimization of nanoscale devices. The nanomaterials have a very high surface-to-volume ratio and ultra small size, leading to surface effects and quantum confinement effect. Therefore, different with bulk counterparts, the nanomaterials show very unique and unpredictable mechanical properties, and have attracted significant research interest. In the early stage, due to the limitation of experimental technology, simulation and computational methods dominate the research on nanomaterials [11–15]. The deformation mechanisms of metallic nanowires with diameters smaller than 100 nm were analyzed using first-principles calculations and molecular dynamics methods. The study revealed that nanowires can deform through various ways, such as slip via perfect dislocation, partial dislocation, and the formation of deformation twins. The competition among these deformation ways is primarily governed by the Schmid factor and material properties. These simulations demonstrated that metallic nanomaterials exhibit exceptionally high strength, and predicted theoretically that their strength may have a significant dependence on temperature and geometry[15]. However, the conclusions obtained from simulations and calculations are strongly dependent on the choice of models and parameters, and differing selections may even lead to opposite results. Zhou et al. studied the Young's modulus of copper (Cu) as an example of face-center-cube (FCC) metal with different approaches, and their results have shown oppsite size dependency (as shown in Figure 1.1): when using embedded atom method (EAM), the Young's modulus decrease while reducing the size; however, in the case that using Lennard-Jones (L-J) potential, the Young's modulus increases with size decreased[16]. This highlights the emergency need for reliable experimental evidence to clear these conflics.

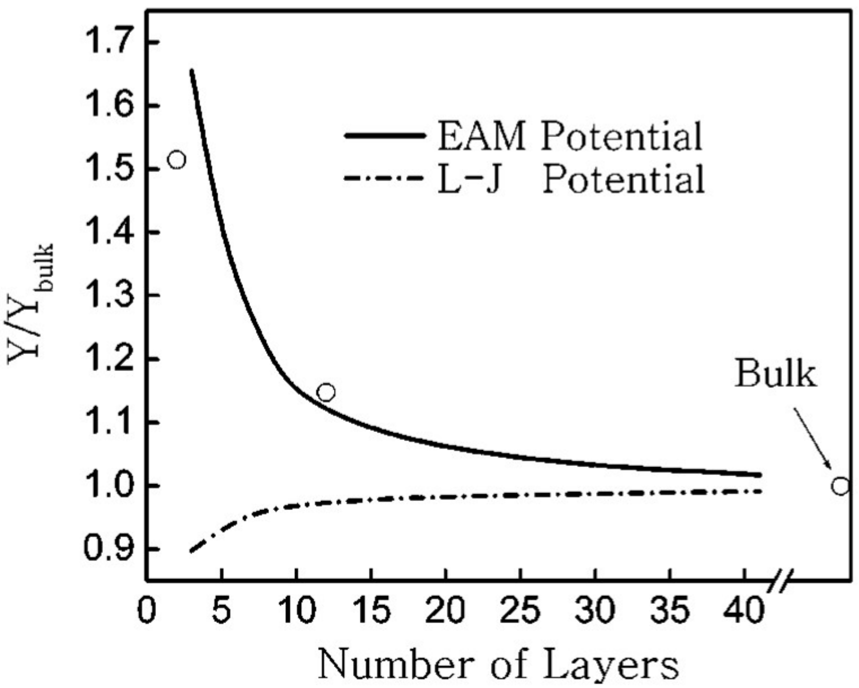

Figure 1.1 Zhou et al. obtained oppsite size denpency of Young's modulus by choosing embedded atom method (EAM) potential and Lennard-Jones (L-J) potential[16].

1.2 Previous experimental studies on the mechanical properties of nanomaterials

With the development of advanced microscopy techniques such as scanning electron microscopy (SEM), atomic force microscopy (AFM), and transmission electron microscopy (TEM), experimental attempts to study the properties of nanomaterials have appeared[17–21]. Greer et al. studied the mechanical properties of Au nanopillars with diameters of hundreds of nanometers[22]. As illustrated in Figure 1.2 (a), they grew [001]-oriented Au on a MgO substrate and fabricated the Au nanopillars using focused ion beam (FIB) milling. They performed uniaxial compression tests on the nanopillars using a flat punch and measured the compressive stress, strain, and stiffness of the pillars. Their results, as shown in Figure 1.2 (b), revealed a size-dependent stiffness, indicating that the stiffness of the nanopillars increases as their diameter decreases.

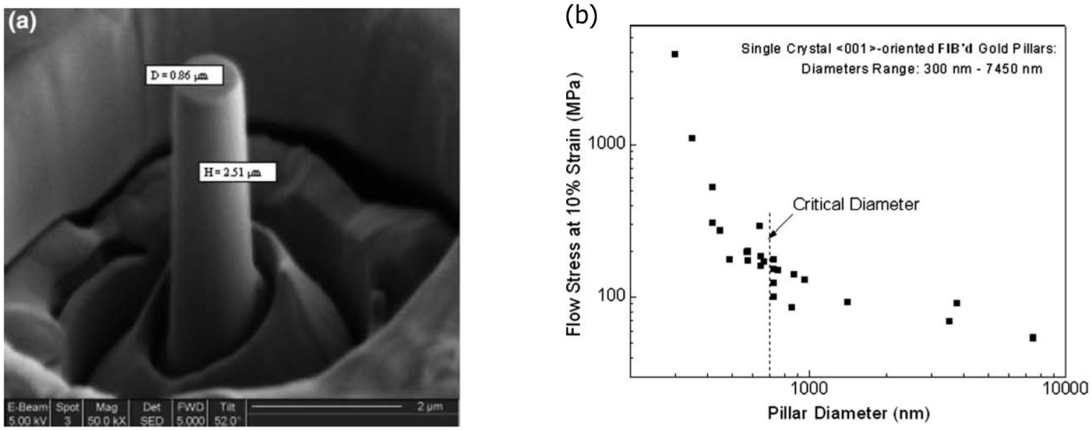

Figure 1.2 (a) SEM image of the Au nanopillar. (b) Size dependency of stiffness by Greer et al.[22].

Wu et al. investigated Au nanowires with diameters ranging from 40 to 250 nm using an AFM-based method[23]. In their experiments, both ends of nanowires are fixed, a cantilever was used to bend the nanowires at their midpoint. Their results showed that the Young’s modulus of the Au nanowires is independent of the diameter within this size range, as shown in Figure 1.3. Hoffmann et al. investigated the mechanical strength of silicon (Si) nanowires grown by the vapor−liquid−solid (VLS) method[24]. These nanowires had diameters ranging from 100 to 200 nm and a typical length of 2 μm. In the experiments, one end of the silicon nanowires was fixed to the grown substrate, and an AFM tip applied a load to the free end, bending the nanowires. The study revealed that the average strength was approximately 12 GPa, which corresponds to 6% of the Young's modulus of Si along the nanowire direction.

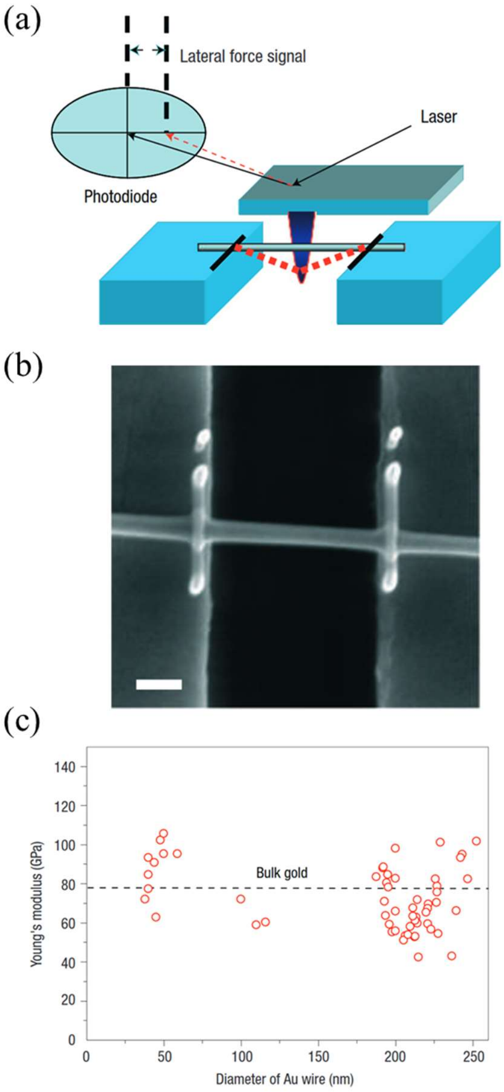

Figure 1.3 (a) Schematic of fixed wire in a lateral bending test with an AFM tip by Wu et al. (b) SEM image of a Au nanowire secured by Pt lines deposited through electron-beam-induced deposition, with scale bars of 500 nm. (c) Young's modulus values measured for Au nanowires ranging from 40 nm to 250 nm in diameter[23].

For nanomaterials with dimensions below 100 nm, direct force measurement remains challenging. Previous studies utilized an integrated TEM-AFM system based on Si cantilevers to estimate the loading force on nanowires. Y. Lu et al. developed a TEM specimen holder to perform in situ tensile testing on Au nanowires (Figure 1.5)[25]. During nanowire elongation, AFM probe deflection was employed to quantify the loading force, while TEM imaging simultaneously captured real-time structure evolution. The strain-stress curve was obtained during the tensile testing. However, the force measurement was relay on the deformation of Si cantilever, due to the individual variation in the cantilever's Young’s modulus, the measurement accuracy is low for microforces at the nN level.

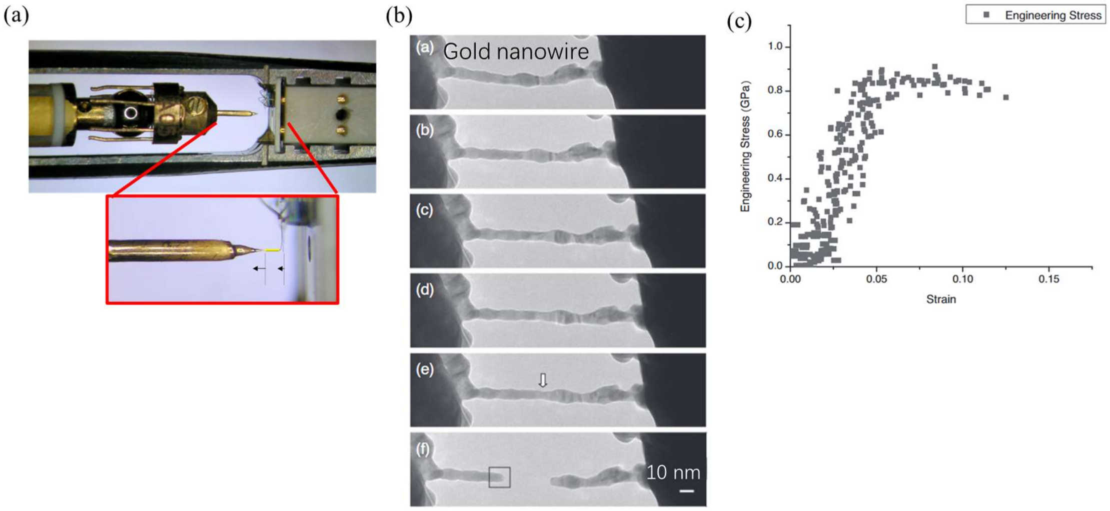

Figure 1.4 (a) TEM combined with AFM based on Si-cantilever. (b)TEM images of Au nanowire during the tensile test. (c) Strain-stress curve of Au nanowire[25].

TEM (or SEM) combined with Micromechanical Devices (MMDs) has also been applied in experimental approaches for loading force measurement. As shown in Figure 1.5(a), Zhang et al. developed a pull-to-push chip, where a Si nanowire was placed across a gap in the chip[26]. By pressing the chip with a punch, the gap widened, stretching the Si nanowire. As shown in Figure 1.5(b), the tensile process of the Si nanowire can be observed using TEM. In their experiment, the Si nanowires had a diameter of approximately 100 nm. This method is applicable not only under SEM but also under an optical microscope. However, due to the significant height difference between the chip gaps (typically >100 nm), this effect becomes non-negligible for smaller samples (Figure 1.5(c)). Therefore, more suitable mechanical measurement methods are required for samples at the tens of nanometers or even nanometer scale.

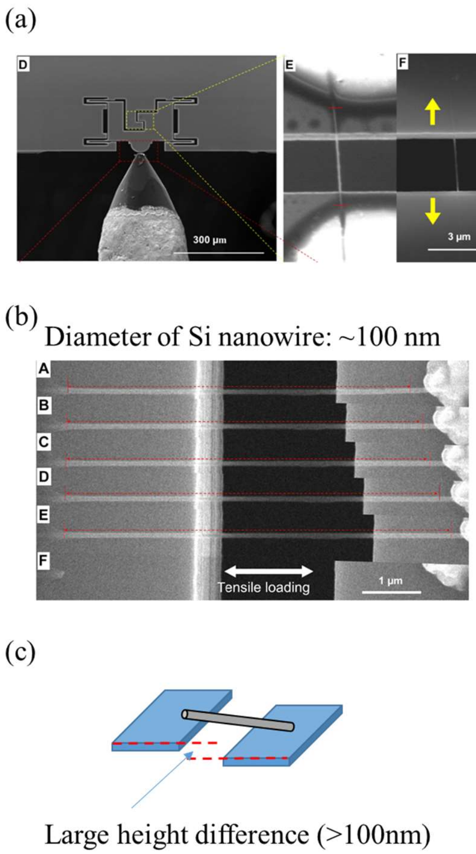

Figure 1.5 (a) Pull-to-push chip with a Si nanowire was placed across a gap in the chip. (b)TEM images of tensile process of Si nanowire[26]. (c) Schematic diagram of the chip gap height difference.

1.3 Purpose

The purpose of this study is to investigate the mechanical response of Au nanocontacts, including both elastic and plastic response. As shown in the figure, the two localized regions within the red box exhibit significant size differences. Due to the size effect in nanomaterials, I hypothesize that these regions have different local Young’s moduli. Estimating the local Young’s modulus is crucial for the design of nano-devices, such as NEMS. Therefore, the first purpose of this study is to estimate the local Young’s modulus of nanomaterials.

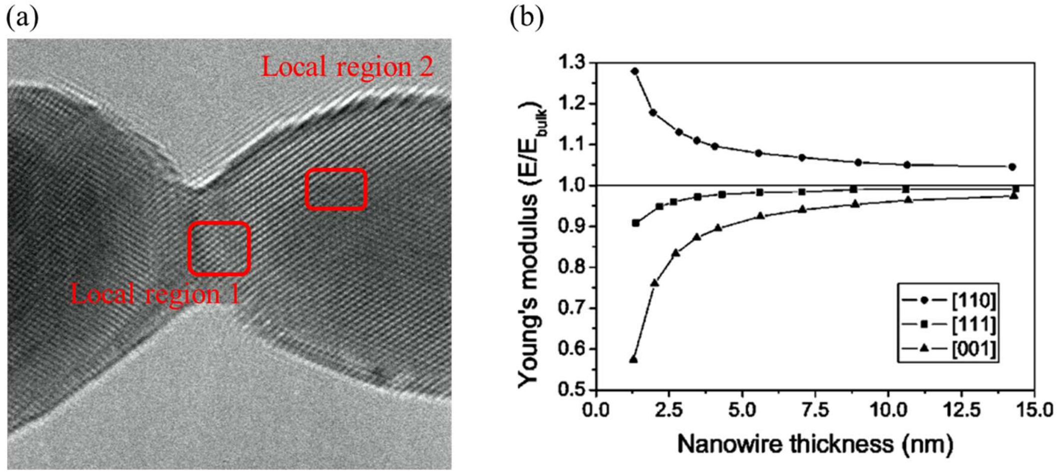

Figure 1.6 (a) One non-uniform size specimen. (b) Size effect on nanomaterials[27].

Figure 1.7(a) shows a typical strain-stress curve of metal materials. After reaching the yield stress, it starts to have plastic deformation. For the case of FCC crystals, slip always occurs on the {111} atomic planes once the loading stress exceeds the elastic limit, regardless of the loading direction (Figure 1.7(b)). Whether plastic deformation takes place depends on whether the resolved shear stress on the slip plane reaches the critical threshold. The critical resolved shear stress (CRSS) is defined as the necessary stress in the slip direction to initiate slip deformation. The second objective of this study is to measure the CRSS of Au nanomaterials.

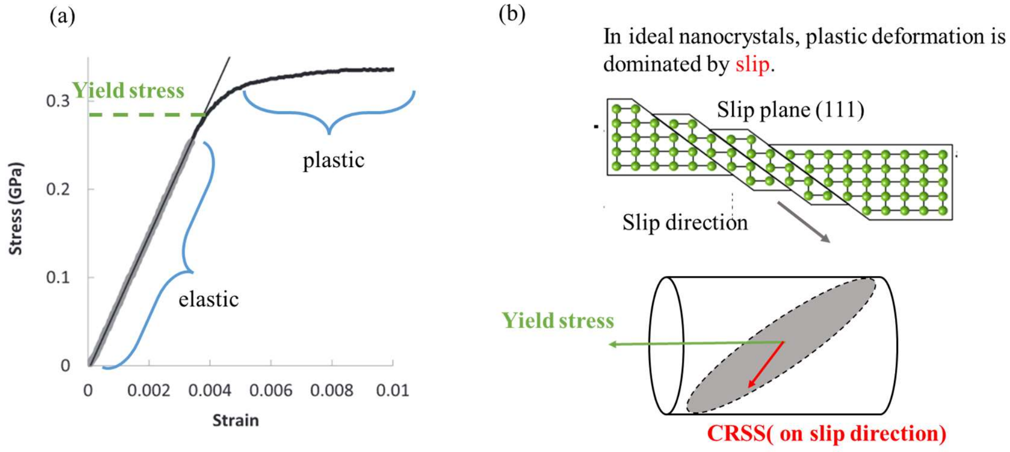

Figure 1.7 (a) A typical strain-stress curve of metal[28]. (b) Size effect on nanomaterials.

Chapter 2 Methodology

Introduction

This chapter introduces the experimental methods and principles. Section 2.1 discusses the birth of TEM, its importance in nanoscience research, as well as its structure and operating mode. Section 2.2 explains the principle and experimental setup for using the FM method to directly measure the sample's spring constant (force gradient). Section 2.3 introduces the method for capturing energy dissipation in nanocrystals during deformation. By modeling the interaction of the sample with the LER sensor as an external force, the non-conservative force components during the oscillation process are considered as the source of energy dissipation. Energy dissipation is directly captured through changes in the driving voltage used to excite the LER oscillation. Section 2.5 describes the working principle of the phase-locked loop used to control LER oscillation.

2.1 Transmission electron microscopy (TEM)

The invention of the optical microscope greatly advanced the study of cells, bacteria, and physiological functions of the human body. However, by the 1920s, the optical microscope could no longer meet the research needs. An optical microscope can achieve a magnification of approximately x500 to x1000 by improving the quality of optical lenses, but cannot achieve the magnification of x2000. This limitation is due to the fact that the magnification of conventional optical microscopes is restricted by the wavelength of visible light. Optical microscopes use visible light to observe objects. According to theoretical calculation, the resolution of a conventional optical microscope does not exceed 200 μm. Researchers improved resolution by reducing the wavelength of the light source, such as using ultraviolet rays as beam source. They developed ultraviolet microscopes, however, the magnification is only about two to three times that of conventional optical microscopes. To study the structure of materials at a higher level, it is necessary to create microscopes with higher resolution.

In 1927, de Broglie published a paper revealing the wave nature of electrons, showing that the electrons are also a light with wavelength of is several orders of magnitude smaller than that of visible light[29,30]. This discovery inspired the exploration of using electrons as a light source, leading to a rapid surge in related applications. The Transmission Electron Microscope (TEM) uses electron beams instead of visible light as its light source, achieving a magnification of 1 million times with an acceleration voltage of 200 kV. TEM is an essential tool for evaluating nanometer-scale materials and is widely used in understanding the physical properties of nanomaterials such as semiconductors, biomaterials, and metals.

Since its invention in the 1930s, the TEM has undergone significant improvements and functional advancements. By the 2000s, the invention of spherical aberration correction equipment allowed TEM to achieve atomic-level resolution. Recently, techniques have been developed to install force sensors, such as cantilevers and AFM probes into specimen holders, enabling simultaneous mechanical measurement while observating specimen structures. The main purpose of using TEM in this study is to obtain real-space images to understand the crystal structure of specimens. TEM can also be used to obtain electron diffraction images of periodic regions, as well as to observe in situ chemical reactions and biological materials.

2.1.1 Structure of Transmission Electron Microscope (TEM)

In an electron microscope, instead of visible light, electron beams emitted from an electron gun, and these beams are focused by electromagnetic lenses to adjust the light path to focus on the specimen. The electron gun can be categorized based on the method of electron emission into types such as thermionic emission, field emission, thermal field emission, and Schottky emission.

A thermionic emission electron gun heats a cathode, such as tungsten or LaB_6, to release thermal electrons. For field emission electron gun, places a sharply pointed tungsten cathode in a strong electric field, utilizing the tunneling effect to emit electrons from the cathode tip. Field emission guns have advantages over thermionic emission guns, offering lower current levels and higher brightness. Furthermore, electrons are emitted from a tiny area on the cathode, resulting in minimal variation in initial velocity, so the electron beam has a stable wave length, this can improve the imaging resolution.

For the Schottky electron gun, by heating the emitter to a temperature lower than that required for effective thermionic emission (~1800 K) while applying a strong electric field to have the Schottky effect to release electrons. Generally, for the thermionic emission, Schottky, and field emission electron guns, the brightness increases with both the electron energy width and beam diameter decrease.

The electron beam used in TEM is typically accelerated by a voltage ranging from tens to hundreds of kV. Similar to optical microscopes, the image resolution of a TEM can be approximated by the following Rayleigh criterion[31]:

$$g(x) = \frac{\omega}{2\pi} \int_{-\frac{\pi}{\omega}}^{\frac{\pi}{\omega}} f(x - x') d\mathrm{t} \qquad 2.1$$

Here, λ represents the wavelength of the electron beam, μ is the refractive index of the medium, and β is the acceptance angle of the objective lens. Since Equation (2.1) represents the resolution limit, a smaller λ results in higher image resolution. In the case of a TEM with an accelerating voltage of 200 kV, the wavelength of the electron beam is 0.00251 nm, which is shorter than the diameter of an atom, thereby achieving atomic-scale resolution.

As shown in Figure 2.1, a comparison is made between the structure of a typical TEM[32] (Figure 2.1(a)) and that of an optical microscope (Figure 2.1(b)). A typical TEM consists of an electron gun, a vacuum system, electromagnetic lenses, a goniometer, apertures, and an image recording system.

The electron gun acts as the source of the electron beam. The vacuum system is used to maintain a high vacuum in the TEM chamber, reducing the effect of gas molecules on both the electrons (by increasing their mean free path) and the specimens (by minimizing electron-beam-induced deposition). The electromagnetic lenses in the TEM are used for electron focusing and, as shown in Figure 2.1 (a), are divided into condenser lenses, objective lenses, intermediate lenses, and projector lenses.

The goniometer is used to fix the sample holder within the TEM chamber and allows mechanical movement of the sample in three axes, enabling the generation of the image or diffraction pattern of the sample through the objective lens. Various types of sample holders can be inserted into the goniometer. Apertures are used to filter the electron beam, and the image recording system is used to capture the image generated by the electrons.

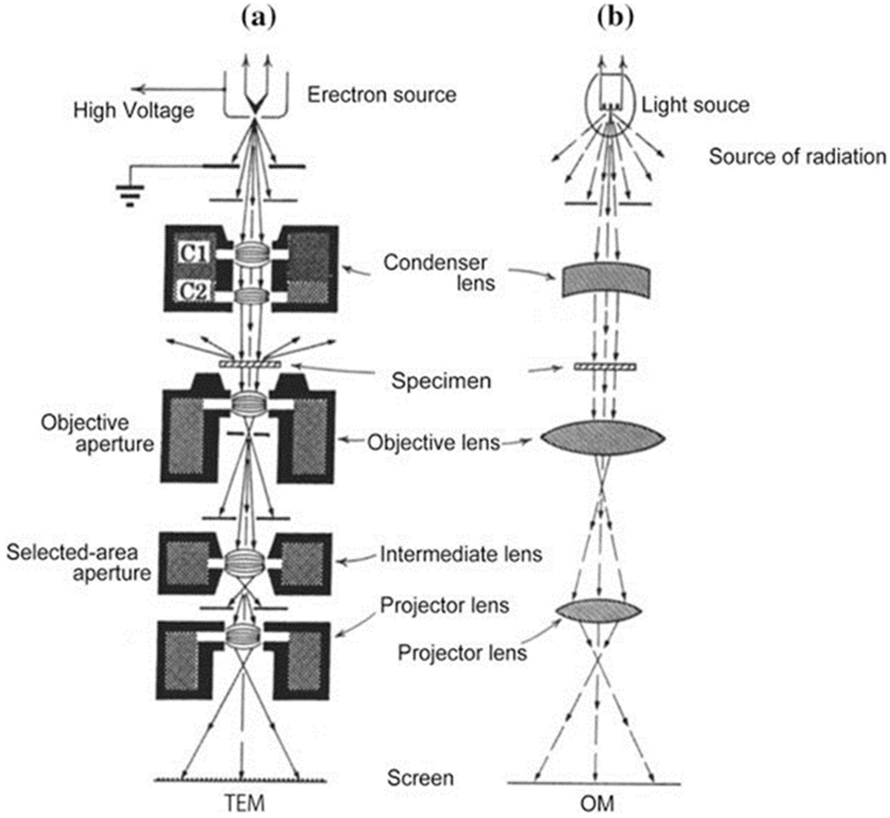

Figure 2.1(a) Schematic structure of a typical TEM. (b) Schematic structure of a typical optical microscope.

2.1.2 TEM Imaging Modes

TEM imaging is performed using transmitted electrons. The basic imaging process is as follows:

i. The electron gun emits and accelerates electrons, which are then focused by the condenser lenses.

ii. The incident electrons interact with the sample, with some electrons passing through or being scattered by the sample.

iii. These transmitted/scattered electrons are focused by the objective lens, and with the assistance of intermediate and projector lenses, a TEM image is obtained.

TEM has two operating modes, imaging mode and diffraction mode, as shown in Figure 2.2(a) and (b). The diffraction pattern is formed on the back focal plane by the objective lens, while the image is generated on the image plane (referred to as the intermediate image). The focus of the intermediate lens can adjust the image or diffraction pattern shown on the second intermediate image, and then it can be magnified by the projection lens. Therefore, imaging and diffraction modes are controlled by the intermediate lens. Finally, the image or diffraction pattern is displayed on a screen and recorded by a camera. In this study, TEM images representing the atomic structure of the sample are obtained using the imaging mode and recorded with a CCD camera.

For obtaining the atomic structure of the sample, high-resolution transmission electron microscopy (HR-TEM) is used in the experiment. The imaging contrast of HR-TEM is caused by the interference between the scattered electron wave and the transmitted electron wave. When the sample is extremely thin, the amplitude of the incident electron wave does not change, but the phase of the wave slightly changes after interaction. In this case, the interaction between the sample and the incident electron wave, along with the interference of the transmitted electron wave, results in a phase shift. This phase shift is relative to the peak of the incident wave at the position of the atomic columns. By recording the amplitude of the phase interference, HR-TEM images are captured with a CCD camera, representing the projected structure of the sample.

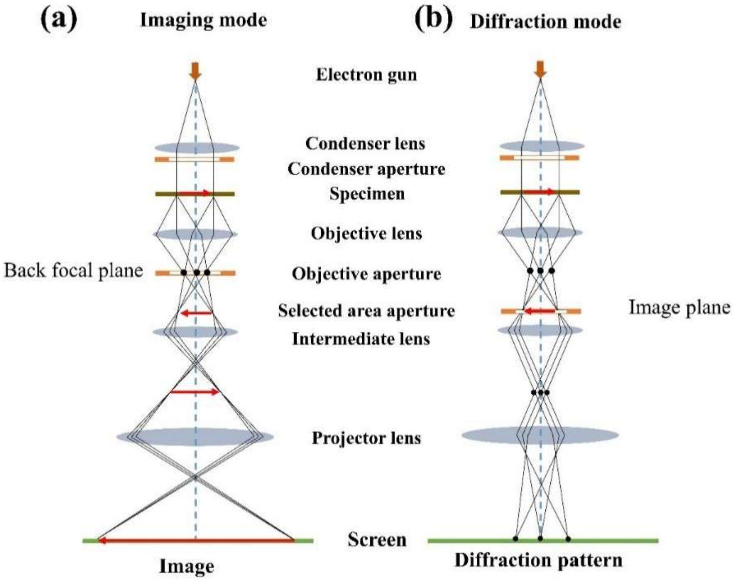

Figure 2.2 (a) Imaging mode of TEM. (b) Diffraction mode. By adjusting the intermediate lens, the imaging or diffraction pattern is displayed on the plane of the second intermediate image when the imaging or diffraction mode is adjusted.

2.2 Method for measuring spring constant

In this study, we used a Length Extension Resonator (LER) as mechanical sensor to detect mechanical responses based on the Frequency Modulation (FM) method. LER has high spring constant of 10^5 N/m, so it can be oscillated with a low oscillation amplitude of about 30pm. With such low amplitude, the TEM image will not be blurred due to LER oscillation. The LER used in this study is a STATEK (3EXW-1073) model (as shown in Figure 2.3), with a spring constant of approximately $9.2\times1059.2\times10^5$ N/m per rod and a resonance frequency around 1 MHz.

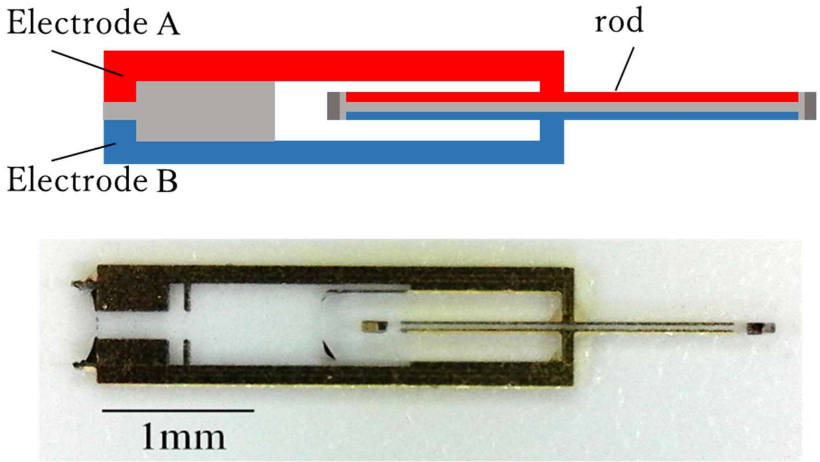

Figure 2.3 Illustration and photograph of the Length Extension Resonator (LER).

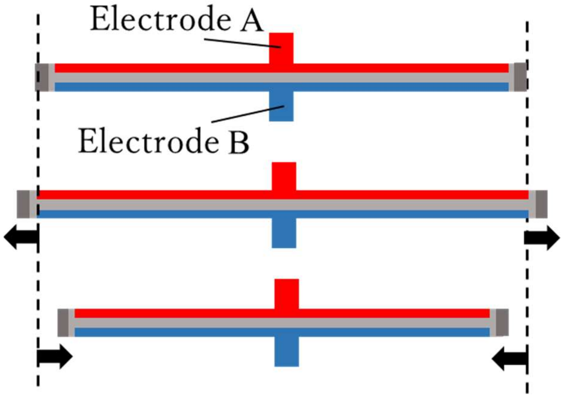

Figure 2.4 Schematic of the LER rod oscillation.

The rod-shaped resonator (approximately 2.7 mm in length) in LER is made of quartz and serves as the actual oscillate part. On both sides of the rod, gold electrodes are deposited so we can apply voltage on it. Hereafter, this rod-shaped resonator will be referred to as the "rod." Since quartz is spontaneously polarized, it exhibits the (inverse) piezoelectric effect. As shown in Figure 2.3, the gold electrode on both sides of the rod is the same, here we call them as Electrode A and Electrode B depending on their function. Electrode A is used for electrical excitation; when an AC voltage is applied, the inverse piezoelectric effect causes the polarized quartz lattice to experience an electric field force, generating stress along the rod axis. Consequently, the rod deformed in the frequency of the applied voltage (as shown in Figure 2.4). Due to this deformation of the rod, induced charges appear on Electrode B. This induced charge is proportional to the oscillation amplitude (in length). We measured the oscillation amplitude in experiment, and studied relationship between it to this induced charge on Electrode B. Detailed methods are provided in Chapter 3.

Next, we will use an oscillation model to explain the principle of using the LER as a sensor to measure the spring constant of the sample through the FM method.

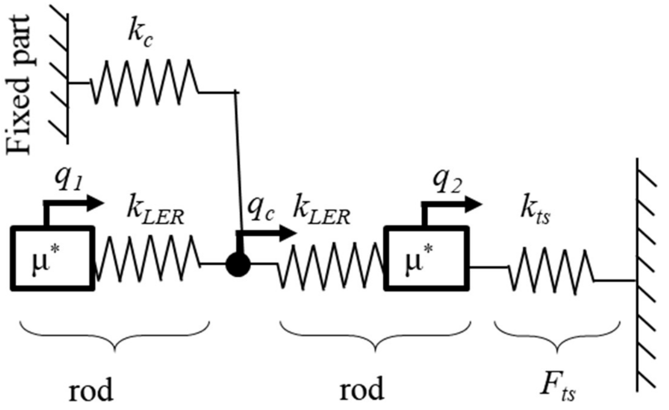

Figure 2.5 Oscillation model of LER rod.

Consider the oscillation model of the LER shown in Figure 2.5. Let the spring constant (force-displacement gradient) of the support at the center of the rod be k_c, and its displacement from the equilibrium position be q_c. The displacements of the two rods from their equilibrium positions are q_1 and q_2. The spring constant and effective mass of each rod are represented as k_{LER} and μ^*, respectively. An external force F_{ts} acts on the left rod, with a displacement gradient k_{ts}. As will be discussed later, if a metallic NC is attached there, this gradient corresponds to the equivalent spring constant of the metallic NC. From this model, we can derive following equations of oscillation:

$$\begin{cases} \mu^* \dfrac{\partial^2 q_1}{\partial t^2} = -k_{ts} q_1 - k_{LER}(q_1 - q_C) \\ \mu^* \dfrac{\partial^2 q_2}{\partial t^2} = -k_{LER}(q_2 - q_C) \end{cases} \qquad 2.2$$

Considering the force balance at the central point c, the following relationship can be obtained:

$$-k_C q_C = -k_{LER}(q_1 - q_C) - k_{LER}(q_2 - q_C)$$

$$q_C = \frac{q_1 - q_2}{2 + \dfrac{k_C}{k_{LER}}} \qquad 2.3$$

κ is defined as follow:

$$\kappa = \frac{1}{2 + \dfrac{k_C}{k_{LER}}} \qquad 2.4$$

then we can obtain $\omega_0^2 = \frac{k_{LER}}{\mu^*}$, and equation (2.2) can be rewritten as:

$$\begin{cases} \dfrac{\partial^2 q_1}{\partial t^2} = -\omega_0^2 \left(\dfrac{k_{ts}}{k_{LER}} + 1 - \kappa\right) q_1 + \omega_0^2 \kappa q_2 \\ \dfrac{\partial^2 q_2}{\partial t^2} = \omega_0^2 \kappa q_1 - \omega_0^2 (1 - \kappa) q_2 \end{cases} \qquad 2.5$$

here, if we make the following definitions:

$$\boldsymbol{M} \equiv \omega_0^2 \begin{pmatrix} \dfrac{k_{ts}}{k_{LER}} + 1 - \kappa & -\kappa \\ -\kappa & 1 - \kappa \end{pmatrix} \qquad 2.6$$

$$\boldsymbol{Q} \equiv \begin{pmatrix} q_1 \\ q_2 \end{pmatrix} \tag{2.7}$$

then, equation (2.5) can be expressed in matrix form as follows:

$$\frac{\partial^2}{\partial t^2}\boldsymbol{Q} = -\boldsymbol{M}\boldsymbol{Q} \tag{2.8}$$

assuming the displacement of the rods follows simple harmonic oscillation, it can be expressed as $q_i = A\cos(\omega_i t - \phi_i)$. Furthermore, if the frequencies of the two rods are same, i.e., $-\omega = \omega_1 = \omega_2$, then we have:

$$\frac{\partial^2}{\partial t^2}\boldsymbol{Q} = -\omega^2\boldsymbol{Q} = -\boldsymbol{M}\boldsymbol{Q} \tag{2.9}$$

Therefore, ω^2 is the eigenvalue of $\boldsymbol{M}$ with $\boldsymbol{Q}$ as the eigenvector. From det $\det(\boldsymbol{M} - \omega^2\boldsymbol{E}) = 0$, we obtain:

$$\begin{vmatrix} \frac{k_{ts}}{k_{LER}} + 1 - \kappa - \frac{\omega^2}{\omega_0^2} & -\kappa \\ -\kappa & 1 - \kappa - \frac{\omega^2}{\omega_0^2} \end{vmatrix} = 0 \tag{2.10}$$

$$\omega_\pm^2 = \omega_0^2\left\{\left(\frac{k_{ts}}{k_{LER}} + 1 - \kappa\right) \pm \sqrt{(\frac{k_{ts}}{k_{LER}})^2 + \kappa^2}\right\} \tag{2.11}$$

The frequencies indicated by the plus and minus signs correspond to the resonant oscillate in opposite phase and in phase, respectively. In the limit of $k_{ts} \to 0$, $\omega_+^2 = \omega_0^2$, $\omega_-^2 = (1 - 2\kappa)\omega_0^2$. κ including the spring constant k_c of the beams fixing part appears only in the solution of the same phase. This is because when the beam vibrates in the opposite phase, the force applied to the fixing part is canceled. Since the oscillation of the opposite phase is used in this study, $\omega_{\mp}^2$ is expressed as ω^2 and will be discussed below. When the spring constant of the beam is sufficiently larger than the spring constant of the external force ($k_{LER} \gg k_{ts}$), we can obtain:

$$\omega^2 \approx \omega_0^2 \left\{ \left(\frac{k_{ts}}{2k_{LER}} + 1 - \kappa \right) + \kappa \right\} = \omega_0^2 \left(\frac{k_{ts}}{2k_{LER}} + 1 \right)$$

$$\omega \approx \omega_0 \left(\frac{k_{ts}}{4k_{LER}} + 1 \right) \qquad 2.12$$

Therefore, the relationship between the external force gradient (equivalent spring constant) k_{ts} and the frequency shift of the LER Δf is expressed as follows:

$$\Delta f = \frac{1}{2\pi}(\omega - \omega_0) = \frac{k_{ts}}{2 \times 2k_{LER}} f_0 \qquad 2.13$$

The effective spring constant of the LER is shown to be 2 time of the equivalent spring constant of one rod.

2.3 Method for measuring energy dissipation

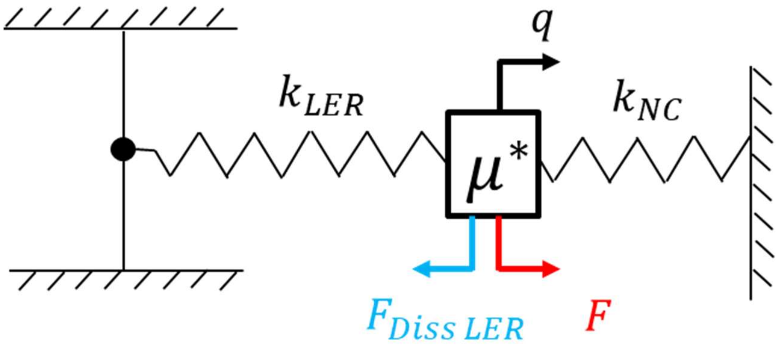

Figure 2.6 LER oscillation model.

To estimate the energy dissipation caused by internal friction within the LER and our specimen NC, we considered the model shown in Figure 2.6. For simplicity, we focus on the left rod of the LER to which the NC is connetcted. Let q represent the displacement of the rod from its equilibrium position on the left side, with μ^* denoting effective mass. Here, k_{LER} and k_{NC} are the spring constant of the LER and NC, respectively. $F_{Diss\ \ LER}$ (in blue color) is the dissipative force inside the LER due to internal friction. F (in red color) is the force that driving the LER oscillation, it is caused by the driving voltage. From this model, we derived the following motion equation:

$$\mu^* \frac{\partial^2 q}{\partial t^2} + k_{LER} q + k_{NC} q + F_{Diss\ \ LER} \quad = F \qquad 2.14$$

Generally, the energy dissipation $Diss_{LER}$ produced in one oscillation cycle can be estimated by the integral of F with respect to displacement q:

$$\begin{aligned} Diss_{LER} &= \oint F\,dq \\ &= \oint \mu^* \frac{\partial^2 q}{\partial t^2} + k_{LER} q + k_{NC} q + F_{Diss\ \ LER}\, dq \\ &= \oint F_{Diss\ \ LER}\, dq \end{aligned} \tag{2.15}$$

here, $\mu^* \frac{\partial^2 q}{\partial t^2}$, $k_{LER} q$ and $k_{NC} q$ are all conservative terms, so their loop integral is 0, then the dissipation is only determined by the dissipative force inside LER. However, we do not know the $F_{Diss\ \ LER}$ directly, so we turn to estimate the energy dissipation through the definition of the quality factor Q.

$$Q \equiv 2\pi \times \frac{stored\ energy}{dissipation} \tag{2.16}$$

here, the stored energy including the potential energy stored in the spring and the kinetic energy of the oscillator within the oscillation model illustrated in Figure 2.6, therefore, $stored\ energy \approx k_{LER} Amp^2/2$. Here, Amp is the oscillation amplitude of LER. The energy dissipation $Diss_{LER}$ is determined by:

$$Diss_{LER} = 2\pi \frac{\frac{k_{LER} Amp^2}{2}}{Q} = \pi \frac{k_{LER} Amp^2}{Q} \tag{2.17}$$

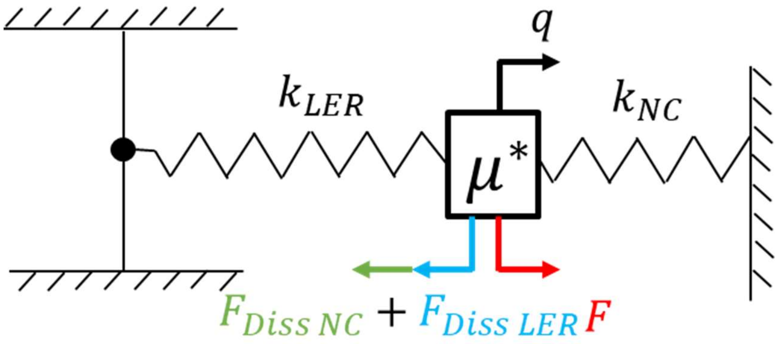

Figure 2.7 LER oscillation model, where the sample NC also exhibits energy dissipation.

Next, consider the scenario where the sample NC also exhibits energy dissipation, as illustrated inFigure 2.7. Under the condition that other parameters such as amplitude and frequency remain unchanged, the energy dissipation from NC absorbs a portion of the oscillation energy. Therefore, an additional driving voltage ΔV is required to compensate for this energy loss and maintain the oscillation of LER. Specifically, in the absence of energy dissipation from NC, the driving voltage for LER is V_0; however, when energy dissipation from NC is present, the driving voltage for LER needs to be increased by an additional voltageΔV, resulting in a total driving voltage of $V_0 + \Delta V$. This additional driving voltage ΔV is precisely used to counteract the energy loss caused by the dissipation from NC, ensuring that the oscillation state of LER remains consistent.

$$Diss_{LER} + Diss_{NC} = Diss_{LER}\frac{\Delta V + V_0}{V_0} \qquad 2.18$$

$$= \pi \frac{k_{LER}Amp^2}{Q}\left(\frac{\Delta V + V_0}{V_0}\right)$$

Assuming the driving voltage and the energy dissipation have a linear relationship, then Equation 2.17 holds. As discussed earlier, when the energy dissipation is$Diss_{LER}$, the corresponding driving voltage is V_0. Based on the linear proportionality, the total dissipation when the driving voltage increases to $\Delta V + V_0$ can be estimated as $Diss_{LER}\frac{\Delta V+V_0}{V_0}$. Therefore, the energy dissipation on the specimen NC can be estimated by the changes in the driving voltage, as shown in Equation 2.19:

$$Diss_{NC} = \pi \frac{k_{LER}Amp^2}{Q}(\frac{\Delta V}{V_0}) \quad 2.19$$

2.4 The equivalent circuit and frequency characteristics of the LER

As a sensor, the LER converts between electrical responses mechanical responses. To use the LER for measuring mechanical oscillations, we developed an electrical model of the LER and analyzed its electrical characteristics. Typically, the equivalent circuit of the LER, as shown in the Figure 2.8.

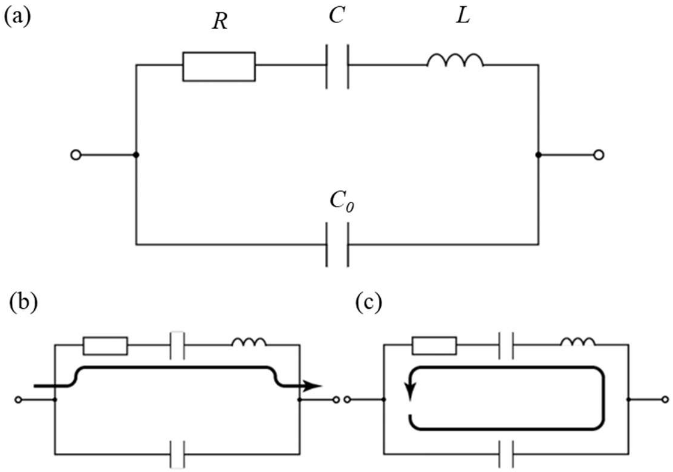

Figure 2.8 (a) Equivalent circuit of the LER. (b) Dominant current path during series resonance. (c) Dominant current path during parallel resonance.

In Figure 2.8 (a), the upper part of the equivalent circuit is a typical RCL series circuit, while the down part, C_0, is the parasitic capacitance. Parasitic capacitance is the capacitance generated in a circuit due to factors such as capbles. This capacitance is unintended in the design but can have a significant impact on circuit performance, particularly in high-frequency circuits. The impedance Z of the RCL series circuit in the upper part is given by:

$$Z_{RCL} = R + \frac{1}{j\omega C} + j\omega L = R + j(-\frac{1}{\omega C} + \omega L) \qquad 2.20$$

The LER is a parallel combination of the RCL circuit and parasitic capacitance shown in Figure 2.8 (a), so the overall impedance of the LER Z_{LER} is given by:

$$\frac{1}{Z_{LER}} = \frac{1}{Z_{RCL}} + j\omega C_0$$

$$Z_{LER} = \frac{1}{\frac{1}{Z_{RCL}} + j\omega C_0} = \frac{\left(R + \frac{1}{j\omega C_1} + j\omega L\right)\frac{1}{j\omega C_0}}{R + \frac{1}{j\omega C_1} + j\omega L + \frac{1}{j\omega C_0}} \qquad 2.21$$

The LER impedance is related to the frequency of the applied voltage ($f = \omega/2\pi$, usually expressed by angular frequency ω in circuit analysis). The frequency characteristics of the LER impedance are analyzed as follows: the real part of the impedance is determined by the equivalent resistance and is independent of frequency. After simplification, the imaginary part of the impedance is given as:

$$\mathrm{Im}[Z_{LER}] = \frac{\left\{\left(\frac{L}{C_0} - \frac{1}{\omega^2 C_0 C_1}\right)\left(\omega L - \frac{1}{\omega C_1} - \frac{1}{\omega C_0}\right) - \frac{R^2}{\omega C_0}\right\}}{R^2 + \left(\omega L - \frac{1}{\omega C_1} - \frac{1}{\omega C_0}\right)^2} \qquad 2.22$$

We noticed that under high-frequency conditions, have $\omega C_0 \gg R^2$. Under this condition, we calculate the frequencies that make the imaginary part becomes zero:

$$\left(\frac{L}{C_0}-\frac{1}{\omega^2 C_0 C_1}\right)\left(\omega L-\frac{1}{\omega C_1}-\frac{1}{\omega C_0}\right)=0 \qquad 2.23$$

therefore,

$$f_r=\frac{1}{2\pi\sqrt{L_1 C_1}} \qquad 2.24$$

$$f_a=\frac{1}{2\pi\sqrt{L_1\frac{C_0 C_1}{C_0+C_1}}} \qquad 2.25$$

These are the series resonance frequency f_r and the parallel resonance frequency f_a, respectively. When the frequency lies between f_r and f_a, the circuit exhibits inductive behavior. On the other hand, when the frequency higher than f_a, the circuit exhibits capacitive behavior. When the circuit transitions from inductive to capacitive, the phase shifts by 180°.

2.5 The mechanism of Phase-Locked Loop (PLL)

As described in the above section, achieving resonant driving (i.e., locking the LER oscillator in the resonant state is a critical step in measuring the sample's spring constant using the FM method. The amplitude and phase characteristics of voltage-modulated resonators like the LER are shown in Figure 2.9(a) illustrates the distribution of the oscillator's amplitude and phase difference as a function of the driving frequency, with the horizontal axis representing the shift from the resonance frequency; Figure 2.9(b) corresponds to the phase difference between the oscillator's input (driving signal) and output (induced signal). The key point is that the phase difference becomes zero in the resonant state. Therefore, in experiments, resonant driving can be achieved by locking the phase difference to zero.

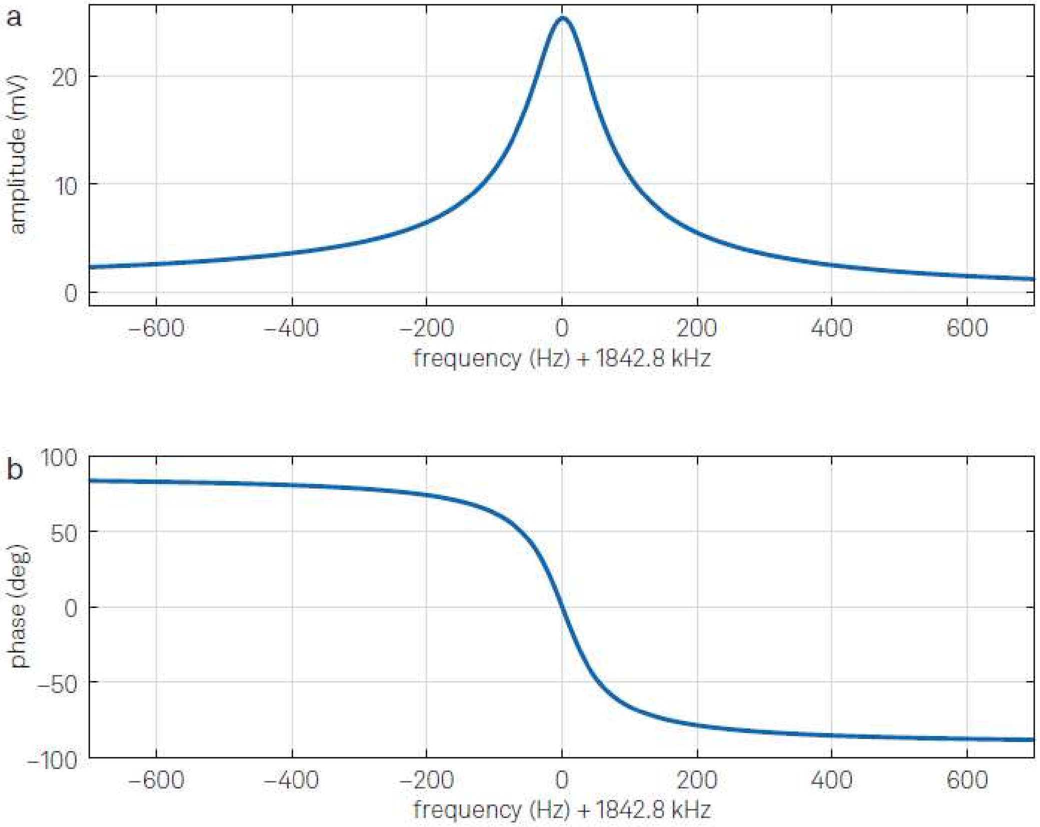

Figure 2.9 The corresponding amplitude and phase difference of the oscillator under various driving frequency. (a) The amplitude reaches its peak at resonance. Here, the horizontal axis representing the shift from the resonance frequency. (b)The phase difference between the oscillator's input (driving signal) and output (induced signal) with various driving frequency. The phase difference became 0 at resonance.

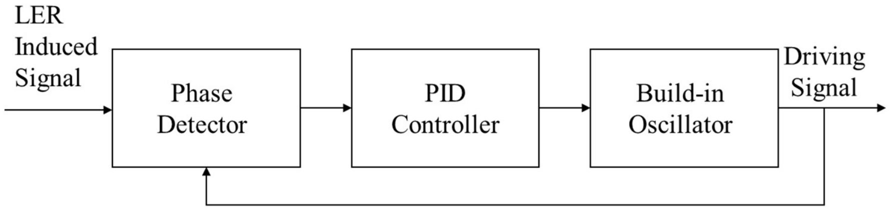

Figure 2.10 Schematic diagram of a PLL including phase detector, PID controller and build-in oscillator. The PLL generates a driving signal that has same phase and frequency of its LER induced signal.

We built a closed-loop control system with negative feedback as depicted in Figure 2.10, the PLL receives the induced signal from the LER, and using this signal to control a built-in oscillator that generates a driving signal synchronized with the LER induced signal's phase. The PLL operates by receiving an input signal, typically from a reference source, and using this signal to control an oscillator that generates an output signal synchronized with the input signal's phase. The process begins with a phase detector that measures the phase difference between the LER induced signal and the driving signal generated by the built-in oscillator. The measured phase difference is then compared to a predefined phase setpoint (usually 0 degree), resulting in an error signal. This error signal is fed into a proportional-integral-derivative (PID) controller, which processes it to produce a feedback signal. This feedback signal adjusts the frequency of the built-in oscillator to minimize the phase difference. Through this continuous adjustment, the built-in oscillator locks onto the LER induced signal's phase, ensuring the driving signal maintains the same frequency and phase evolution. This mechanism allows for precise synchronization and signal generation.

Chapter 3 Experiment setup

Introduction

This chapter introduced the experimental setups used in this study. In Chapter 3.1, we introduce the UHV TEM machine used in this study and the importance of ultra-high vacuum for this study. In Chapter 3.2, we introduce *microscopic nanomechanics measurement method* (MNMM) to realize TEM observation of nanomaterials simultaneously with measuring the mechanical properties. In Chapter 3.3, we introduce the mechanical measurement system, including the frequency and amplitude control of LER. This allows us to measure the spring constant of the specimens. Also, we estimated the oscillation amplitude of LER resonator from FFT pattern. In Chapter 3.4, we introduce the electrical measurement system. This allowed us to estimate the crows-section area of the specimens. In Chapter 3.5, we introduce the motion control system of the specimens substrate, that allows us to move the specimens inside the TEM.

3.1 Ultra-high vacuum TEM

In previous in-situ TEM observations, contaminants on the sample surface increase over time during observation. It is thought that these contaminants are composed of hydrocarbon residual gas molecules in the sample chamber. It decomposes and evaporate under electron beam irradiation, and then redeposit onto the sample surface, forming a contamination layer. These contamination layers can accumulate charge, affecting the electron beam and hindering the acquisition of structural information. More importantly, as the size of the specimen decreases, the surface properties are more sensitive to such contamination due to the increased surface-to-volume ratio, especially affecting mechanical properties. Figure 3.1(a) and (b) show typical TEM images of a clean and a contaminated sample surface, respectively. The surface atoms of a clean Au nanocrystal are orderly arranged, it can be seen that their interfaces are sharp, while the edges of a contaminated Au nanocrystal are smooth. The presence of contamination layers may affect the mechanical properties of Au nanocrystals. UHV-TEM can maintain an ultra-high vacuum (UHV) condition in the sample chamber at 10^{-7} Pa order. In such UHV conditions, the evaporated molecules consisting of carbon atoms are hardly redeposited on the surface, and the contamination layer can be reduced to keep the sample surface clean.

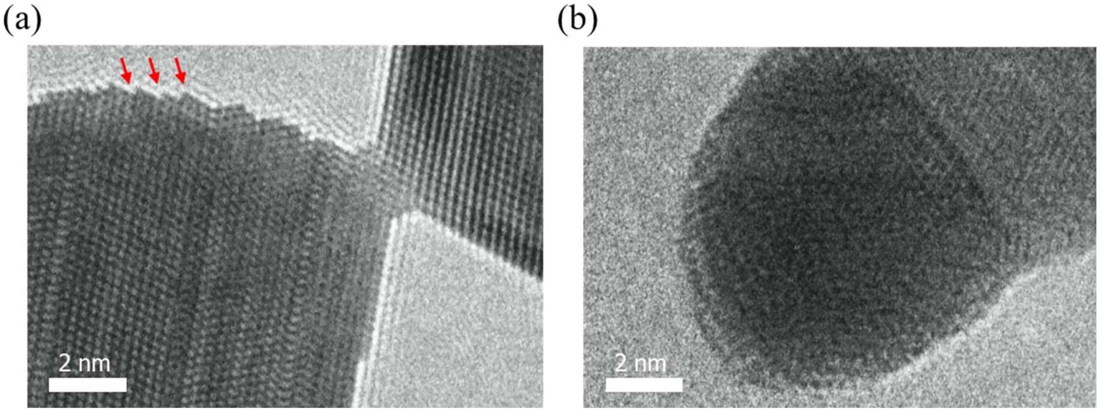

Figure 3.1 (a) The TEM image of a clean Au nanocrystal shows an orderly atomic arrangement, with sharp edges visible at the red arrow. (b) A typical TEM image of Au crystals covered by contaminants, where the edges appear smooth.

In this study, we used the UHV-TEM (JEM2000FXVB) manufactured by JEOL Ltd. as shown in Figure 3.2. The sample chamber of the TEM is evacuated by an ion pump and a titanium sublimation pump, and the maximum ultimate vacuum of the sample chamber reaches the order of 10^{-7} Pa. The spherical aberration of the objective lens is 0.705 mm, and the point resolution of the high-resolution image is 0.21 nm. The electron gun is a field emission type. The accelerating voltage during structural observation is 200 kV, the measurement environment is room temperature (300 K), and the ultra-high vacuum (7×10^{-7} Pa).

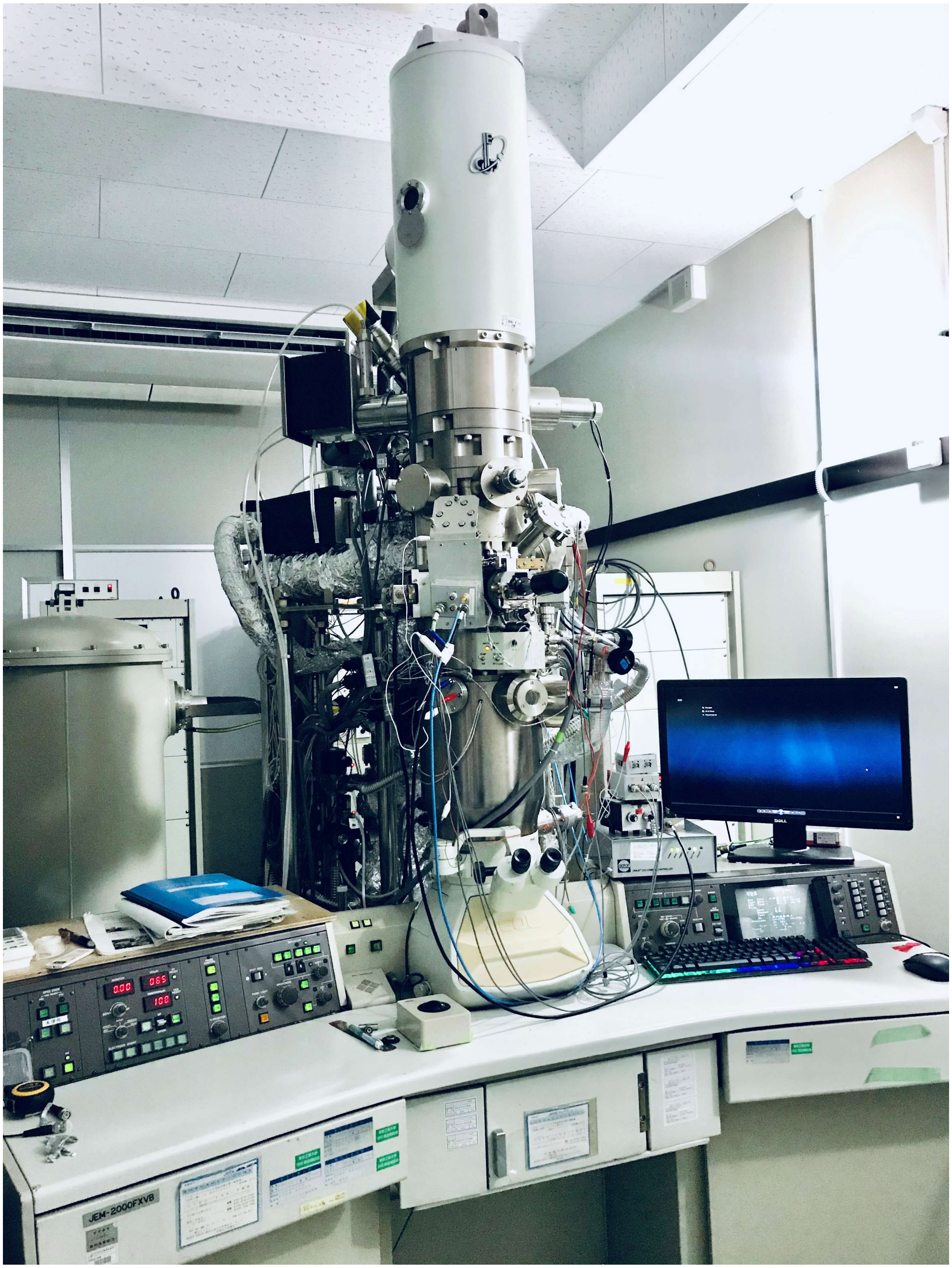

Figure 3.2 Photograph of UHV-TEM used in this study.

3.2 Microscopic nanomechanical measurement method

In this study, we used MNMM method to realize TEM observation of nanomaterials simultaneously with measuring the mechanical properties. By designing a TEM holder equipped with a force sensor of a length extension resonator (LER). the equivalent spring constant (corresponding to the force gradient) of the observed nanomaterial can be directly evaluated from the resonance frequency shift of the LER. Such a frequency modulation (FM) method is superior not only to provide a direct, elastic response, but also to provide energy dissipation from changes in the driving voltage to the LER.

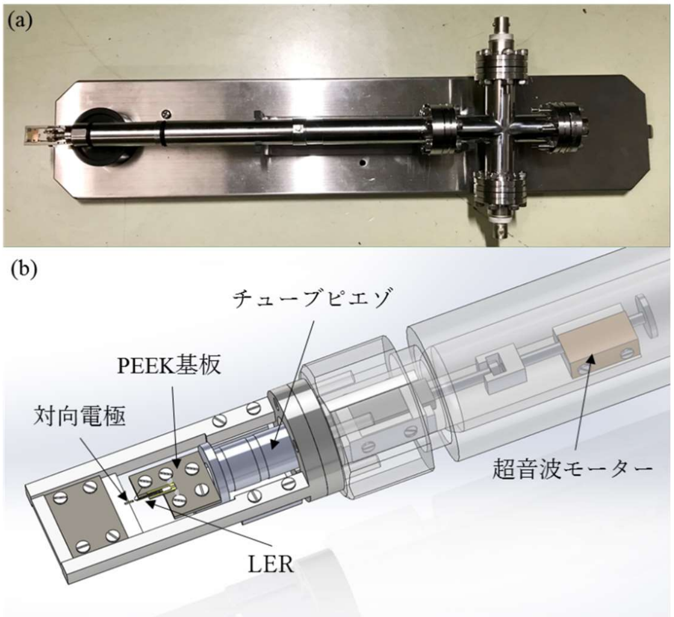

Figure 3.3 (a) Photograph of the developed TEM holder. Inset is an enlargement of the sample stage of the TEM holder. (b) An illustration of the sample stage in the TEM holder.

Figure 3.3(a) and (b) respectively show the actual photo and schematic diagram of the TEM sample holder we developed. The head part of the sample holder consists of a LER, a polyether ether ketone (PEEK) substrate that carries the LER, a counter electrode made of 100 μm diameter gold wire, a driving mechanism for the substrate, and BNC wires. The LER has advantages of high stiffness ($k_0 = 7.5 \times 10^5$ N/m) and high resonance frequency ($f_0 \approx 1$ MHz), which provide a high Q-factor and low noise level. Au wires or other nanomaterials can be suspended between the fixed electrode and the tip of the LER, allowing for visual observation through TEM. Using the FM method, the equivalent spring constant can be obtained from the shift in the LER's resonance frequency, while energy dissipation is measured by increasing the sinusoidal driving voltage applied to the LER (hereafter referred to as the driving voltage). During the experiment, the frequency and amplitude of the driving voltage are feedback-controlled by a PLL to maintain the LER's resonance and amplitude stability. The advantage of the LER lies in its ability to achieve a very small amplitude (about 30 pm), ensuring clear visibility of atomic arrangements in TEM images.

The LER is mounted on a white PEEK substrate, and its position can be finely adjusted in three directions using a tubular piezoelectric ceramic, with an adjustment range of about ±1 μm in the x, y, and z directions. Additionally, the tubular piezoelectric ceramic is mechanically connected to an ultrasonic linear motor (TULA50, Technohands) via a connecting rod, allowing coarse axial movement of the PEEK substrate and LER. Since vibrations generated by the ultrasonic motor are easily transmitted through the connecting rod, a coupling connector is designed to selectively decouple or couple the connecting rod from the ultrasonic motor, and graphite (low friction) guide rails are used to minimize vibrations transmitted through the connecting rod. The coarse adjustment range in the y direction is 5 mm. This design enables large-distance movement of the substrate while minimizing vibrations caused by the moving structure, resulting in clear TEM images.

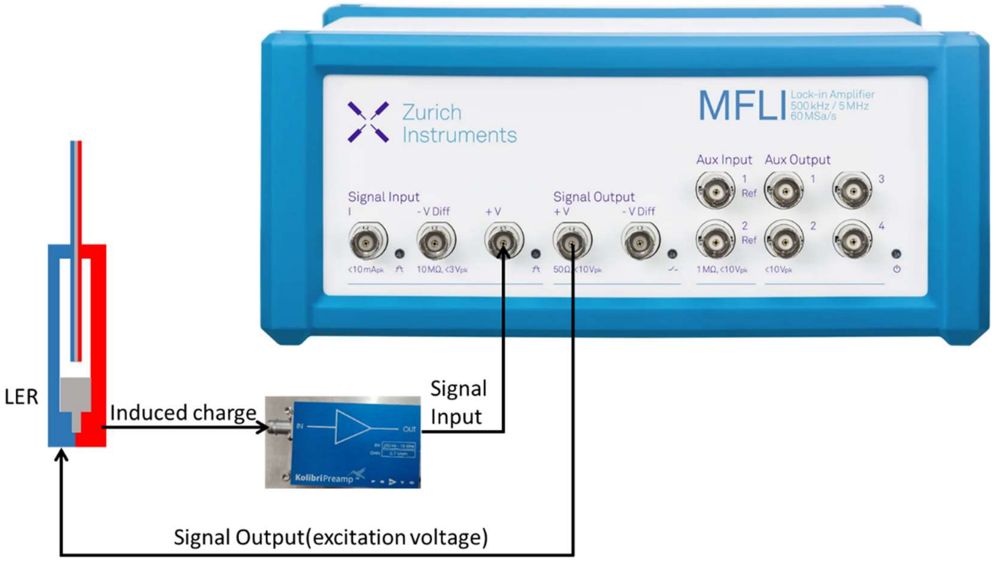

Figure 3.4 Schematic diagram of connection between LER and MFLI.

3.3 Mechanical measurement system

We use the LER as the force sensor to measure the mechanical responds of Au NC using the FM method. Using the FM method, the equivalent spring constant can be obtained from the shift in the LER's resonance frequency, while energy dissipation is measured by the extra driving voltage applied to the LER. In this study, the MFLI lock-in amplifier from Zurich Instruments was used to control the oscillation of the LER. The signal output (Signal Output V) of the MFLI is used to apply an driving voltage to the LER, which is a sinusoidal AC voltage signal. The MFLI adjusts the frequency of the driving voltage to maintain the resonance of the LER, and adjusts the amplitude of the driving voltage to control the mechanical oscillation amplitude of the LER (the mechanical oscillation amplitude of the rod). The detailed adjustment method will be described in later sections. The signal input (Signal Input) of the MFLI can read both current and voltage signals from external sources. In this study, a charge amplifier (HQA-15M-10T, FEMTO Messtechnik GmbH, with a conversion ratio of 10 V/pC) was used to convert the induced charge of the LER into a voltage signal, which was then read through the voltage input of the Signal Input.

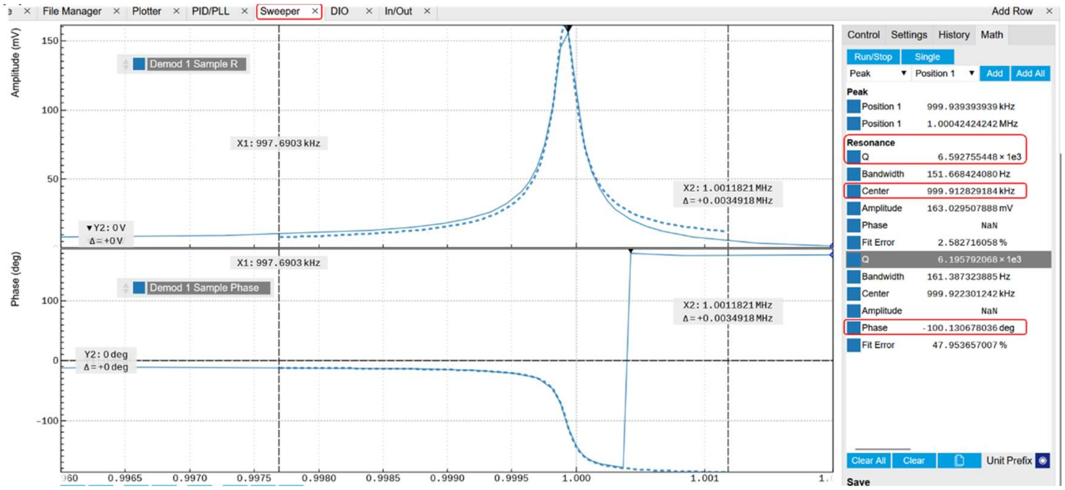

Peak	
Position 1	999.939393939 kHz
Position 1	1.00042424242 MHz
Resonance	
Q	6.592755448 × 1e3
Bandwidth	151.668424080 Hz
Center	999.912829184 kHz
Amplitude	163.029507888 mV
Phase	NaN
Fit Error	2.582716058 %
Q	6.195792068 × 1e3
Bandwidth	161.387323885 Hz
Center	999.922301242 kHz
Amplitude	NaN
Phase	-100.130678036 deg
Fit Error	47.953657007 %

Figure 3.5 The sweep result was fitted by dash lines, and the quality factor Q, resonance frequency and the phase was calculated.

Parameters including the resonance frequency, quality factor Q, and phase difference (the phase difference of input and output at resonance) are essential for setting up the PLL. The MFLI instrument has a built-in parameter sweeper function which can scan the frequency of the output signal within a specified range while continuously measuring the LER's response data (such as amplitude and phase difference). The output signal was scanned around 1 MHz, and the amplitude and phase were measured. As shown by the dashed line in Figure 3.5, the measurement results were fitted using the [Math] function, and the quality factor Q of the LER was calculated to be 6500, with a resonance frequency of 999 kHz and a phase difference of -100° at resonance. It should be noted that for voltage-controlled resonators such as the LER, resonance generally occurs at the point where the phase difference is 0. However, in the scan results shown in the figure, the phase difference is shifted by -100°. This shift is introduced by the amplifier that converts the LER's induced charge into a voltage signal.

During the process of converting the charge into a voltage signal, the amplifier causes the phase of the signal to shift backward by approximately 90°.

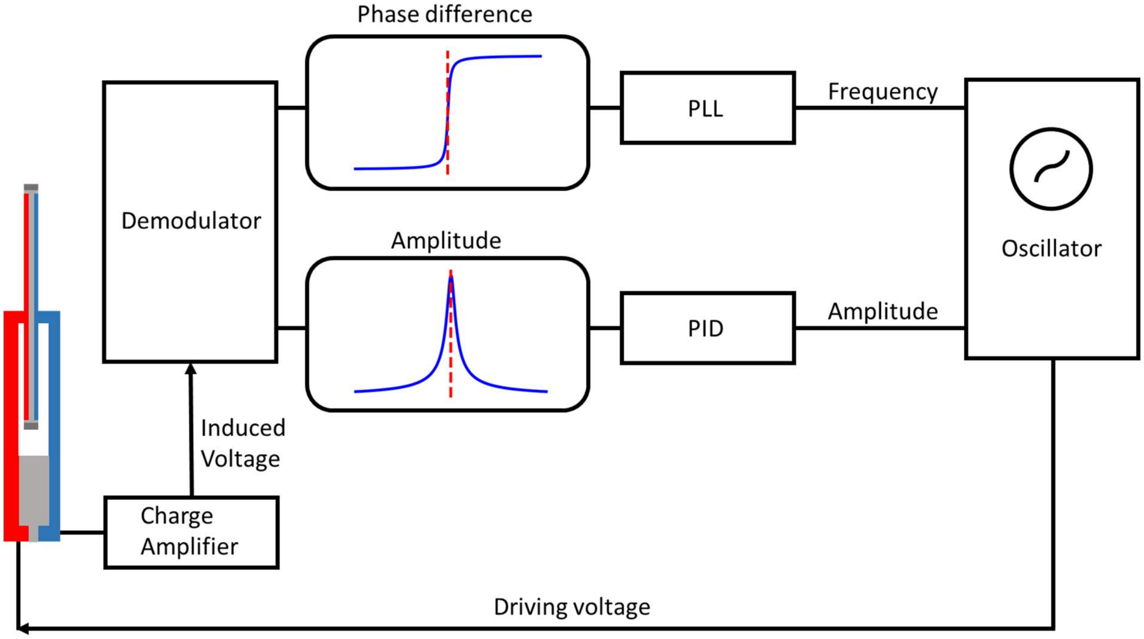

Figure 3.6 Schematic diagram of oscillation control system.

The oscillation control system is shown in Figure 3.6. The oscillator outputs an initial driving voltage to the LER, cause an electric field that make quartz crystal to deform. This leads to forced oscillation of the LER rod driven by the driving voltage. The LER oscillates at its resonant frequency when the driving voltage is applied to one electrode of the LER. The sinusoidal electric charge, induced by the deformation of the quartz crystal due to the piezoelectric effect, is monitored through the other electrode, and is proportional to the amplitude of the LER oscillation. This induced charge is converted into a voltage signal (hereafter referred to as the LER induced voltage) using a charge amplifier. The MFLI input reads the LER induced voltage, and use demodulator to separate it into the phase and amplitude signals. When the Au wires at the tip of the

LER makes contact with the fixed Au wire, the spring constant changes, leading to a shift in the LER's resonant frequency. The built-in PLL of the MFLI adjusts the driving voltage frequency, locking the phase to the resonance phase to keep the LER in a resonant state. On the other hand, the LER oscillation amplitude is controlled by PID to lock it at setpoint.

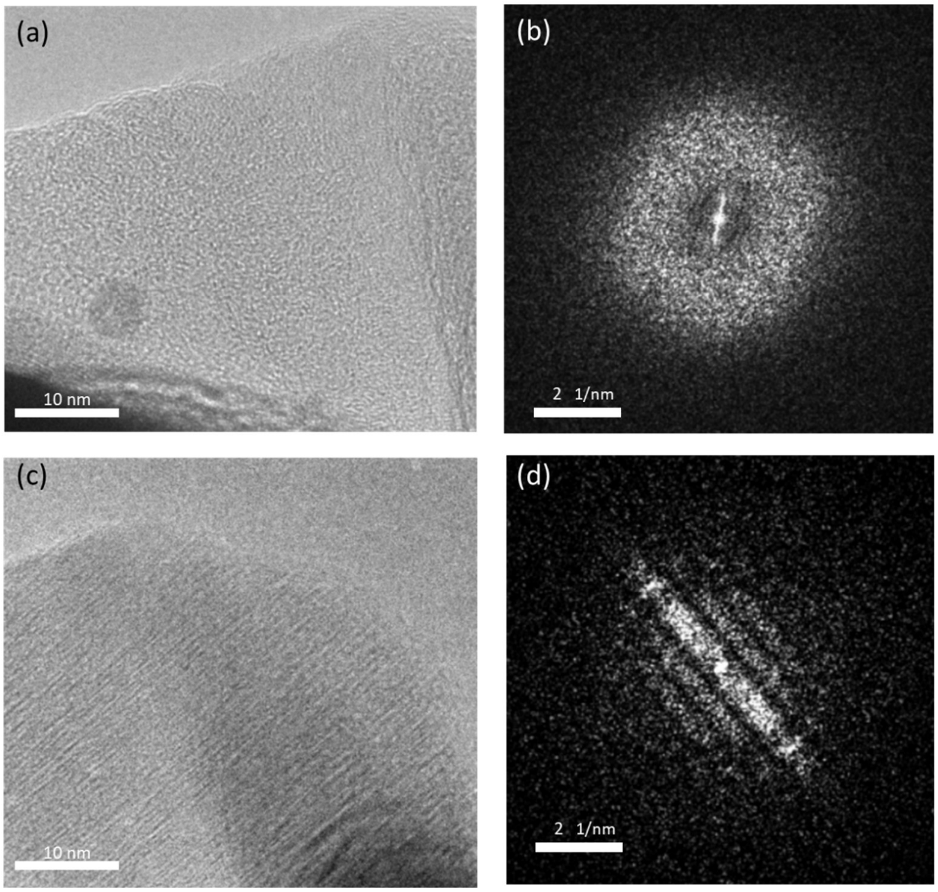

Figure 3.7 (a) TEM image of thin amorphous carbon before oscillation. (b) The FFT pattern of the captured TEM image (a). The FFT pattern of thin amorphous carbon exhibits a uniform ring before oscillation. (c) A TEM image of the same thin amorphous carbon acquired during oscillation. (d) The FFT pattern of the TEM image (c) during oscillation. White fringes appear in the FFT pattern, corresponding to the LER oscillation. The LER induced voltage from the charge amplifier was 400 mV.

We calibrated the relationship between the LER induced voltage and the LER amplitude. The LER induced voltage was locked at 200 mV, 300 mV, 350 mV, and 400 mV, then we measured the corresponding LER amplitude. Conventionally, accurately measuring the LER amplitude has been challenging since it is extremely small (pm order). In this study, we aimed to precisely measure the LER sensitivity by estimating the LER amplitude from TEM images. In detail, as shown in Figure 3.7(a) we observed a thin layer of amorphous near the tip of the LER, its FFT pattern of thin amorphous carbon exhibits as a uniform ring (Figure 3.7(b)). When the LER oscillate with large amplitude, the TEM image of the amorphous became blurred (Figure 3.7(c)), and white periodic stripes appeared in the Fourier transform (FFT) pattern, as shown in Figure 3.7(d). A contrast of a FFT pattern can be expressed as follow:

$$f(x) = \sum_{i} \alpha_i \sin(k_i x + \delta_i) + C \qquad 3.1$$

where α_i is the intensity of the wave component i, k_i is the wave number, δ_i is the arbitrary phase and C is the background intensity. Here we assume that α_i does not strongly depend on i, because the contrast of TEM image of amorphous carbon is almost uniform.

Consider that the sample position is shifted by $x' = A\sin(\omega t)$ due to the LER oscillation where A is the oscillation amplitude and ω is the angular oscillation frequency of the LER. Thus, the time-averaged contrast of FFT pattern over the one cycle, $g(x)$ can be described as follow:

$$g(x) = \frac{\omega}{2\pi} \int_{-\frac{\pi}{\omega}}^{\frac{\pi}{\omega}} f(x - x') d\mathrm{t} \qquad 3.2$$

Since $dx' = A\omega \cos \omega t d\mathrm{t}$, equation 3.2 can be expressed as below:

$$g(x) = \frac{\omega}{\pi}\int_{-\mathrm{A}}^{\mathrm{A}} f(x-x')\frac{1}{\sqrt{A^2 - x'^2}}dx' \tag{3.3}$$

The FFT pattern during the oscillation can be obtained:

$$g(x) = \sum_i J_0(k_i A)\alpha_i \sin(k_i x + \delta_i) + C \tag{3.4}$$

here $J_0(k_i A)$ represents the zero-order Bessel function of the first kind. It indicates that the FFT pattern intensity $g(x)$ is expressed by multiplying the $f(x)$ with $|J_0(k_i A)|$. It can be seen from equation 3.4, when $|J_0(k_i A)|$ takes its zero point (in other worlds, when $|J_0(k_i A)| = 0$), FFT pattern intensity $g(x)$ takes its local minima. The local minima of FFT pattern intensity $g(x)$ is the dark fringes in FFT pattern. Therefore, the oscillation amplitude A can be estimated by the distance of the dark fringes in FFT pattern.

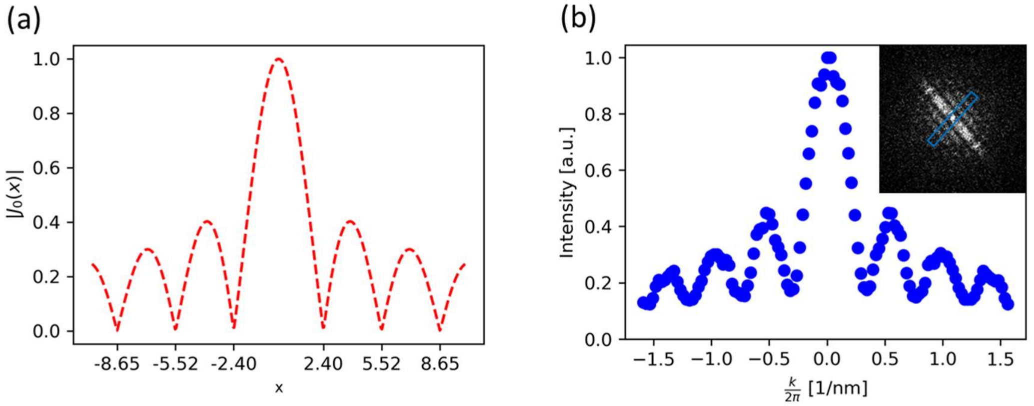

Figure 3.8 (a)Function $|J_0(x)|$ and its zero points. (b) The intensity profile of the white fringes. This profile was extracted from the blue-boxed region of the FFT pattern in the inset.

The absolute value of the zeroth-order first kind Bessel function ($|J_0(x)|$) is shown in Figure 3.8(a). $|J_0(x)|$function has fixed zero points, for example $|J_0(2.4048)| =$

$|J_0(5.5201)| = |J_0(8.6537)| = 0$. As shown in the Figure 3.8(b), from the FFT pattern extracted a region with a length of 150 pixels that perpendicular direction to the white fringes, and the plotted intensity profile of this region. According to equation 3.4, by fitting the amplitude A, making the local minima of the intensity profile be aligned with the zeros points of the function $|J_0(kA)|$, the LER oscillation amplitude can be estimated.

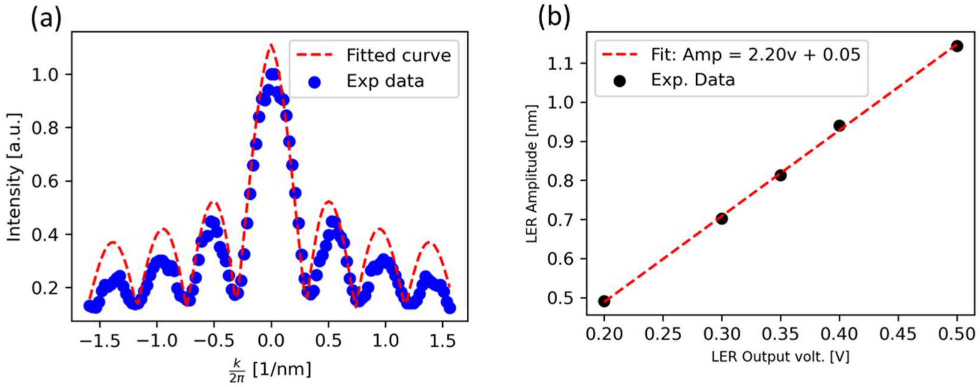

Figure 3.9 (a) The fitted $|J_0(k_i A)|$ and the FFT pattern profile from experiments. (b) The relationship between the LER induced voltage and the mechanical oscillation amplitude. The induced charge generated by the mechanical oscillation of the LER is converted into voltage of the LER through an amplifier.

More specifically, as shown in Figure 3.8(b), there is a first minimum point to the right of the center at $k/2\pi = 0.335$ *1/nm* in the profile curve. This point should correspond to the point where $AK = 2.4048$ (because $|J_0(2.4048)| = 0$) in Figure 3.8(a), allowing us to calculate $A = \frac{2.4048}{2\pi \ 0.335 \ 1/\mathrm{nm}} = 1.1466$ nm. When calculating the amplitude, A, it is important not only to fit one minimum point but also to align the positions of all minimum points with the experimental data as closely as possible. I wrote a Python program that uses $\left|J_0\left(\frac{\mathrm{k}}{2\pi}2\pi A\right)\right| + 0.1$ as the objective function to fit the experimental profile. I used the least squares fitting method. The fit result was shown in Figure 3.9(a). The estimated LER amplitude was 1.1466 nm. This analysis is reasonable, since the intensity modulation in the FFT pattern is well reproduced by the Bessel function (Figure 3.9(a)). Then, since the LER induced voltage was 500 mV, the sensitivity was estimated to be 2.2 nm/V. For more fitting points, the LER induced voltage was locked at 200 mV, 300 mV, 350 mV and 400 mV, and the corresponding LER amplitudes were obtained through the above method. These results showed a linear relationship between the LER oscillation amplitude and LER induced voltage as shown in Figure 3.9(b), indicating that the sensitivity was 2.2 nm/V. Now, we can estimate the LER oscillation amplitude (in length) by LER induced voltage.

3.4 Electrical measurement system

The mean free path refers to the average distance an electron can travel freely before undergoing a scattering event. During this process, the electron is not disturbed by impurities, lattice vibrations, or other defects. When the size of a metallic material is much smaller than the electron's mean free path, the probability of electrons scattering (such as interacting with lattice vibrations, impurities, or defects) as they pass through the material is significantly reduced. Electrons experience almost no scattering during transmission, as known as ballistic conduction. The conductance can be described by the Landauer formula:

$$G = \frac{2e^2}{h} \sum T_n \qquad 3.5$$

Here, T_n represents the transmission probability of the n-th conduction mode. Under ideal conditions (i.e., $T_n \approx 1$), the total conductance can be approximately expressed as:

$$G = \frac{2e^2}{h} N \qquad 3.6$$

N is the number of conduction modes, which is proportional to the cross-sectional area. Therefore, the cross-sectional area of the NC is proportional to its conductivity value. As shown in the Figure 3.10, a gold foil is attached to the 10 μm diameter gold wire. Appliy bias voltage through this gold foil, and the current flows through the NC. The counter part Au wire was connected to the conductivity measurement equipment. This current flowing through the NC was converted by a current amplifier (FEMTO DLPCA-200), and then measured by MFLI Aux port. The current amplifier, as shown in Figure 3.11, has a gain and measurable range from 10^3 to 10^{11} V/A and ±10 V, respectively. We made a LABView program to read this signal from MFLI Aux port, calculate the conductance value by the bias voltage and the current amplifier parameter the conductance value is displayed in real-time on the LABView panel, as shown in Figure 3.12.

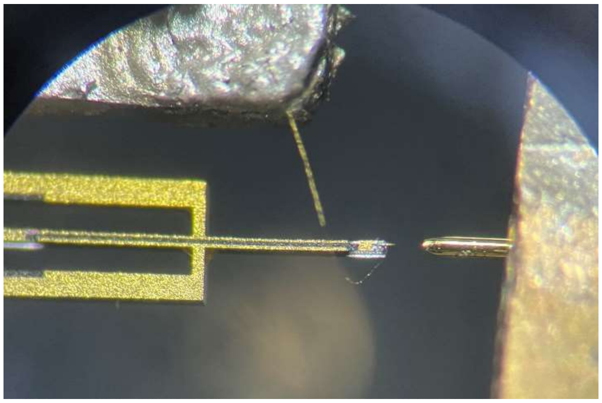

Figure 3.10 A photo of the PEEK board that carries LER and one gold foil. The gold foil lead connected to an Au wire (diameter: 10 μm), used for measuring conductivity.

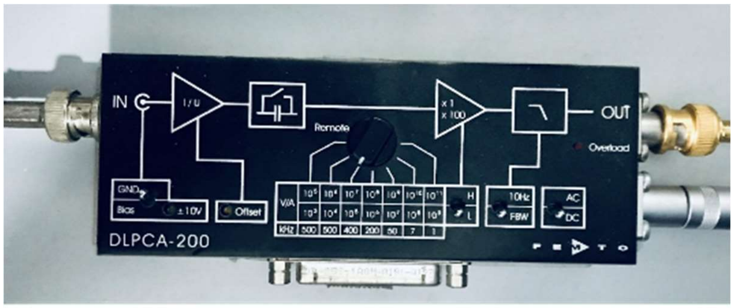

Figure 3.11 The current amplifier used in this study.

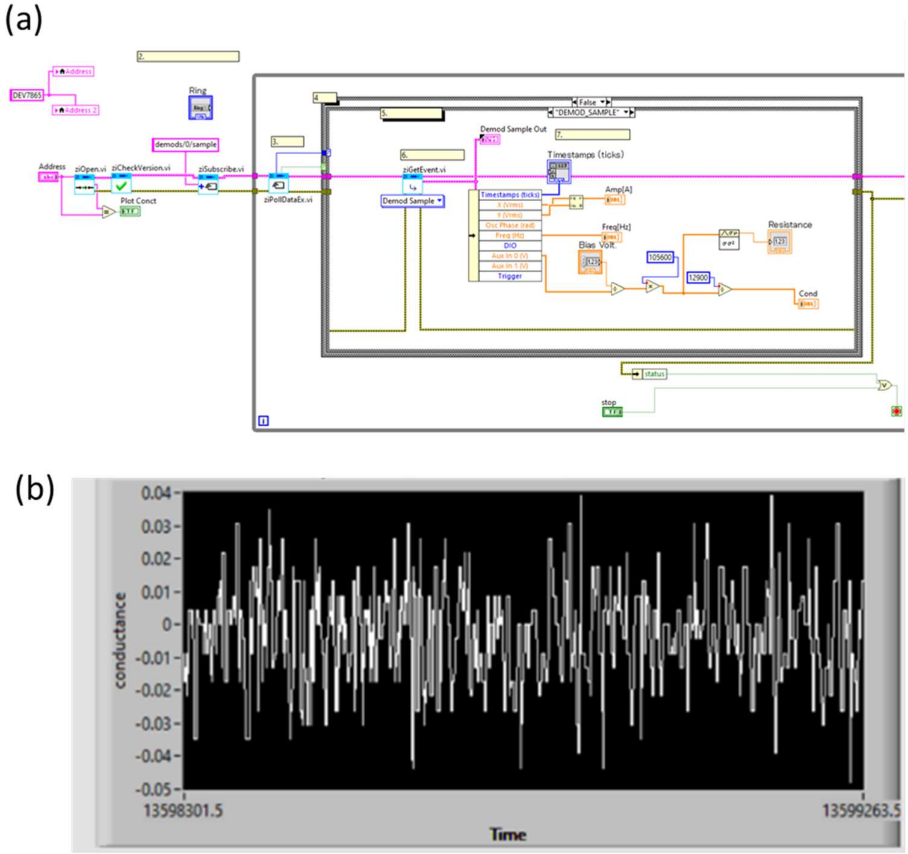

Figure 3.12 (a) The LABView program for calculating the conductance and display in real-time on the panel. Pulled data from MFLI through data streaming node [Demod Sample 0], read the Aux input by [Aux In 0]. (b) The conductance value is displayed in real-time on the LABView panel.

3.5 Motion control part of sample platform

Both the Au sample and the LER sensor are install on a PEEK substrate, we need to move this substrate to make the two Au wires touch to fabricate Au nanocontact. The position of the PEEK substrate can be driven by both coarse and fine motions. The motion control unit in our TEM holder is shown in Figure 3.13, for coarse motion, a ultrasonic motor (TULA50, Technohands) was used to push or pull the sample substrate. The ultrasonic motor operates by utilizing the piezoelectric effect of piezoelectric ceramics to convert ultrasonic vibrations into linear or rotary motion. The movement principle is piezoelectric ceramic vibrates and reaches the drive shaft, pulls the friction body by changing the duty ratio of going and return, using this action to moving the unite distance. With small movement controlled by high vibration frequency, actuator can move smoothly. The moving range of coarse motion can be hundreds of μm, and the minimum step length can be as low as 50 nm.

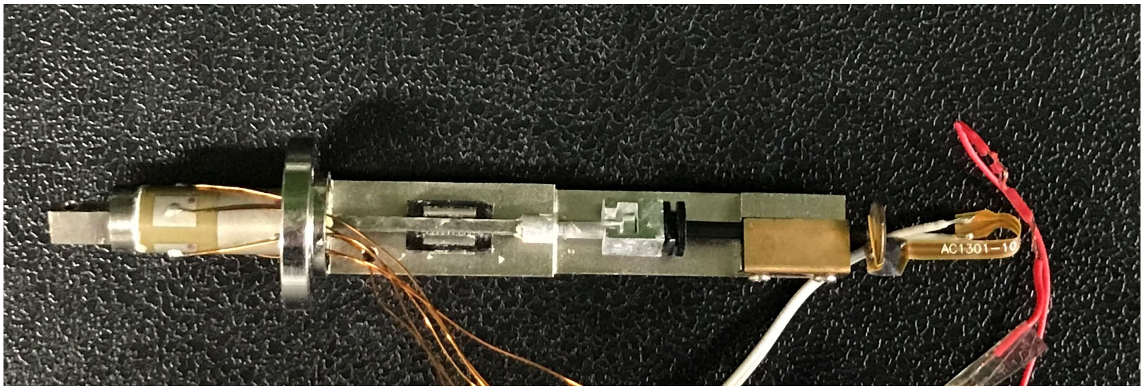

Figure 3.13 The motion control unit in our TEM holder.

For fine motions, as shown in Figure 3.13, a tube piezo, which fixed with the sample substrate, enables movement and positioning. This tube piezo can deform in x,y,z directions when voltage applied. Here, we use three Aux output ports to control the voltages dring this tube piezo. The voltage output range of MFLI Aux output is ±10V, however, it needs a much higher voltage (over 100 V) to have enough deform on tube piezo. We use a piezo driver (MESS-TEK M-2680) to amplify the control voltage from MFLI Aux output by 30 times and apply it to the tube piezo. The deformation coefficient of the tube piezo is 2.67 nm/V.

Chapter 4 Elastic properties of Au nanocontacts

Introduction

This chapter introduces the study of the elastic properties and local Young’s modulus of nanocrystals. Section 4.1 provides an overview of research on Young’s modulus at the nanoscale and explains the necessity of measuring the local Young’s modulus of nanomaterials. Section 4.2 explains the principles for measuring the local Young’s modulus. Section 4.3 briefly describes the experimental setup and raw data, including the process of cross-sectional area reduction during the stretching process. Section 4.4 provides a detailed description of the method for accurately measuring lattice spacing using TEM images and shows the evolution of lattice spacing under tensile stress. Section 4.5 presents the measurement results of the local Young’s modulus, compares them with previous studies, and discuss. Section 4.6 summarizes this chapter.

4.1 Previous studies on the Young's modulus of nanomaterials

Young's modulus can describe a material's elastic property. As shown in Figure 4.1, when a force is applied to an object, it elongates from its original length L to $L + \Delta L$. To evaluate the elastic response without being affected by the size and shape, we focus on the force applied per unit area (stress) and the elongation for per unit length (strain). Young's modulus is defined as the ratio of stress to strain, it can represent the material's inherent elastic property. Young's modulus is an important parameter for understanding such an elastic response. Conventionally, the modulus is measured by applying the loading force and measuring displacement, which is called the stretching test. This test can be performed without taking care of the stretching direction for bulk materials, because the orientation dependence of Young’s modulus can be ignored owing to the polycrystallinity of bulk materials. On the other hand, Young's modulus of nanomaterials has been suggested to depend not only on the size but also on the orientation, since the nanomaterials tend to be monocrystalline[33,34]. In calculation, Young's moduli of a single gold (Au) crystal show a pronounced elastic anisotropy. Liu et al. reported that Young's modulus of a single Au crystal was calculated to be 72.2, 104.1, and 157.1 GPa for the [100], [110], and [111] directions, respectively, based on their molecular static calculations[35]. Meanwhile, Young’s modulus of Au nanowires with the axis of the [100], [110], and [111] directions with a diameter of about 2.29 nm have been calculated to be 53.38, 111.63, and 135.59 GPa, respectively[36]. The size dependence of elastic properties has been discussed based on theoretical calculations[37]. As the diameter of a nanowire decreases, the surface-to-volume ratio significantly increases, enlarging the influence on the surface properties. Two possible surface mechanical responses have been pointed out: softening and hardening. Softening is caused by a reduction in the coordination number of surface atoms, and hardening is by the redistribution of electrons of the surface atoms[16,38–40]. However, due to a lack of experimental results, no clear conclusion has been reached on Young's modulus size dependence of metallic nanocontacts (NCs) with diameters of 10 nm or less, where surface effects are expected to appear[41].

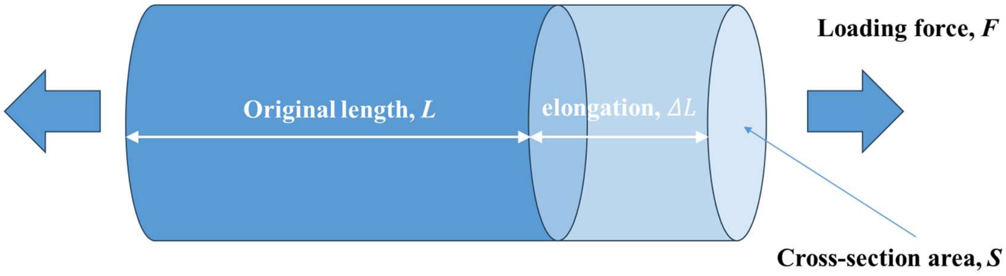

Figure 4.1 Schematic diagram of the deformation of an object with a uniform cross-sectional area under applied force.

In experiments, the estimation of Young's modulus of nanomaterials is typically conducted using the bending test method. Wu et al. utilized nanowire bending under lateral load exerted by an atomic force microscope (AFM) tip to estimate the Young's modulus of Au nanowires [23]. They found that the Young’s modulus remained consistent irrespective of diameters ranging from 250 nm to 40 nm, suggesting that the surface effects might not be crucial enough to lead to the size dependence of the Young's modulus within such a size range. Apparent Young's moduli of Ag and Pd nanowires, measured using atomic force microscopy, have been reported to be close to bulk values (76 GPa for Ag and 16 GPa for Pb) for diameters larger than 70 nm and 100 nm, respectively. On the other hand, their Young's moduli tended to increase with decreasing diameter, which was explained by the effect of surface tension [42]. The Young’s modulus of Ag nanowires with diameters between 34 and 130 nm was also reported to increase as the diameter decreased by achieving the in-situ tensile testing in a scanning electron microscope (SEM) [43]. However, the size dependence of Young's modulus is controversial. Some reported that Young's modulus increased with decreasing size [20,43–45], while others reported that it decreased [46,47].

In many cases, the size dependence of Young's modulus has been investigated for nanowires larger than 10 nm in diameter. Simply, the ratio of surface atoms to total atoms is inversely proportional to diameter: assuming an atom diameter of about 0.2 nm, the ratio drops to about 0.1 for nanowires with a diameter of 10 nm. To clarify the surface effect more clearly, it is necessary to examine the size dependence of Young's modulus for nanowires with a diameter of 10 nm or less, where the ratio of surface atoms to total atoms is large enough. However, few such experimental results have been obtained. One of the reasons is that it is required to measure the dimensions of the nanowire at an atom level.

4.2 Principles of estimating the local Young's modulus

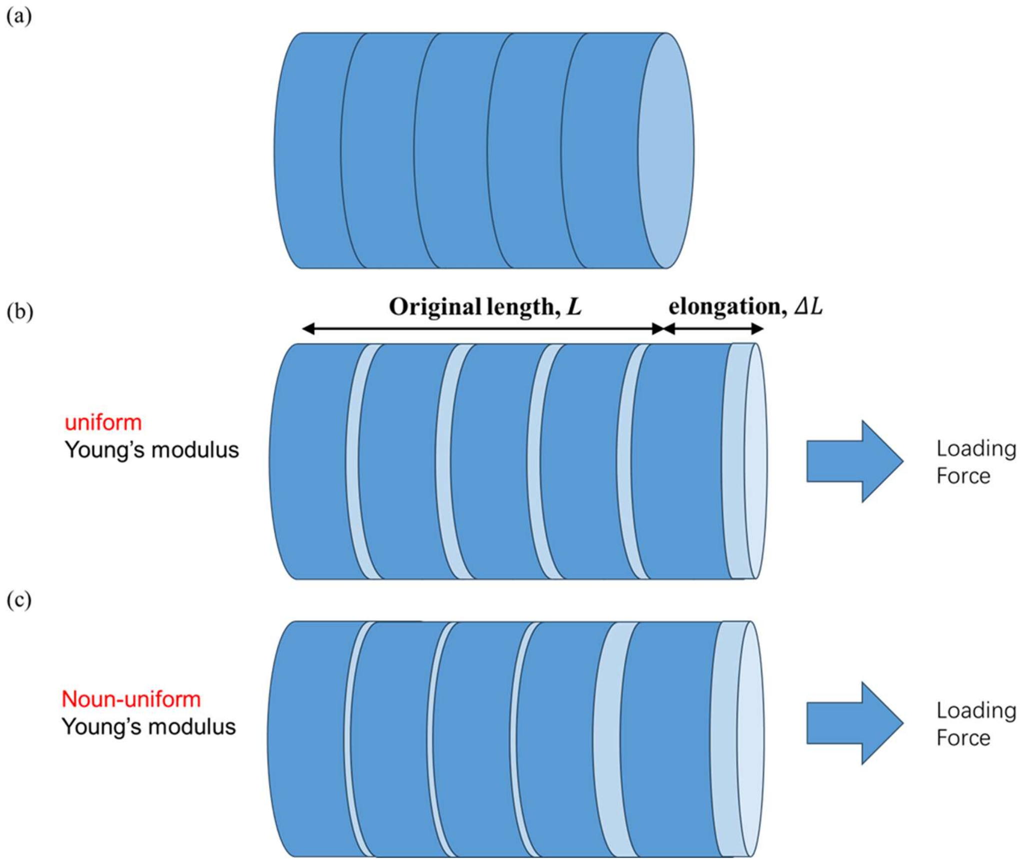

Figure 4.2 Schematic diagram of out idea to of estimating the local Young's modulus from the local strain. (a) One nanomaterial object was divide into several local regions. (b) Elastic response under applied force with uniform Young's modulus and consistent local elongation. (c) In the case of non-uniform local Young's modulus, the local strain distribution will be uneven. The local Young's modulus can be estimated by the ratio of local strain to total strain.

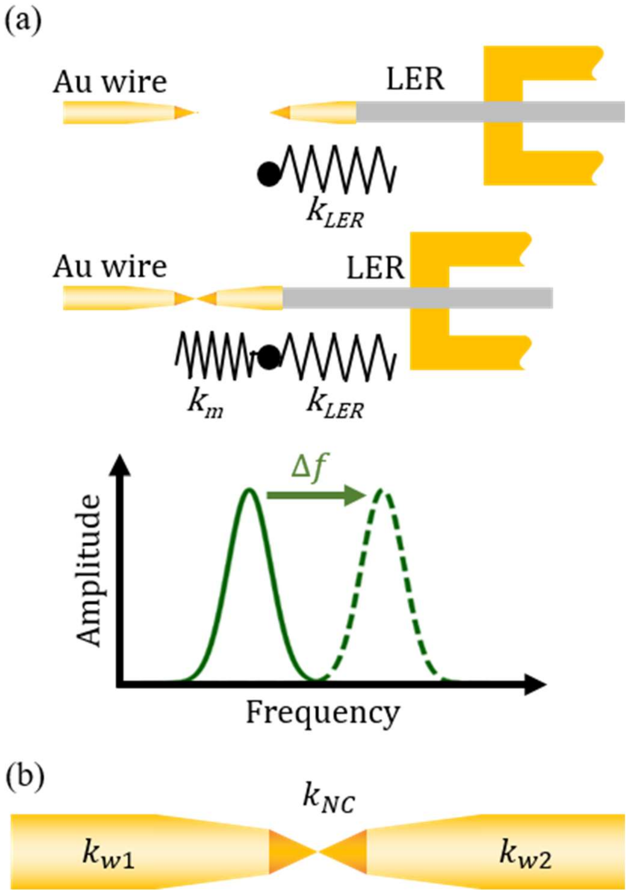

Figure 4.3 (a) Schematic illustrations of FM method for measuring the spring constant of the NC using the shift in resonance frequency. kLER is the spring constant of the LER, and km is the equivalent spring constant of the Au NC and two metal (Au) wires. The resonance curve shifts by Δf owing to the NC formation, as shown in the graph of the oscillation amplitude as a function of the oscillation frequency (b) Schematic of two Au wires supporting an NC: The NC section is marked in orange with a spring constant k_{NC}. The Au wires supporting the NC are marked in yellow with spring constants k_{w1} and k_{w2}.

As described in the methods of Chapter 2, the spring constant of the NCs can be measured by the FM method, as shown in Figure 4.2(a). An Au wire of 10 μm in diameter was attached to the LER, which oscillated at the resonance frequency (f_0). The Au NC was formed by contacting the Au wire attached to the counter electrode. When contacting, the resonance frequency was shifted by Δf due to a serial couple of LER and the Au contact including two Au wires supporting it, which can be regarded as two metal probes, as shown in Figure 4.3(b). Therefore, the equivalent spring constant of the Au contact and two metal probes, k_m, can be estimated by $k_m = 2k_{LER}\Delta f/f_0$ (see the more detail in Experiment).

In mechanical property measurements such as tensile and compression tests, the applied force extends over the entire object being measured, including the probes. For example, if a nanomaterial is a measurement target, the elastic property is measured including two metal probes supporting it. The estimated equivalent spring constant (k_m) can be expressed by a series coupling of the spring constant of the nanomaterial (k_NC) and the spring constant of two Au wires supporting it (k_w1 and k_w2) as follows (Figure 4.3 (b)):

$$\frac{1}{k_m} = \frac{1}{k_{NC}} + \frac{1}{k_{w1}} + \frac{1}{k_{w2}} \qquad 4.1$$

This equation indicates that the contribution of two Au wires must be eliminated from the measured spring constant to determine the elastic properties of the nanomaterial. Such consideration applies to all mechanical property measurement methods, such as silicon cantilever-based methods. However, it is not easy to evaluate the spring constant of the tips of two Au wires. In the case of the MNMM, the two Au wires that support the NC are very sharp; their equivalent spring constants have the same order as the NC (~ tens N/m). As can be seen from equation 4.1, the influence of the equivalent spring constant of the two Au wires cannot be ignored for this reason.

As mentioned above, Zhang et al. overcome this problem by comparing the spring constant before and after a {111} layer was introduced in stretching. However, their method does not apply to other materials and stretching directions.

In this study, a new method for estimating Young's modulus of nanomaterials is proposed. Young’s modulus (Y) is defined to be a proportional coefficient by assuming a linear relationship between strain (ϵ) and stress (σ) as follows:

$$\sigma \equiv Y\epsilon \tag{4.2}$$

Accordingly, Young’s modulus can be obtained when the values of strain and stress are obtained. Equation 4.2 is valid for any region designated between two planes perpendicular to the stretching direction in the process of elastic deformation. Therefore, the local Young's modulus in a region (Y_{local}) can be determined from the force (F) applied to this region as follows:

$$\frac{F}{S_{local}} = Y_{local}\frac{\Delta l_{local}}{l_{local}} \tag{4.3}$$

Here, S_{local} is the cross-sectional area of the region, l_{local} is the length of the region at the force equilibrium point, and Δl_{local} is the change in l_{local}. The force (F) applied to this region can be evaluated from the product of the measured equivalent spring constant (k_m) and the piezo elongation (ΔL_{piezo}) from the force equilibrium point in the MNMM, which corresponds to the total change of l_{local} over the stretched regions:

$$F = k_m\Delta L_{piezo} \tag{4.4}$$

In the experiment, since the piezo produces displacement at a constant rate, its elongation can be obtained by a product of the ratio and the elongation time within one elastic elongation process. Therefore, the local Young's modulus can be obtained as follows:

$$Y_{local} = k_m \frac{l_{local}}{S_{local}} \frac{\Delta L_{piezo}}{\Delta l_{local}} \qquad 4.5$$

During stretching, the metal NC is elastically stretched and then relaxed by plastic deformation. Such elastic and plastic deformation occurs repeatedly. Equation (5) indicates that the local Young's modulus can be estimated when measuring the ratio of the piezo elongation to the displacement of the local region $\Delta L_{piezo}/\Delta l_{local}$ at any time interval of the elastic deformation process.

4.3 Experimental Setup

The design of the *in-situ* TEM holder equipped with LER and the sample preparation is briefly explained in Chapter 2 (Figure 3.3). In this holder, the LER is mounted on a polyetherketoneketone (PEEK) board substrate. The Au $\langle 111 \rangle$ NC was fabricated in the following procedure: An Au wire with a diameter of 100 µm was set with the fixed electrode, and an Au wire with 10 µm in diameter and approximately 150 µm in length was attached to the LER tip. The height difference between the two Au wires was adjusted so that they could be in contact with each other. This contact could form the Au NC. To make the Au wires clean, they were baked in advance at ~100 °C for at least 24 h in a vacuum chamber. Afterward, they were irradiated with an intense electron beam (~100 A/cm^2) in an ultrahigh vacuum (UHV)-TEM to remove residual contaminations adsorbed on them.

In the experiment, the Au NCs are stretched and thinned by using a tube piezo. Figure 4.4(a) shows a typical TEM image of the Au ⟨111⟩ NC. It exhibits an "hourglass" shape, which is constructed by two truncated triangular pyramids composed of three different {111} surfaces joined to face each other [4,48]. When the Au NC was stretched at a constant rate by the piezo in the stretching process, it became thinner by repeating the elastic and plastic deformations. In the case of Au ⟨111⟩ NCs, a new layer of the {111} lattice plane is introduced at the narrowest constriction during plastic deformation to maintain the "hourglass" shape. In the previous study [4], it has been pointed out that the new layer of the {111} lattice plane was introduced by the migration of surface atoms, which moved from the bulk part supporting the Au NC. Compared with the TEM image of Figure 4.4(a), three layers of the {111} lattice planes were introduced at the narrowest constriction in the TEM image of Figure 4.4(b).

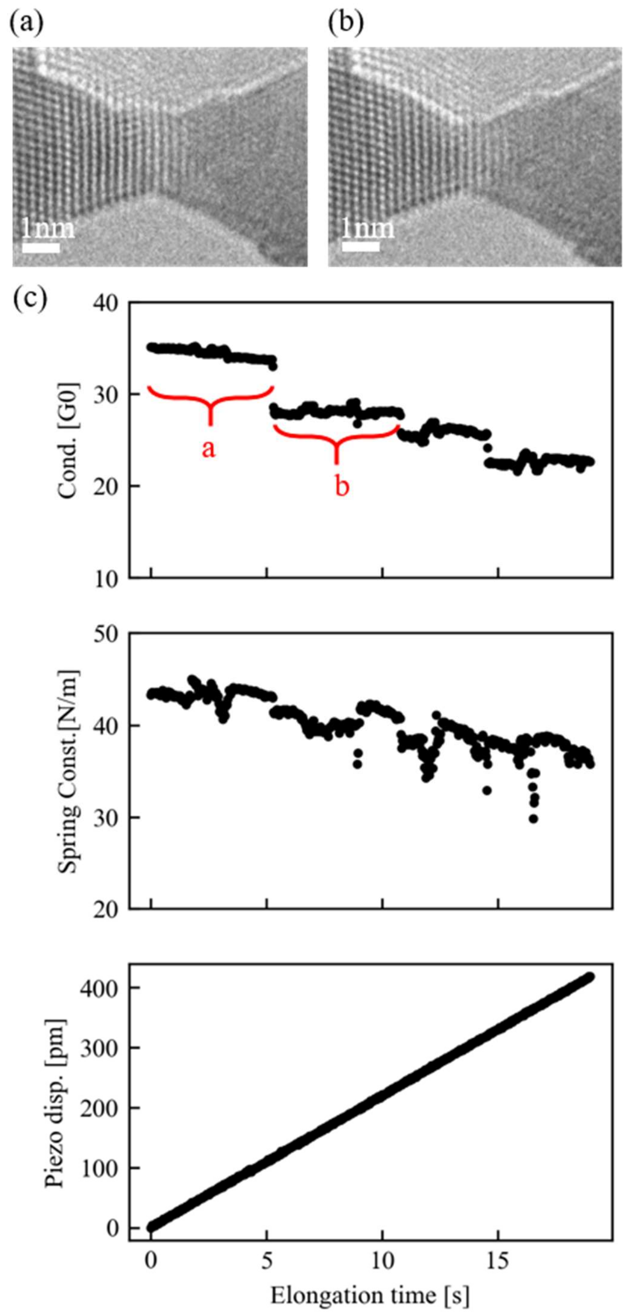

Figure 4.4 (a)(b) TEM images of the Au ⟨111⟩ NC taken before and after plastic deformation, respectively, during the stretching process. The white scale bar indicates 1 nm. (c) Time evolution of electrical conductance, spring constant, and the piezo displacement during the stretching process. The piezo displacement increased at a constant rate of 22 pm/s. The two elastic stages labelled "a" and "b" correspond to the

TEM images in (a) and (b), respectively.

The cross-sectional area of the narrowest constriction in the Au NC can be estimated by electrical conductance as reported previously [49]. When the diameter at the narrowest constriction is small enough (a few nm), the conductance has been pointed out to be proportional to the cross-sectional area and satisfy the Sharvin formula $S = {\lambda_f}^2 G_c/\pi$ (where λ_f is the Fermi wavelength of Au (0.52 nm), and G_c is the conductance value in units of G_0 ($G_c = 2e^2/\hbar$)) [50]. Figure 4.4(c) shows the time evolution of electrical conductance when the Au $\langle 111 \rangle$ NC was stretched at a constant rate. In Figure 4.4(c), the conductance plateau corresponds to the elastic deformation in the stretching process, while the conductance jumps to the plastic deformation. To estimate Young's modulus of the Au NC, we performed our analysis in the region of the elastic response.

Figure 4.4(c) also shows the time evolution of the measured spring constant and total stretching distance (corresponding to the piezo displacement). The measured spring constant was almost kept constant in the elastic stage indicated by “a”, decreased abruptly at the moment of plastic deformation and then maintained a constant value in the next elastic stage indicated by “b”. The TEM images in elastic stages “a” and “b” are shown in Fig. 3(a) and (b), respectively. The piezo displacement increased at a constant rate of 22 pm/s. Considering Eq. (5), Young's modulus of a certain region, designated between two planes perpendicular to the stretching direction in the Au $\langle 111 \rangle$ NC, can be obtained by the ratio of the piezo elongation (ΔL_{piezo}) to the displacement of this local region (Δl_{local}) in the elastic deformation process, which can be obtained from the TEM image.

4.4 Measurement of local spacings in TEM images

Since the displacement of a local region in the Au $\langle 111 \rangle$ NC is at a sub-angstrom level, it needs to measure the elastic displacement with high accuracy. First, the intensity profile along the {111} lattice planes, corresponding to darker fringes in the TEM image, was obtained by averaging the intensity of pixels along the fringe parallel to the {111} lattice fringe (Figure 4.5(a) and (b)). Second, the lattice plane positions were determined at a sub-pixel level by fitting a Gaussian function to the intensity profile so that each lattice plane position corresponded to the bottom of each valley in the intensity profile (Figure 4.5(c)). Although the pixel size was 25 pm in the TEM image of Figure 4.5, the lattice plane position was identified with at least a few pm levels of accuracy by developing a Python program to fit the Gaussian function to the intensity profile.

In the case of the Au $\langle 111 \rangle$ NC of an hourglass-like shape, the displacement of each {111} lattice spacing depends not only on its cross-sectional area but also on the local Young's modulus, if the Young’s modulus changes depending on the size as previously reported [4]. We tried to investigate each elastic displacement of each {111} lattice spacing. Still, it was difficult because the spacing at equilibrium is 0.24 nm, and the maximum elastic strain is about 5% at maximum, so the elastic displacement is only less than 10 pm. In fact, the elastic displacement of the measured spacing was so broadly scattered from a time-proportional relationship that the ratio of the piezo elongation (ΔL_{piezo}) to the displacement of this local region (Δl_{local}) could not be reasonably determined.

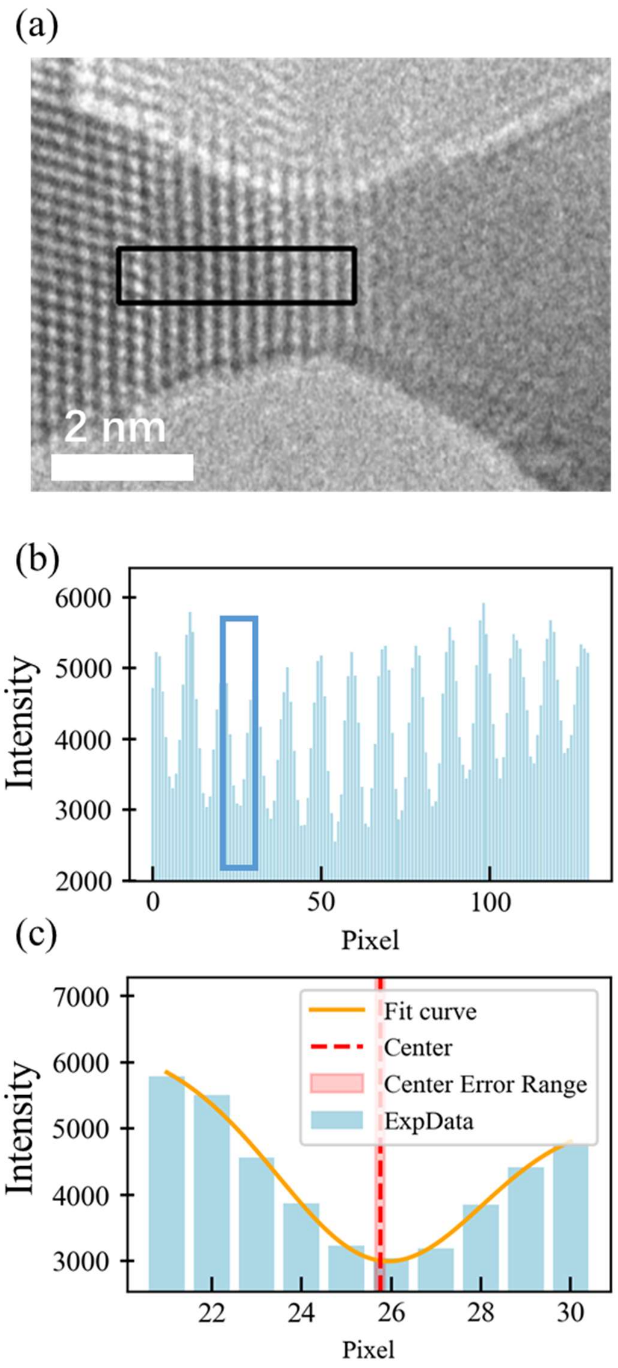

Figure 4.5 Procedure of measuring the {111} lattice plane positions in HRTEM images. (a) A typical TEM image of the Au ⟨111⟩ NC. In the black rectangle area, the average value was taken in the vertical direction to obtain the intensity profile in the horizontal direction. The white scale bar indicates 2 nm. (b) The intensity profile in the horizontal direction in the black rectangle area in (a). The minima (valleys) in the

profile correspond to the positions of individual {111} atomic planes. (c) Magnified view of a single valley (blue box in b), representing one {111} atomic plane. The profile was fitted with an inverted Gaussian function (red dashed line: center of the fitted function, representing the precise atomic plane position; pink regions: uncertainty in the fitted center position).

Figure 4.6(a) shows a typical TEM image of the Au ⟨111⟩ NC. The positions of the {111} lattice planes indicated by the green lines were identified at the sub-pixel level by the program. When the {111} lattice planes were numbered from thickest to thinnest cross-sections, the elastic responses were investigated in the following three regions: 8 to 9 (as region I), 5 to 6 (as region II), and 0 to 5 (as region III), respectively, as indicated by the black arrows from up to bottom in Figure 4.6(a). In these regions, the time evolution of the local interval was measured. Figure 4.6(b) shows the time evolution of the normalized local interval, which was obtained by dividing the measured width of the region by the number of the {111} lattice spacing, as a function of the piezo displacement. In detail, the time evolution in interval of each region was automatically measured from eight consecutive TEM images during the elastic deformation process by developing the program, and plots of eight points for each region were obtained. In Figure 4.6(b), the ratio of the elongation in the local region to the total displacement ($\Delta l_{local}/\Delta L_{piezo}$) was determined to be 0.108, 0.055, and 0.026, respectively, for the region I, II, and III by linear fitting based on the least-squares method, although the displacement in the local spacing was scattered among 8 data for each region. The equivalent spring constant was obtained by averaging the values in the corresponding elastic deformation process (see Figure 4.4(c)).

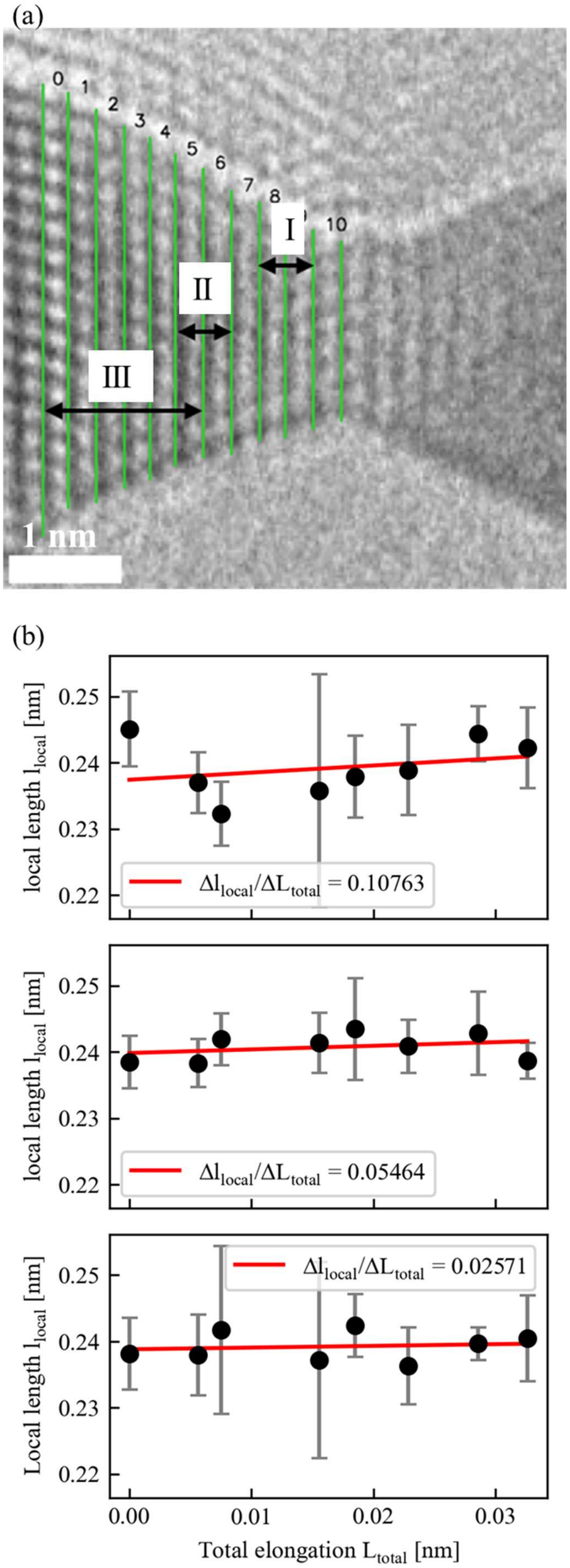
(a)
0
1
2
3
4
5
6
7
8
9
10
I
II
III
1 nm
(b)
local length l_{local} [nm]
0.25
0.24
0.23
0.22
$\Delta l_{local}/\Delta L_{total}$ = 0.10763
local length l_{local} [nm]
$\Delta l_{local}/\Delta L_{total}$ = 0.05464
Local length l_{local} [nm]
$\Delta l_{local}/\Delta L_{total}$ = 0.02571
0.00
0.01
0.02
0.03
Total elongation L_{total} [nm]

Figure 4.6 (a) A typical TEM image of the Au ⟨111⟩ NC, with the {111} lattice planes indicated by the green line. The white scale bar indicates 1 nm. The {111} lattice planes were numbered from thick to thin parts. The black arrows indicate three local regions. (b) The ratio of the elongation in this spacing to the total displacement ($\Delta l_{local}/\Delta L_{piezo}$) for these three local regions in the same elongation process. The red line was obtained by linear fitting to the data.

4.5 Results and discussion

As shown in above sections, the spring constant and local strain have been estimated. Before calculating the local Young's modulus using the equation 4.5, the cross-sectional area of the local region still needs to be estimated. The cross-section of the Au ⟨111⟩ NC, which is necessary to estimate Young’s modulus, was approximated by a triangle with a slight truncation as reported [4]. Since the sharp angle of the hourglass-shaped Au ⟨111⟩ NC is fixed, the cross-sectional areas of the {111} lattice planes that make up the local region are not uniform because of the conical shape. The cross-sectional area of a certain {111} lattice plane can be estimated from the distance from the narrowest constriction by determining the cross-sectional area of the narrowest constriction from the conductance. To obtain Young's modulus in these three regions of the conical shape, Young's modulus was assumed to be constant in each region. To obtain Young's modulus, it is necessary to assume that this region is a cylinder and determine its length and average cross-sectional area. Considering that the equivalent spring constant of this local region is expressed as a series coupling of the equivalent spring constants of these {111} lattice “slices” (S_i), the average cross-sectional area (S_{local}) is obtained as follows:

$$\frac{1}{S_{local}} = \frac{1}{n}\sum_{i}^{n}\frac{1}{S_i} \quad 4.6$$

Based on equation 4.6, the average cross-sectional area was 1.5, 2.5, and 4.0 nm^2 for regions I, II, and III, respectively. Therefore, the Young’s modulus of this local region was estimated to be 54 GPa, 63 GPa, and 83 GPa, respectively, for the three regions by substituting these values in equation 4.5. This indicates that Young’s modulus of the Au ⟨111⟩ NC decreased with decreasing diameter, which was in agreement with the previous result [4].

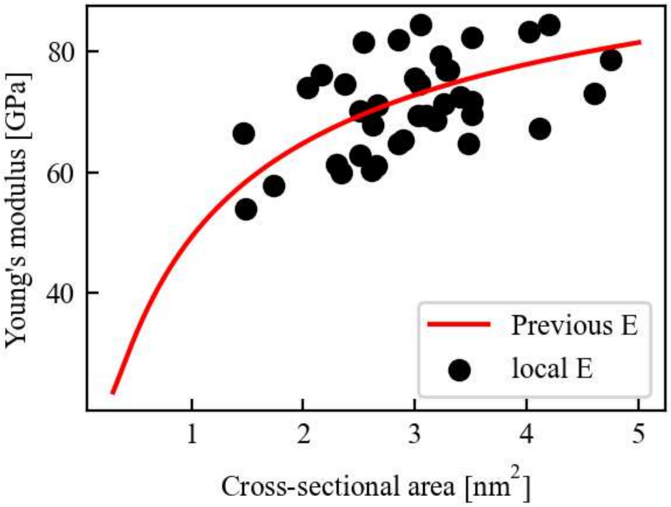

Figure 4.7 Young’s modulus of the Au ⟨111⟩ NC as a function of the cross-sectional area. Black dots represent the estimated local Young’s modulus in this experiment. The red curve represents the size dependence of Young's modulus obtained from previous studies [4].

The Young's moduli of the Au ⟨111⟩ NCs were also estimated in some local regions for each of nine different elastic stretching processes for checking reproducibility.

Figure 4.7 summarizes the Young’s modulus estimated at local regions in different elastic deformation processes. In Figure 4.7, the data points of (average cross-sectional area, Young's modulus) which were obtained in the three local regions as mentioned above were plotted as (1.5 nm^2, 54 GPa), (2.5 nm^2, 63 GPa) and (4.0 nm^2, 83 GPa), respectively. Even though the range of the average cross-sectional area is limited to 1.5 to 5 nm^2, the Young’s modulus shows a tendency to decrease with decreasing the cross-sectional area.

Previously, Zhang et al. found that Young's modulus of Au ⟨111⟩ NCs exhibited a decreasing trend with decreasing cross-sectional area, with the modulus approaching 80 GPa for cross-sectional areas below 4 nm^2 and reducing to around 60 GPa as the cross-sectional area decreased to 2 nm^2 as indicated by the red curve in Figure 4.7 [4]. This curve was obtained by assuming that Young’s modulus at the core and surface of the cross-section were 119 GPa and 22 GPa, respectively. Our estimated Young’s modulus was scattered but had a similar trend to that previously reported.

It has been pointed out that below 10 nm in diameter, the mechanical properties differ from those of the bulk due to surface effects. Theoretically, it is not clear whether the Young's modulus due to surface effects can be higher or lower depending on the pseudopotential used in calculation [16]. It has also been pointed out that the effect of temperature cannot be neglected. Assuming absolute zero temperature, as in first-principles calculations, Young's modulus is shown to be higher due to surface effects. On the other hand, at room temperature, entropy must be taken into account, and Young's modulus decreases due to surface effects [51]. Experimentally, the Young's modulus of gold NCs smaller than 10 nm in diameter has not been systematically evaluated except for the reports mentioned above. Notice that the surface effect on Young's modulus of nanocontacts remains controversial.

To improve the accuracy of the estimation of local Young's modulus of nanomaterials, it is important to recognize the three-dimensional (3D) shape of the NC; TEM simply provides the projected information on the sample depth. Meanwhile, it is known that when the diameter of the NC is less than 5 nm, electrical conduction depends on the number of conduction channels in discrete states. This means that the minimum cross-sectional area of the NC, which is proportional to the number of channels, can be determined. It is also obvious that the geometry of the NC should consist of surface indices with the lowest possible surface energy, since surface effects are dominant. From these two pieces of information, the 3D shape of the NC can be estimated. If this is not the case, energy loss spectroscopy can be used to estimate the thickness of the irradiated region by measuring the ratio of incident electrons to inelastic electrons. By combining this technique with scanning transmission electron microscopy, a thickness map can be obtained to estimate the 3D shape of the nanomaterial. By such technical improvements, the present method is expected to be utilized in the future, as it can appropriately evaluate size and orientation dependences of Young's modulus on the nanoscale.

The elastic properties of nanomaterials have been estimated using stretching or bending tests and AFM. However, any method of measuring mechanical properties detects the mechanical response of the whole, including the target nanomaterial and its supporting materials; it is impossible to obtain the mechanical response of the nanomaterial alone. This means that it is imperative to eliminate any influence from the supporting materials. Recently, the spring constant of the atomic chain has been obtained by removing the contribution of the electrode supporting the atomic chain, which could be achieved by measuring the spring constants of Pt atomic chains of different lengths supported between electrodes of the same geometry [52]. Also, the equivalent spring constant of the nanomaterial alone could be obtained by assuming the bulk value of Young's modulus and calculating the equivalent spring constant of the electrode that supported it [53]. Compared to these methods, our proposed method has the advantage that it requires only several atomically resolved TEM images during the process of elastic deformation to obtain Young's modulus in a certain region.

Recently, Y. Bu et al. reported that the local atomic environment inhomogeneity was related to amorphization process in high-entropy alloys (HEAs). The method for measuring the local Young's modulus proposed in this study is expected to be applied to further research on the local physical and mechanical properties of HEAs [54]. The mechanical properties of structurally heterogeneous materials such as HEAs have attracted much interest. Measurements from a macroscopic point of view have been achieved, while those from a nanoscale point of view have rarely been done. However, because material fracture starts locally, it is important to reveal the mechanical properties of such materials from a nanoscale point of view. The present proposed method would be one of the powerful tools to clarify local mechanical properties.

Young's modulus of a local area could be determined by obtaining the ratio of local elongation measured in the TEM images to the total displacement estimated by the bias voltage applied to the piezo when using the MNMM. However, as shown in Figure 4.6, the local displacements in the seven or eight TEM images, which were retrieved during the stretching process, often deviated from a linear relationship to the total displacement. For thin or relatively long regions where the spring constant was low, this deviation tended to be small because of relatively large elongation, and thus, Young's modulus seemed to be estimated with high accuracy. It means that the spatial resolution of the TEM images should be crucial. In this sense, an aberration-corrected TEM effectively reduces the deviation in the measurement of the elongation of a certain region during the stretching process, resulting in estimating Young's modulus with higher accuracy. In the near future, using aberration-corrected TEM, we expect that our proposed method will allow us to determine Young’s modulus of various nanomaterials more precisely.

4.6 Conclusion

We proposed a new method to measure Young's modulus of nanomaterials. By taking the TEM images simultaneously with measuring the spring constant using the MMNM, the equivalent spring constant of a local region can be obtained by determining the ratio of the displacement of the region to the total displacement of the nanomaterial and its supporting bases on both sides. The Young's modulus can be estimated by considering the cross-section and length of this region. The Young's modulus of the local region in the Au⟨111⟩NC was estimated by applying this method, which showed a similar size dependence of the Young's modulus as reported previously. This method is promising because it can reveal the mechanical properties of structurally heterogeneous materials such as HEAs from a local perspective. Thus, it is expected that the accuracy of this method will be improved in the near future by using aberration-corrected TEM.

Chapter 5 Plastic properties of Au nanocontacts

In section 5.1 we introduce the background of investigating critical resolved shear stress (CRSS), including its definition and function in nanomaterial deformation. Section 5.2 presents the method and results of estimating the yield stress in the loading direction. This section presents the experimental procedure and raw data obtained by varying LER oscillation amplitude, and details the method of estimating the specimen's energy dissipation using the LER driving voltage. Section 5.3 introduces the estimation of CRSS for Au NCs using the yield stress and the slip system. Section 5.4 presents the CRSS results obtained from the experimental results, discussing them with previous experimental and theoretical results. Section 5.5 provides a summary of this chapter.

5.1 Critical resolved shear stress (CRSS)

Critical Resolved Shear Stress (CRSS) is the threshold stress required to start slip deformation in a material. As shown in Figure 5.1(a), when an external loading stress (σ) is applied along the direction indicated by the green arrow, a corresponding resolved shear stress (τ) develops on the slip plane (gray plane) along the slip direction (red arrow). Slip deformation occurs when the resolved shear stress satisfies the condition: $\tau \geqslant$ CRSS (as shown in Figure 5.1(b)).

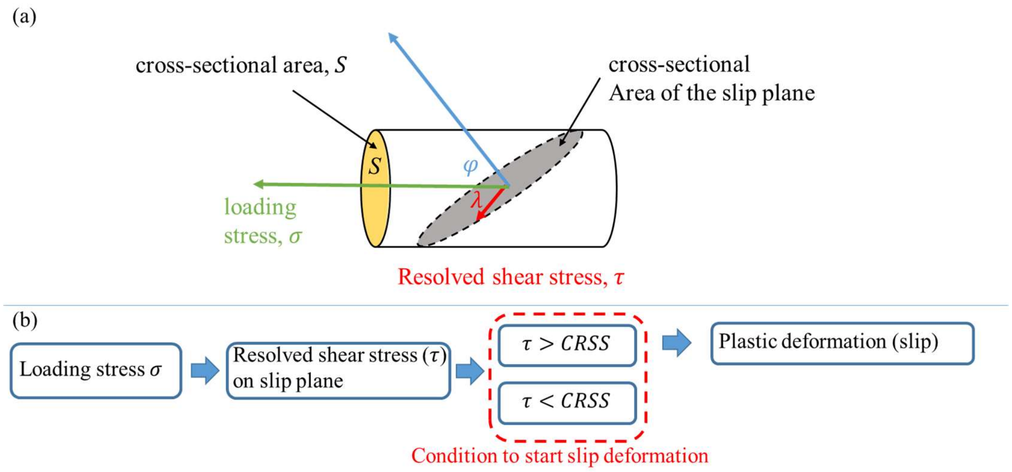

Figure 5.1 The critical resolved stress is the necessary stress on the slip direction to start slip deformation. (a) The geometric relationship between loading stress(σ) and resolved shear stress(τ). (b) process of simultaneously shifting the upper part of a crystal.

The CRSS is an intrinsic property of the material, determined by factors such as crystal structure, temperature, and defect density, and is independent of the external loading direction. In contrast, the critical yield strength (i.e., the applied stress required to trigger plasticity) depends on both the CRSS and the geometric orientation of the slip system relative to the loading direction. When the resolved shear stress on the slip system reaches the critical value (CRSS), dislocations begin to glide, marking the onset of plastic deformation. The relationship between yield stress (normal stress) and CRSS is discussed in more detail in Section 5.3.1.

5.2 Estimation of yield stress

In this study, our purpose is measurement of the CRSS in the slip deformation. To achieve this purpose, it is first necessary to determine the yield point of the material, defined as the critical load in the direction of the applied force (green arrow in Figure 5.1(a)) that plastic deformation begins. This critical load is commonly termed the yield stress. The reason we beginning with the measurement of yield stress lies in its direct. By measuring the yield stress, the CRSS in the slip direction can be effectively derived from the yield stress, if the geometric relationship between the loading direction and the slip system CRSS.

Our specimen is in perfect crystal, its primary mechanism of plastic deformation is slipping deformation. During slip deformation, the yielding behavior of the material is governed by the stresses acting on the slip plane along the slip direction. Crucially, the CRSS and the yield stress are linked through geometric relationships intrinsic to the slip system. By measuring the yield stress in the direction of the loading force, we can estimate the CRSS using these geometric relationships. On the other hand, since metallic nanocontacts with size of only a few nanometers can be regarded as nearly perfect crystals with almost no defects, it is expected to have CSS values close to the ideal values[55,56].

At a scale of 10nm or less, it is very difficult to directly measure the loading stress. As shown in Figure 5.2(a) and (b), J. Comtet et al. fabricated gold nanojunctions between a tuning fork and a gold substrate[57]. In this experiment, the oscillation of the tuning fork essentially constitutes a periodic compressive-tensile dynamic loading process on the gold nanojunction. They used a piezo dither to excite the tuning fork, the periodic force applied on tuning fork is $F^* = Fe^{i\omega t}$.The oscillation of tuning fork is described as $a^* = ae^{i\omega t+\phi}$. They defined the complex mechanical impedance $Z^* = \frac{F^*}{a^*} = (\frac{F}{a})e^{-i\phi}$. The imaginary part $Z'' = Im(Z^*)$ characterizes the dissipative response of the Au junction, it can be measured by tracking the piezo driving voltage necessary to keep the oscillation amplitude of the tuning fork constant. When the driving amplitude exceeds the elastic limit of the material, the gold nanojunction undergoes a transition from purely elastic deformation to deformation that includes plastic deformation. This plastic deformation process significantly increases the energy dissipation of the system. As shown in Figure 5.2 (c), the dissipative response (red dots) while increasing the oscillation amplitude. The dissipation was found to suddenly increase at the amplitude of about 160 pm (a_{γ}), corresponding to the elastic limit. This detection method, based on the abrupt change in energy dissipation, provides an effective experimental criterion for precisely determining the yield point of the metallic junction at the nanoscale. However, due to the lack of structural information on the Au nanojunctions, the direction of loading stress could not be determined, making it unable to estimate the CRSS through the geometric relationship between yield stress and CRSS. Therefore, we conducted experiments using our developed TEM holder equipped with LER.

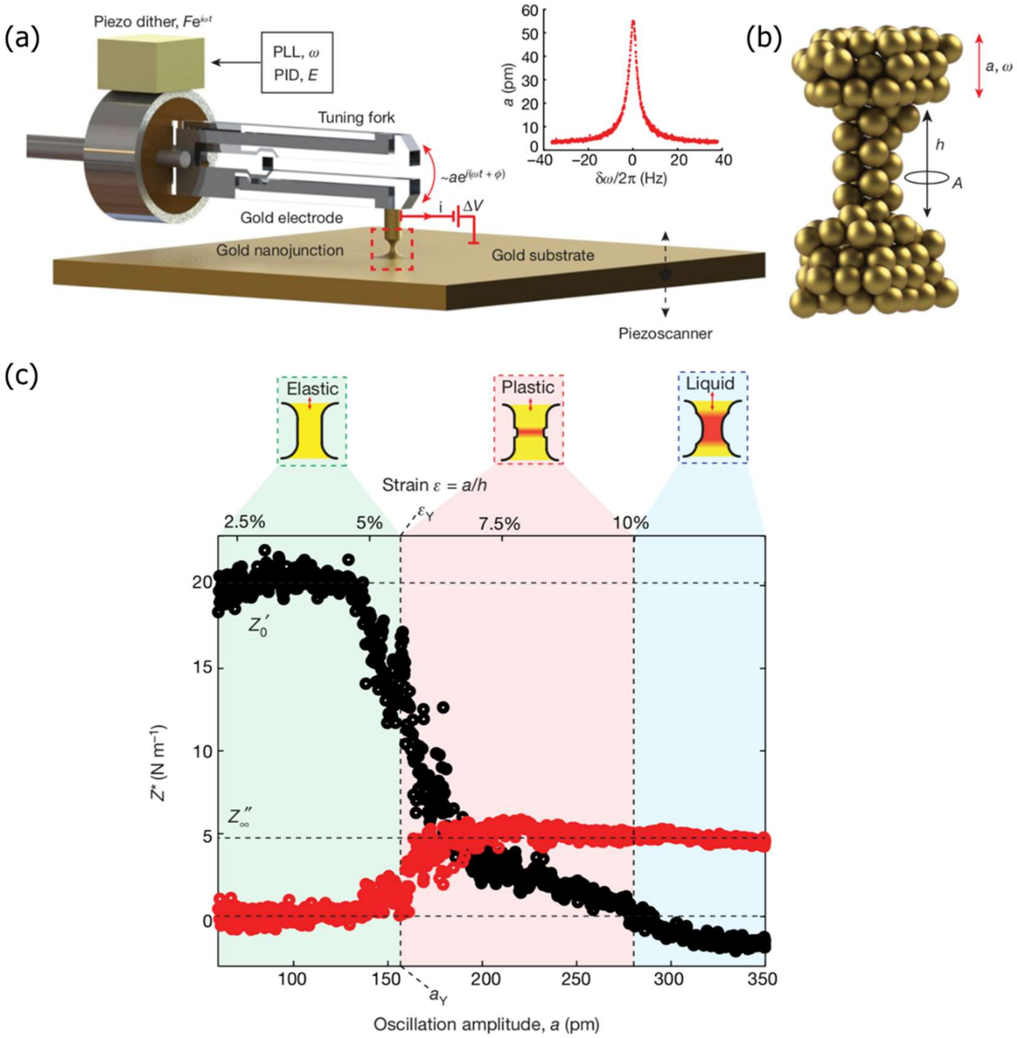

Figure 5.2 (a) Schematic diagram of the experimental setup with a gold nanojunction fabricated between the tip of a tuning fork and a gold electrode. (b) Enlarged schematic view of the gold nanojunction. (c) Amplitude dependence of the complex resistance: the black line represents the real component, and the red line represents the imaginary component.

As mentioned above, we can determine whether or not nanocrystals undergo plastic deformation (e.g., yielding) by measuring the energy dissipation during the deformation process. However, for nanocrystals with dimensions of only a few nanometers, the energy dissipation from a single plastic deformation event is extremely small, making direct measurement highly challenging. Our idea to solve this problem is, we connect the LER oscillator to the nanocrystal, enabling repeated stretching and compression during oscillation. A lock-in amplifier can effectively extract the LER oscillation response signal. The LER oscillates the nanocrystal at 1 MHz, and the sample's the dissipation response is also at 1 MHz. Through phase-sensitive detection (PSD), the lock-in amplifier multiplies the input signal with a 1 MHz reference signal, retaining only the signal components of the same frequency and converting them into low-frequency components. Subsequently, a low-pass filter removes the high-frequency AC components, retaining only the low-frequency components, thereby extracting the target signal. Noise and other frequency interferences become AC signals after PSD and are filtered out by the low-pass filter. Since the lock-in amplifier locks onto the 1 MHz reference frequency, it can precisely extract signals at this frequency, effectively denoising even in environments with strong noise. This mechanism endows it with excellent capability in measuring weak signals, ensuring the accurate extraction of LER oscillation response signals. Response with increasing LER oscillation amplitude

In this study, an experiment was designed to estimate the maximum deformation that a nanocrystal can sustain within its elastic limit, which also called “the yield strain”. A feedback loop was installed to maintain a constant conductance of the nanocrystal (as shown in Figure 5.3(a)), keeping a consistent sample size since the conductance is proportional to the minimum cross-sectional area of the nanocrystal. Based on this setup, we increased the LER oscillation amplitude step-wisely (Figure 5.3(b)), starting from 30 pm, while simultaneously measuring the driving voltage required to excite the LER oscillation (Figure 5.3(c)) and the equivalent spring constant of the nanocrystal (Figure 5.3(d)). Using the method described in Chapter 2, the energy dissipation introduced from the nanocrystal was estimated by comparing the difference in driving voltage between the LER in free oscillation (unconnected to the nanocrystal) and the LER connected to the nanocrystal.

As shown in the Figure 5.4, we converted the raw data, which was a function of time as shown in Figure 5.3(b) and (c) into a function of the LER amplitude. Figure 5.4(a) shows the relationship of the LER amplitude and the driving voltage required to maintain the LER amplitude constant. The red dashed line represents the driving voltage when the LER is unconnected to the nanocrystal, while the black squares represent the driving voltage when the LER is connected to the nanocrystal. It can be observed that when the LER oscillation amplitude exceeds approximately 110 pm (Amp_C), an additional driving voltage is required when connected to the nanocrystal. Using the formula derived in Chapter 2, the corresponding energy dissipation at each LER oscillation amplitude is calculated, as shown in Figure 5.4(b).

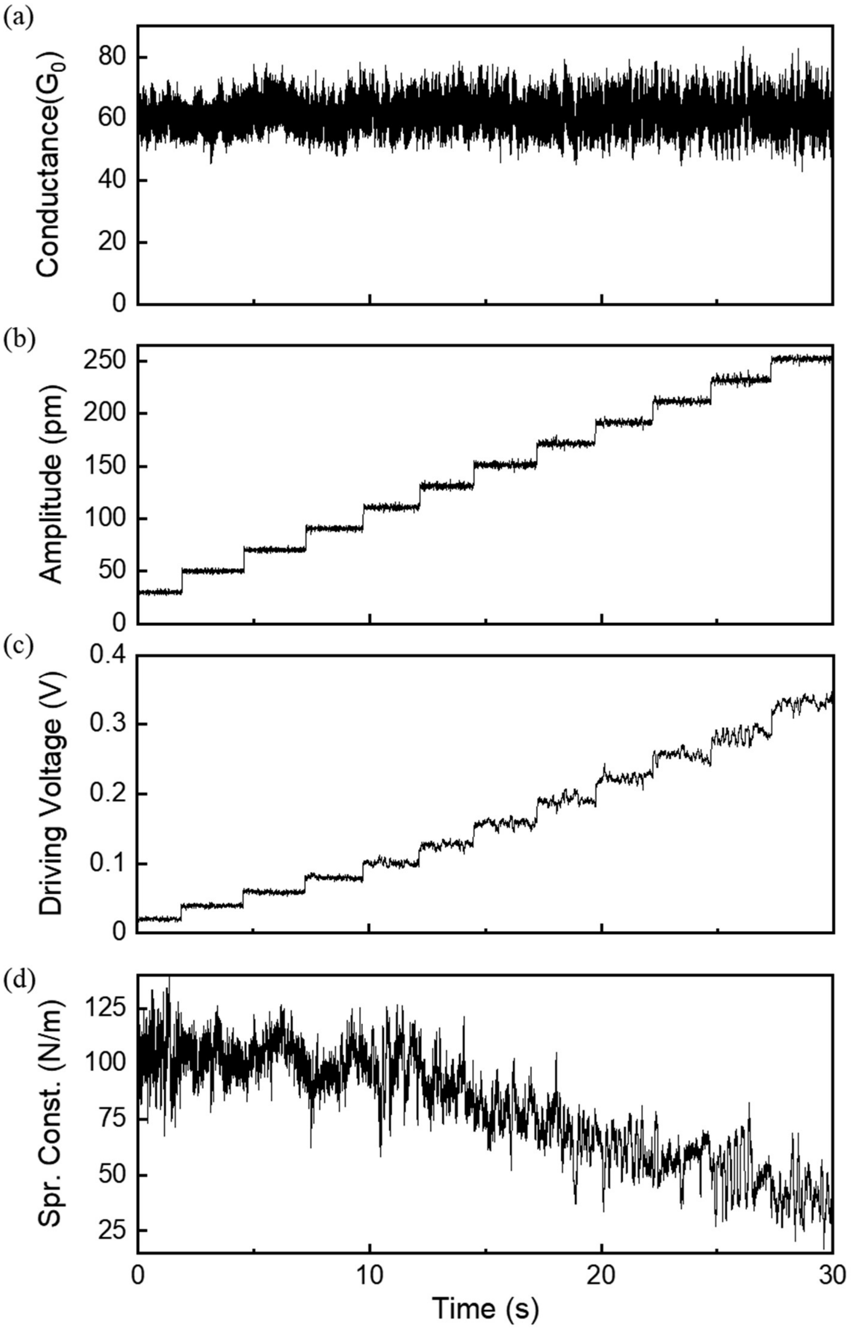

Figure 5.3 (a) Conductance maintained at a constant value. (b) Stepwise increase in the maximum displacement (LER amplitude). (c) (d) Driving voltage and equivalent spring constant corresponding to each value of the maximum displacement (LER amplitude).

When the LER amplitude is below the critical value, Amp_C (indicated by orange region), the energy dissipation under the influence of the LER on the nanocrystal is zero, indicating that only elastic deformation occurs, so we call it as the elastic region. Above Amp_C (indicated by blue region), energy dissipation begins to increase with increasing the LER amplitude, indicating that the nanocrystal undergoes plastic deformation by the LER oscillations. We call it as the plastic region. By gradually increasing the deformation of the nanocrystal and capturing the corresponding energy dissipation, we determined the critical deformation (equal to LER amplitude) at which the nanocrystal yields, denoted as Amp_C.

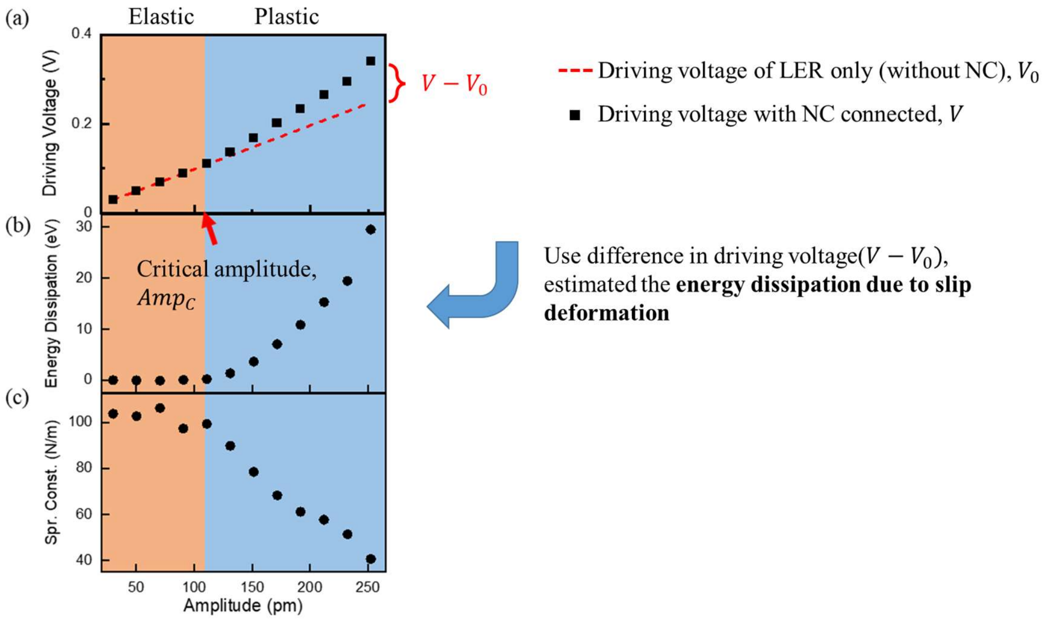

Figure 5.4 (a) Dependence of the driving voltage on the LER oscillation amplitude. (b) Dependence of energy dissipation on the LER oscillation amplitude. (c) Dependence of the equivalent spring constant on the LER oscillation amplitude. Here LER oscillation amplitude is also the displacement of the nanocrystal.

5.2.1 Equivalent spring constant (force gradient)

As mentioned above, by estimating the maximum displacement in the elastic region, the system divides into the elastic region (orange) and the plastic region (blue). As shown in Figure 5.4(d), we measured the equivalent spring constant of Au nanocrystal using the FM method described in Chapter 2. The dependence of the equivalent spring constant on the LER oscillation amplitude (deformation of Au nanocrystal) is shown in Figure 5.4(c). In the elastic region, the equivalent spring constant is almost constant at about 100 N/m. In the plastic region, the equivalent spring constant decreases as the LER oscillation amplitude (maximum displacement) increases. This can be interpreted as the result of the energy that would normally be stored as elastic energy being unable to be stored due to structural relaxation caused by sliding deformation. In other words, we think that the equivalent spring constant has effectively decreased due to the decrease in elastic energy, which is determined by the amplitude and equivalent spring constant.

5.2.2 Quantized conductance and cross-sectional area

In TEM images, only two-dimensional information can be obtained, we cannot get depth information. Therefore, in this study, the minimum cross-sectional area of gold nanocontacts was estimated from their electrical conductance, assuming that electrons pass through such a thin nanocontact ballistically due to quantum confinement effect. Under such an assumption, the conductance G can be given by Landauer's formula, where the transmission coefficient for channel i is denoted by T_i.

$$G = \frac{2e^2}{h}\sum_{i=1}^{n} T_i \qquad 5.1$$

Since the size of metal nanocontacts is shorter than the mean free path of electrons, the effects of scattering can be neglected (ballistic transport), $T_i = 1$. The conductance of the metal nanocontact G_c is given by:

$$G_c = n \times G_0 \tag{5.2}$$

here, n represents the number of channels, and G_0 is the quantum conductance unit defined as $G_0 \equiv 2e^2/h$. In the experiment, a bias voltage of 10 mV was applied to the gold nanocontact, and the measured quantized conductance ,G_c, was analysed using the Sharvin equation, which express the relationship between the number of conductance channels and the minimum cross sectional area of the contact:

$$\mathrm{S} = {\lambda_f}^2 G_c/\pi \tag{5.3}$$

By substituting G_c to equation 5.10, the minimum cross-sectional area can be estimated. Here, λ_f is assumed to be the Fermi wavelength of gold as 0.52 nm.

5.2.3 Results of yield Stress

Assuming that the gold nanocontact is a cylindrical body with a uniform cross-sectional area, the force applied in the tensile direction is:

$$F = kd \tag{5.4}$$

here, k is the equivalent spring constant, and d is the displacement caused by the LER oscillation. Since tensile stress is the force per unit area, we can obtain:

$$\sigma = \frac{F}{S} = \frac{kd}{S} \tag{5.5}$$

When taking the maximum displacement in the elastic region ($d = Amp_c$), the yield stress σ_c is:

$$\sigma_c = \frac{kAmp_c}{S} \tag{5.6}$$

It can be estimated from the three measured values: Amp_c was determined from the amplitude dependence of energy dissipation. The cross-sectional area S was obtained from the conductance values. The equivalent spring constant k was directly obtained from the experimental results.

5.3 Estimation of CRSS for Au nanocontacts

This section determines the CRSS required for slip to occur, based on the geometric relationship between the yield stress σ_c and shear stress.

5.3.1 Geometric relationship between tensile stress and shear stress

When a loading stress is applied to a crystal, then a shear stress will occur on a slip plane. As shown in Figure 5.5, if the angle between the loading stress and the shear stress is λ, then the shear stress is given by $F\cos\lambda$. If the angle between the loading stress and the normal to the slip plane is φ, the area of the slip plane becomes $S/\cos\varphi$. Therefore, the shear stress acting on the slip plane is:

$$\tau = \frac{F\cos\lambda}{\frac{\mathrm{S}}{\cos\varphi}} = \frac{F}{\mathrm{S}}(\cos\lambda\cos\varphi)$$

$$= \sigma(\cos\lambda\cos\varphi) \tag{5.7}$$

here, $\cos\varphi\cos\lambda$ is called as Schmidt’s factor, it is determined by slip system (slip plane and slip direction of the crystal).

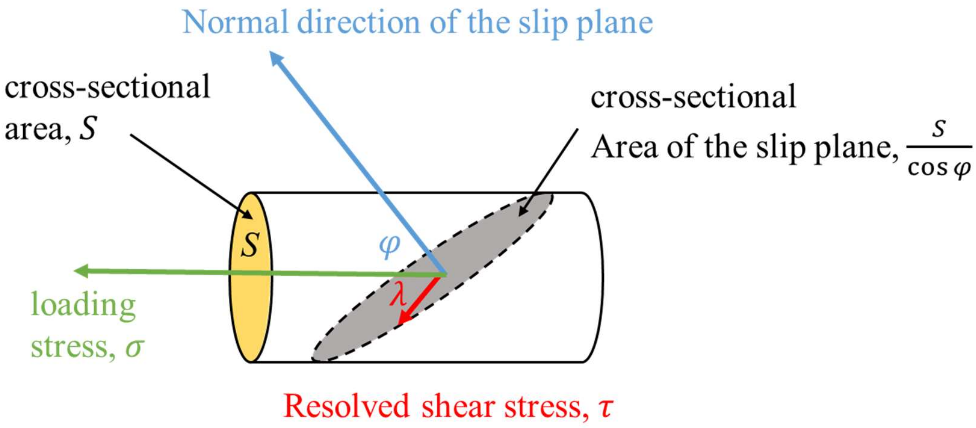

Figure 5.5 Geometric relationship between loading stress and shear stress.

5.3.2 Slip system in nanocrystal

The slip system of a crystal is defined by its slip plane and slip direction. The slip plane is often the crystal plane with the largest interplanar spacing, while the slip direction is the densest direction connecting the closest atoms. In other words, the slip system is determined by the crystal structure. The slip systems of typical metals are shown in Table 5.1.

Lattice type	Typical metals	Slip plane	Slip direction	Number of slip systems
face-centered cubic (fcc)	Au・Ag・Cu	{111}	<110>	4×3=12
body-centered cubic (bcc)	W・α-Fe・Cr	{110} {112} {123}	<111>	6×2=6 12×1=12 24×1=24

Table 5.1 Slip systems of typical metals.

For FCC metallic materials with sizes smaller than a few nanometers, it has been reported that both tensile forces and surface tension act to induce partial slip along the {111} <112> direction[58]. Furthermore, it has been observed that complete slip along {111} <110> occurs through the successive activation of two {111} <112> slips. Therefore, as the gold nanocontacts in this study have diameters ranging from approximately 1.9 nm to 2.6 nm, the slip system can be considered to be {111} <112>.

In the experiment, gold nanocontacts with the axis of the [110] and [111] directions were fabricated. Figure 4.6 shows TEM images of the [110] and [111] gold nanocontacts.

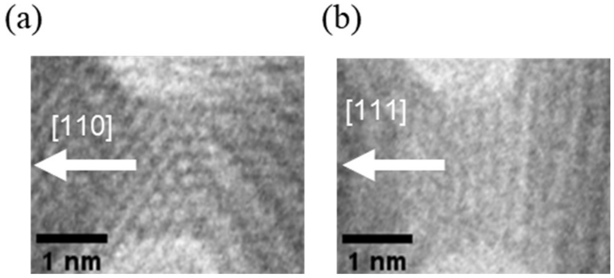

Figure 5.6 TEM images of [110] and [111] gold nanocontacts.

5.4 Results and discussion

5.4.1 Results of this experiment

In the experiment, 4 [110] gold nanocontacts with conductance of 60 G_0, 3 [110] gold nanocontacts with conductance of 30 G_0, and 3 [111] gold nanocontacts with conductance of 30 G_0 were fabricated, and their critical shear stresses were investigated. Figure 5.7 shows the dependence of the equivalent spring constant and the LER oscillation amplitude (maximum displacement) on the driving voltage. From the driving voltage, the energy dissipation per oscillation cycle was summarized in Figure 4.8(the method for estimating dissipation energy is described in section2.3).

Table 4.2 presents the maximum displacement in the elastic region determined from the dependence of energy dissipation on the LER oscillation amplitude (maximum displacement), along with the equivalent spring constant, cross-sectional area, and estimated yield stress. From the results, the yield stress of the [110] gold nanocontacts with conductance of 60 G_0 and 30 G_0 was 2.0 ± 0.1 GPa, regardless of size. In contrast, the yield stress of the [111] gold nanocontacts with conductance of 30 G_0 was 3.0 ± 0.1 GPa.

The Schmid factor for the [110] gold nanocontacts is $\sqrt{2}/3$ (= 0.47), and from Equation 5.13, the CRSS was calculated as 0.94 ± 0.1 GPa. Similarly, for [111] gold nanocontacts, the Schmid factor is $2\sqrt{2}/9$ (= 0.31), yielding an estimated critical shear stress of 0.94 ± 0.1 GPa. The CRSS is an inherent property of the material. From two different directions, we obtained consistent CRSS of 0.94GPa, proved the reliability of our method.

(a) Au <110> NC of 60 G_0 in conductance

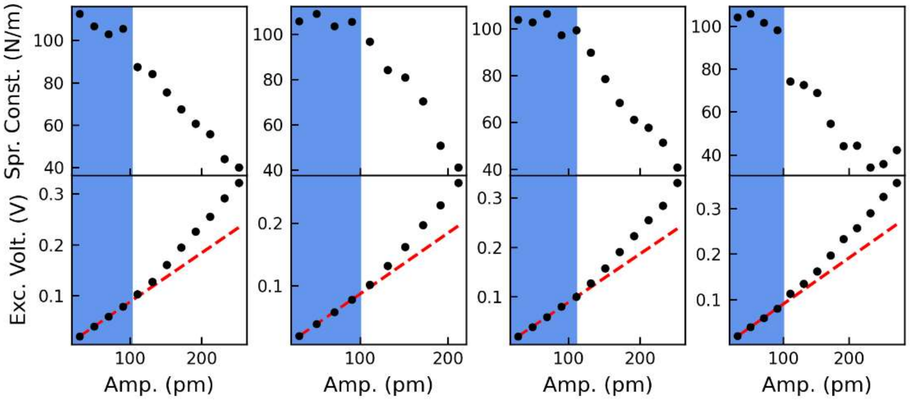

(b) Au <110> NC of 30 G_0 in conductance

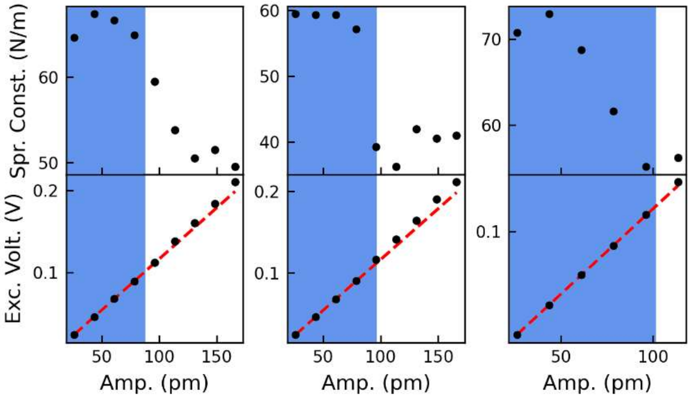

(c) Au <111> NC of 30 G_0 in conductance

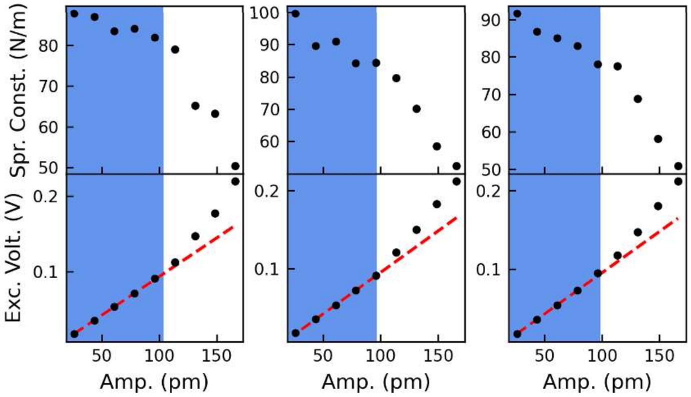

Figure 5.7 Graph of the LER amplitude dependence of additional energy dissipation per oscillation cycle (E_{diss}) and measured spring constant for different Au NCs.

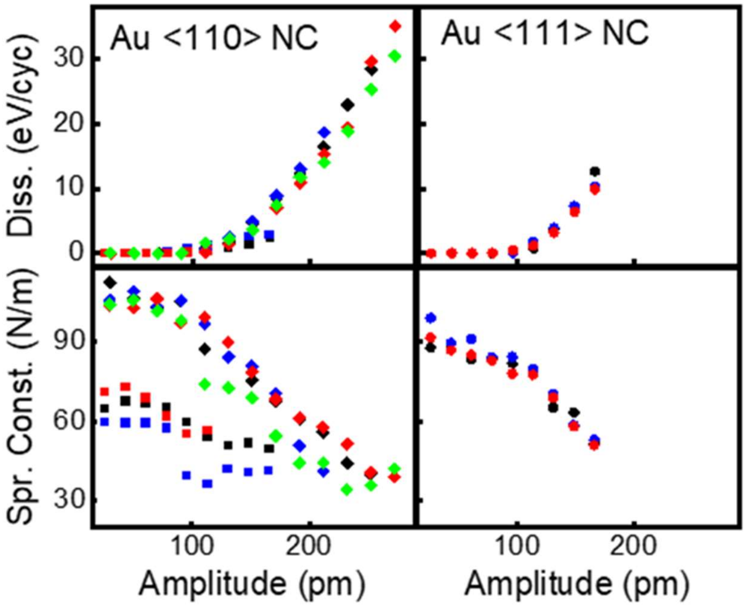

Figure 5.8 Graph of the LER amplitude dependence of additional energy dissipation per oscillation cycle (E_{diss}) and measured spring constant for different Au NCs. Three Au <110> NCs of 30 G_0 are denoted by the colored squares, four Au <110> NCs of 60 G_0 by the colored diamonds, and three Au <111> NCs of 30 G_0 are denoted by the colored circles.

orientation	S (nm^2)	A_c (pm)	k_m (N/m)	yield stress σ (GPa)
<110>	2.9	87	64	1.9
<110>	3.0	96	59	1.9
<110>	2.9	101	59	2.1
<110>	5.4	103	107	2.0
<110>	5.3	100	106	2.0
<110>	5.3	111	102	2.1
<110>	5.2	100	102	2.0
<111>	2.9	103	85	3.0
<111>	2.9	96	91	3.0
<111>	2.9	98	87	3.0

Table 5.2 The cross-sectional area, maximum elastic displacement, spring constant,

and estimated yield stress of gold nanocontacts.

5.4.2 CRSS from previous researches

Previous research has investigated the CRSS of Au nanomaterials using both experimental and theoretical approaches. Heyer et al. fabricated the microshear specimen as shown in the Figure 5.9(a), experimentally investigated the critical shear stress of µm-scale Au single crystal[59]. As illustrated in Figure 5.9(b), when a punch compress on the central part of the Au single crystal, its both sides will have shear deformation. The measured shear stress-displacement curve during the compression process is presented in Figure 5.9(c). For Au single crystals at the µm-scale, the critical shear stress was estimated to be 63.5 MPa experimentally. Geer et al. fabricated submicron-scale single-crystalline Au pillars with the axis of a <001> orientation from single Au crystal. They investigated the stress-strain behavior of these pillars under compression. During testing, as illustrated in Figure 5.10(a), the axial compression induces shear deformation along {111}-type planes. The corresponding stress-strain responses were obtained as shown in Figure 5.10(b). Their results revealed that the critical shear stress for slip initiation on {111} planes in the rage of several hundred MPa.

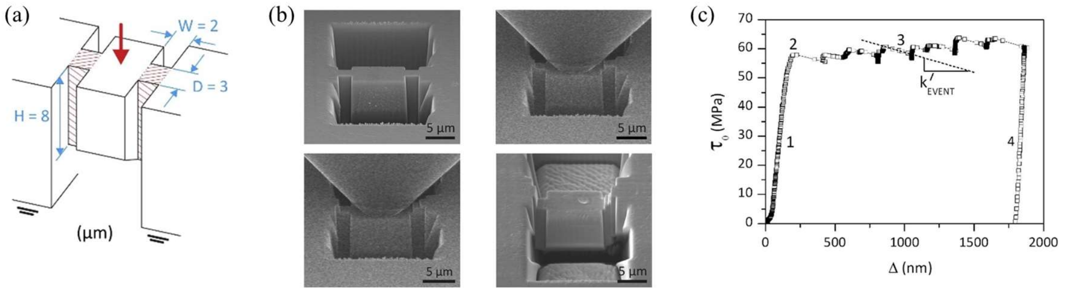

Figure 5.9 (a) Schematic of the microshear specimen produced by Heyer et al. (b)

The SEM image of the process of using a punch to compress the microshear specimen. (c)Stress-displacement curve[59].

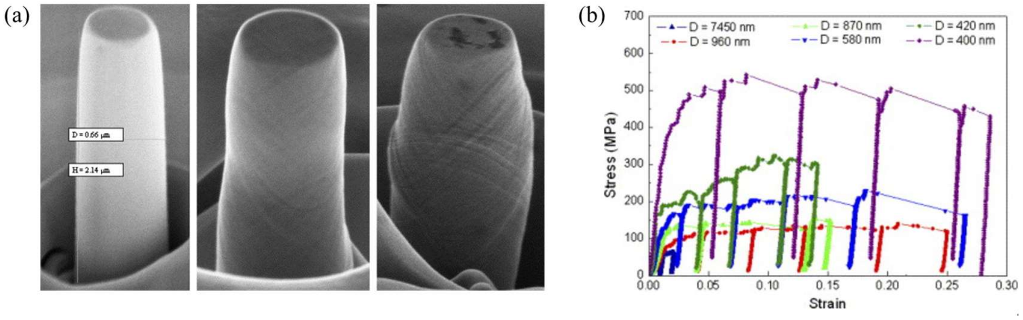

Figure 5.10 (a) SEM images of submicron-scale single-crystalline gold pillars with a <001> orientation Slip lines are clearly present in the deformed states. (b) The corresponding stress-strain curve during compression.

Theoretically, the shear stress for the slip along the $[11\bar{2}]$ direction on the (111) surface,[60] corresponding to CRSS, was predicted to be 1.73 or 1.78 GPa by molecular dynamics (MD) calculations with the embedded atom method (EAM) Au potential[11,61], while it was predicted to be 1.42 GPa by first principle calculation[62]. The CRSS of the Au NCs with dimeters of 1.9 and 2.6 nm was estimated to be 0.94±0.1GPa in this work. which were smaller than such theoretical values. This difference may be explained by the temperature effect. Iskandarov et al. reported that the CRSS of Cu crystal was about 75% at 300 K and about 50% at 800 K relative to the value at 0 K by MD calculations [70]. In our measurement, the Au NC was oscillated along the axis direction above the critical amplitude at 1 MHz of the resonance frequency of LER, and the slip probably occurs continuously during the measurement. The temperature at the Au NC might be raised by heat generated by the slip considerably, resulting in reducing the CRSS value.

5.4.3 Simple estimation of CRSS

The assumption for perfect crystal is all atoms on both sides of a slip plane undergo simultaneous sliding. As shown in , the slip deformation finish in one step. The atomic bonds on both sides of the slip plane break and reform simultaneously, which requires a significant amount of energy for slip to occur, resulting in a high shear stress for a perfect crystal.

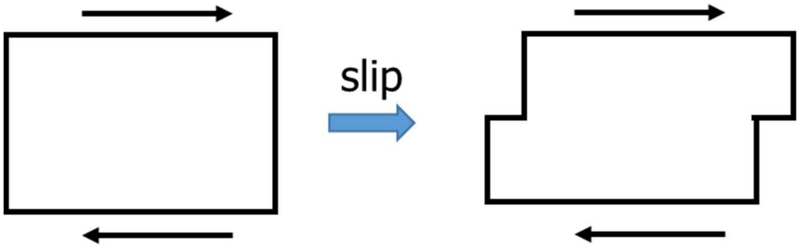

Figure 5.11 Schematic diagram of slip in a perfect crystal. In a perfect crystal, slip is accomplished in only one step.

For a crystal lattice, if a unit crystal has a structure that can be repeated perfectly, then we defined it as perfect crystal. In perfect crystals, the mechanism of plastic deformation typically involves slip deformation occurring on close-packed planes.

Next, we discuss the forces acting on atoms on both sides of the slip plane and estimate the CRSS in an ideal case. As shown in Figure 5.12 from (a) to (b) to (c), it represents the shear stress required to slip the upper part. In the process that the upper part slip by x relative to the down part, Figure 5.12(d) shows the relationship between the necessary shear stress τ and the slip dislocation x. In the states shown in Figure 5.12(a) and (c), the upper and lower part are at equilibrium positions, so the shear stress τ is zero. During the transition from Figure 5.12 (a) to (b), the upper part tends to return to the equilibrium position (a), so τ takes a positive value to counter this tendency. This process corresponds to the displacement range $0 \leqslant x \leqslant d/2$ in Figure 5.12(d). During the transition from Figure 5.12(b) to (c), the upper structure easily tends toward the equilibrium position (c), so a reverse force is needed to counter this, and τ takes a negative value. This process corresponds to the displacement range $d/2 \leqslant x \leqslant d$ in Figure 5.12(d). The intermediate state (b) is also an unstable position, where τ switchs from positive to negative, so $\tau = 0$.

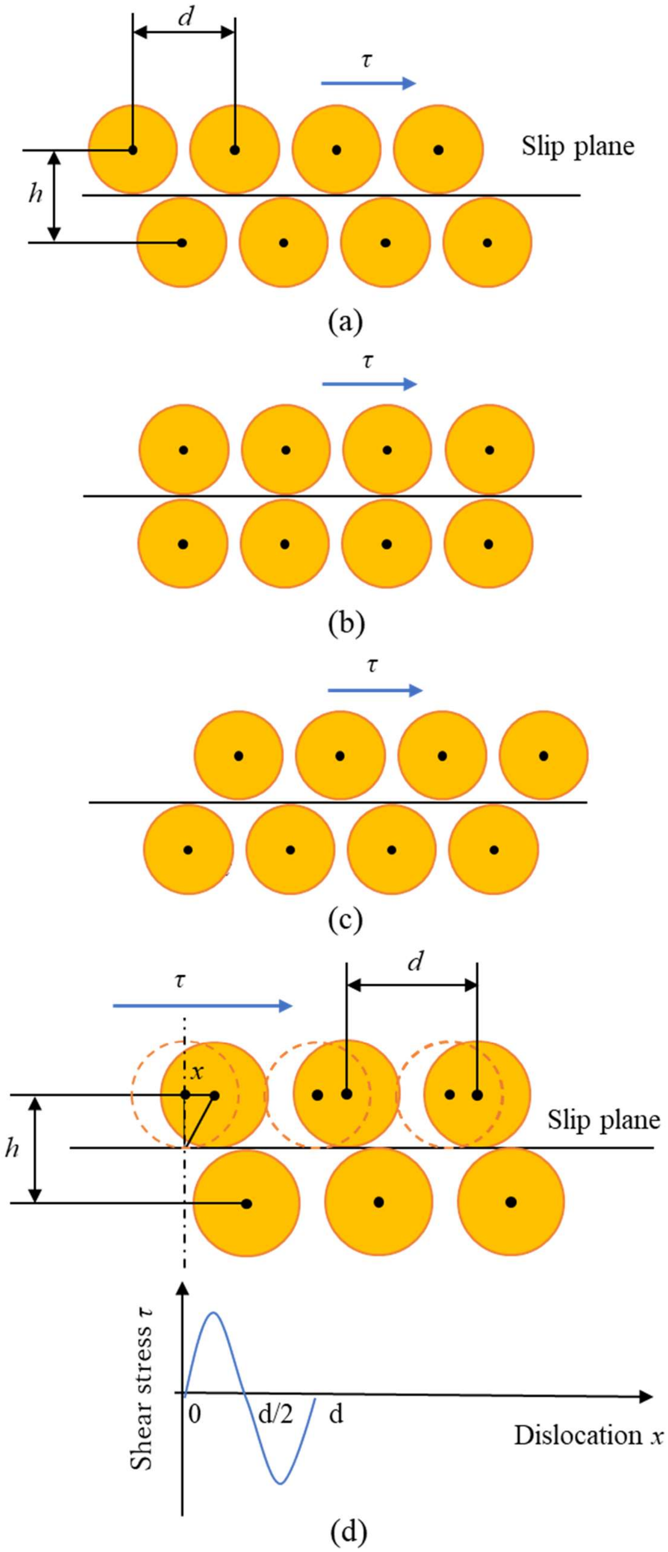

Figure 5.12 The process of simultaneously shifting the upper part of a crystal.

For simplicity, to satisfy the conditions described in the previous paragraph, we assume the relationship between shear stress τ and displacement x follows a sine function as below:

$$\tau = \quad k \sin\left(\frac{2\pi x}{d}\right) \tag{5.8}$$

if we take the distance between the upper and down atomic planes as h, and the displacement x is small enough, then due to Hooke's law, we can describe the shear modulus as:

$$\tau = G\frac{x}{h} = k\frac{2\pi x}{d} \tag{5.9}$$

we can obtain the spring constant:

$$k = \frac{d}{h}\frac{G}{2\pi} \tag{5.10}$$

from above equations, the shear stress is:

$$\tau = \frac{d}{h}\frac{G}{2\pi}\sin\left(\frac{2\pi x}{d}\right) \tag{5.11}$$

for the upper part to entirely slip to the next equilibrium position, the applied stress must exceed the maximum value of this shear stress, otherwise, once the applied stress is released, the upper part will return to its original position. The CRSS required to complete the slip can be determined as the maximum value from equation 5.12:

$$\tau_c = \frac{d}{h}\frac{G}{2\pi} \tag{5.12}$$

Approximately, use $d \approx h$:

$$\tau_c = \frac{G}{2\pi} \tag{5.13}$$

Furthermore, by approximating $\pi \approx 3$, the CRSS can be estimated as 1/6 of the shear modulus. In other words, for a perfect crystal the necessary stress for the upper part to slip can be estimated to be 1/6 of the shear modulus. Table 5.3 lists the measured CRSS values for several metals, along with the calculated values derived from the aforementioned model. From Table 5.3, it can be observed that the CRSS obtained from experiments are 2 to 3 orders of magnitude lower than the theoretical values.

metal	Shear modulus G[GPa]	Critical resolved shear stress [GPa]		The ratio of calculated value to measured value
		G/6	Measured value	
Au	27.6	4.6	0.0009	5100
Ag	28.8	4.9	0.0003	12900
Cu	45.5	7.5	0.0005	15400

Table 5.3 Calculated and measured values of the critical shear stress

5.4.4 Influence of dislocations on the CRSS of crystals

However, the actual measured yield strength was found to be 3 to 4 orders of magnitude lower than the theoretical value. This discrepancy was resolved in 1934 when Taylor and other scientists proposed that the slip process in crystals occurs through the movement of dislocations (Figure 5.13)[63]. Dislocations can begin to move under relatively low stress, causing the slip region to gradually expand until all atoms on the slip plane sequentially undergo relative displacement. This mechanism explains why real crystals require only very low shear stress to initiate slip.

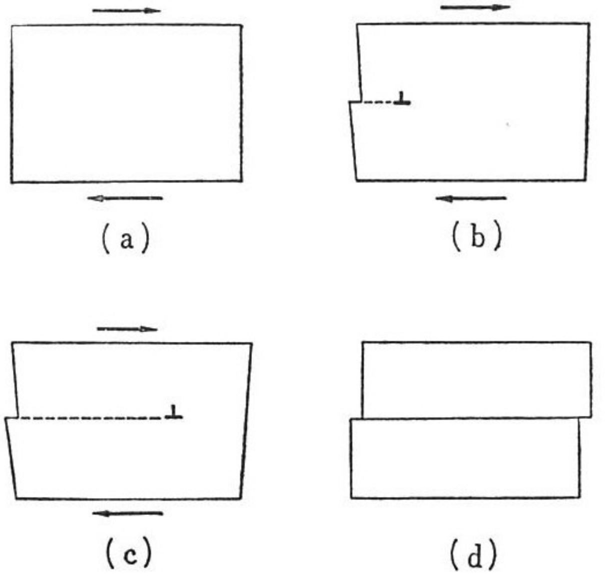

Figure 5.13 Slip process in crystals occurs through the movement of dislocations.

Lastly, we estimate the slip dissipation per oscillation cycle by using a simple model for the shear force exhibiting a curve as a function of the displacement caused by the LER oscillation. We roughly consider the stress-strain curve acting on the nanocrystal during one oscillation cycle. As shown in Figure 5.14, when the LER oscillates within the elastic region, the displacement remains smaller than the maximum elastic strain (ε_C), and the stress-strain curve follows path AD during a single oscillation cycle. However, once the displacement exceeds the maximum elastic displacement, plastic deformation occurs within a single oscillation cycle, and the stress-strain curve follows path FBCE. Specifically, after the stress reaches the critical value ε_C (point A), slip begins to occur, and strain continues to increase while the stress remains constant (A-B). At point B, the displacement reaches its amplitude, corresponding to the peak strain, after which the motion reverses, and both stress and strain decrease proportionally (B-C). The shear stress shows similar behavior in the opposite side (compression). In this case, the work done (energy dissipation) in one cycle corresponds to the area enclosed by FBCE. In fact, the energy here should be calculated by the area enclosed by the force-displacement curve, while the original graph depicts stress-strain. The force-displacement relationship can be derived from the stress-strain relationship, and for convenience, it will not be discussed separately here. This model was obtained by similarity to the strain-stress curve reported previously[64]. In summary, when the LER amplitude is below the elastic deformation limit, the shear force remains linearly proportional to the displacement (as indicated by the orange arrow A-D), and thus no hysteresis occurs. However, once the amplitude exceeds the elastic deformation limit, the stress-strain relationship follows the cyclic path of B-C-E-F. In this case, the slip dissipation per oscillation cycle of the LER corresponds to the area enclosed by the displacement-shear force curve. This phenomenon indicates that the introduction of plastic deformation leads to energy dissipation, which is quantified by the hysteresis loop in the force-displacement curve[62,65].

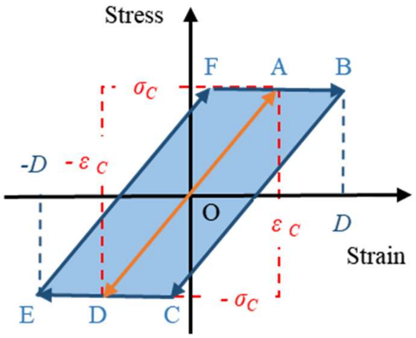

Figure 5.14 Schematic of the stress-strain curve acting on the nanocrystal during one oscillation cycle.

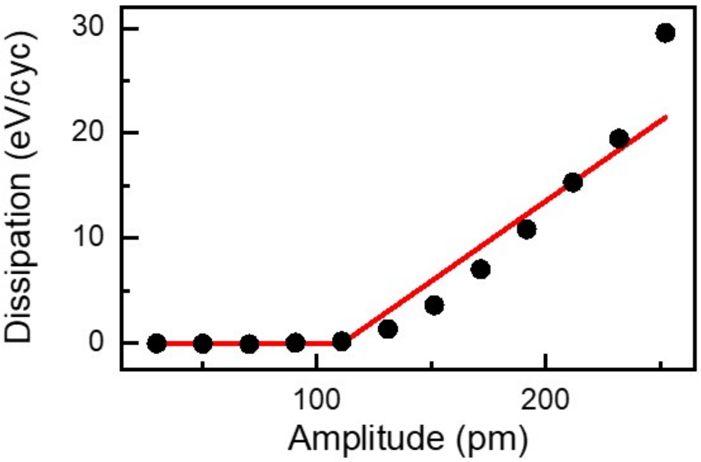

Figure 5.15 Graph of slip dissipation per oscillation cycle as a function of LER amplitude. The black dots correspond to the experimental results, and the red curve is the calculated one based on the simple model in Figure 5.14.

Figure 5.15 shows the amplitude dependence of the slip dissipation. Regardless of simple model, the calculated slip dissipation based on this simple model (red line) reproduces the experimental result well. It supports that the slip continuously occurred on the (111) plane during the LER oscillation above the critical LER amplitude and the CSS value of $0.94 \pm 0.1 \ GPa$ for Au NCs with a few nm in diameter. This study is so worth that it will enable us to understand the mechanism of the plastic deformation (the slip) more deeply by analyzing the dissipation energy using a model that considers the detailed plastic deformation process.

5.5 Conclusion

In this chapter, we investigated the critical resolved shear stress (CRSS) required for slip to occur on the slip plane in a perfect Au crystal. First, Au NC with diameters of less than a few nanometers were prepared by controlling two gold wires to touch together. These NC are our specimen. An LER was used to oscillate the Au NC along the <110> and <111> orientations. This oscillation process is equivalent to repeated tensile and compressive loading, with the maximum tensile and compressive strain equal to the oscillation amplitude. In classical continuous tensile tests, when the maximum strain exceeds the elastic limit, plastic deformation occurs, accompanied by energy dissipation; otherwise, the sample undergoes only elastic deformation with negligible energy dissipation. Similarly, when the oscillation amplitude of the LER exceeds the elastic limit of the Au NC, plastic deformation occurs during oscillation, leading to energy dissipation. Due to the rapid and repeated nature of the oscillations, energy dissipation from plastic deformation continuously accumulates and can be captured by our instrument. Therefore, we use the presence or absence of energy dissipation as a criterion for determining whether plastic deformation has occurred, allowing us to identify the yield point of the sample, including both the yield stress and yield strain.

In the experiment, we estimated the energy dissipation in the specimen through the driving voltage of the LER and estimated the yield stress of the Au NC along the <110> and <111> orientations to be 2.0±0.1 GPa and 3.0±0.1 GPa, respectively. Then, using the slip system of Au, which follows the geometric relationship between loading stress and shear stress in an FCC crystal, we calculated the CRSS required for slip on the {111} plane to be 0.94 GPa. Notably, experiments along the <110> and <111> orientations determined a consistent CRSS of 0.94±0.1 GPa, this result follows the theoretical understanding that CRSS is the fundamental factor governing slip deformation. This further validates the effectiveness of our method.

Chapter 6 Conclusion

This study successfully developed and applied a microscopic nanomechanical measurement method (MNMM) to investigate the elastic and plastic responses of gold nanocontacts (NCs). The local Young's modulus of nanomaterial can be estimated by the ratio of local to the total elongation during elastic deformation. Results from this method also exhibits a size dependence consistent with previous method, validating the method's reliability. Furthermore, we measured the critical resolved shear stress (CRSS) of gold nanocontacts with sizes smaller than 10 nm using a home-made in-situ TEM holder equipped with a quartz length-extension resonator (LER) to detect slip dissipation. The CRSS is an inherent property of the material. From two different directions([110] and [111]), we obtained consistent CRSS of 0.94 ± 0.1 GPa, proved the reliability. The CRSS we observed is higher than the results for sizes greater than 100 nm. I think this difference is due to the presence of dislocations in the larger specimen, which reduced the measured CRSS values.This new method provided valuable insights into the plastic deformation mechanisms at the nanoscale.

This work represents a significant advancement in understanding the mechanical properties of nanomaterials, particularly at the atomic scale, and lays the foundation for future improvements using advanced TEM techniques, such as aberration-corrected TEM, to enhance measurement accuracy and broaden the method's applicability.

Chapter 7 Acknowledgements

I want to express my heartfelt respect and gratitude to Professor Oshima. Since I joined JAIST, Oshima sensei's inspiration and support have been throughout both my master's and doctoral stage. Professor Oshima has guided me with both words and actions, teaching me how to approach research thoughtfully and encouraging me to think critically, take bold experimental steps, and strive for deeper and more rigorous research. His emphasis on hard working and the necessity of even the most repetitive tasks has profoundly shaped my understanding of what it takes to be a researcher. I deeply admire Oshima-sensei's extensive knowledge, vision, and passion for research. He has provided many opportunities for me to present my work, helping me learn how to communicate effectively, tell attractive stories about research, and collaborate with other researchers. Oshima sensei's support and guidance, both academically and personally, have been instrumental in preparing me for future challenges. I am truly grateful for and inspired by Oshima sensei's example and encouragement, which have left a lasting impact on my future development as a researcher.

I would like to express my great gratitude to Professor Tomitori. Tomitori sensei's invaluable guidance was throughout my master's and doctoral studies. Every discussion with Tomitori sensei was a learning experience, filled with insightful advice and perspectives. His profound theoretical knowledge and ability to explain complex concepts with clarity left me deeply impressed. Even when my Japanese was sometimes unclear, he patiently listened and made every effort to understand my points. Tomitori sensei not only provided a high-level overview to help me see the bigger picture of my research but also paid careful attention to detail, offering thorough corrections to my papers and constructive suggestions for my studies. His vivid explanations and practical examples enabled me to quickly grasp challenging formulas and theories, which I deeply admire. I sincerely thank Tomitori sensei.

I sincerely thank Professor Arai of Kanazawa University. Professor Arai has provided me with valuable knowledge and guidance in my research and papers, and I am also very grateful for the valuable suggestions she has offered. Her research on energy dissipation has greatly inspired me, and it will become a key focus of my future work. I am truly thankful for the contributions Professor Arai has made.

I want to express my thank to Professor An. An sensei taught me a lot about measurement techniques and showed me the joy of building measurement systems. Through An sensei, I have meet many friends. His vivid explanations in class deeply captivated me. I am truly grateful for his patient guidance and support in my minor research. His pioneering work in LER has helped me so much.

I also wish to express my heartfelt thanks to Aso sensei, who has provided me with broad guidance, from data analysis and programming and so on even in daily life. I received sincere and thoughtful guidance from Aso sensei, that my study life more interesting. I am truly grateful.

I would like to express my sincere gratitude to my senior, Dr. Zhang Jiaqi. Dr. Zhang despite being busy with his own research, kindly guided me on the use of experimental equipment, sample preparation methods, measurements, and data analysis. When I was learning how to prepare samples, Dr. Zhang patiently observed and guided me, teaching me both the skills for operating the equipment and the advantages of these methods. He also answered my questions with great patient. Through my continued efforts, I hope to become a good researcher under the example like Dr. Zhang. I am deeply grateful for all his support.

I would like to express my thank to my fellow lab mates Dr. Liu, Dr. Xie and Dr. Chen for the kindly discussions and useful ideas when working together.

I want to thank my family. Under their inflution, I have grown the interest for nature word, and thanks to the good and relatively free environment they have given to me. I am grateful to my family for the warmth of home, their integrity, and their attitude of loving life. I also appreciate that my family has helped me grow up accustomed to these valuable qualities, making them an integral part of my life.

Chapter 8 Referrence

[1] Saffarzadeh A, Demir F and Kirczenow G 2018 Thermoelectric voltage switching in gold atomic wire junctions *Phys. Rev. B* **98** 115436

[2] Terabe K, Hasegawa T, Nakayama T and Aono M 2005 Quantized conductance atomic switch *Nature* **433** 47–50

[3] Schirm C, Matt M, Pauly F, Cuevas J C, Nielaba P and Scheer E 2013 A current-driven single-atom memory *Nat. Nanotechnol.* **8** 645–8

[4] Zhang J, Tomitori M, Arai T and Oshima Y 2022 Surface Effect on Young's Modulus of Sub-Two-Nanometer Gold [111] Nanocontacts *PHYSICAL REVIEW LETTERS* **128** 146101

[5] Cui L, Jeong W, Hur S, Matt M, Klöckner J C, Pauly F, Nielaba P, Cuevas J C, Meyhofer E and Reddy P 2017 Quantized thermal transport in single-atom junctions *Science* **355** 1192–5

[6] Jalabert L, Sato T, Ishida T, Fujita H, Chalopin Y and Volz S 2012 Ballistic Thermal Conductance of a Lab-in-a-TEM Made Si Nanojunction *Nano Letters* **12** 5213–7

[7] Yi B, Pang R, Ren X, Guo H, Shang Y, Duan X, Cho J-H and Li S 2020 Phase transition of nanoscale Au atom chains on NiAl(110) *Physics Letters A* **384** 126183

[8] Lagos M J, Sato F, Galvão D S and Ugarte D 2011 Mechanical Deformation of Nanoscale Metal Rods: When Size and Shape Matter *Phys. Rev. Lett.* **106** 055501

[9] Schirm C, Matt M, Pauly F, Cuevas J C, Nielaba P and Scheer E 2013 A current-driven single-atom memory *Nature Nanotech* **8** 645–8

[10] Paul D J 2004 Si/SiGe heterostructures: from material and physics to devices and circuits *Semicond. Sci. Technol.* **19** R75

[11] Diao J, Gall K and Dunn M L 2003 Surface-stress-induced phase transformation in metal nanowires *nature materials* **2** 5

[12] Tosatti E, Prestipino S, Kostlmeier S, Corso A D and Di Tolla F D 2001 String Tension and Stability of Magic Tip-Suspended Nanowires *Science* **291** 288–90

[13] Calvo M R, Sabater C, Dednam W, Lombardi E B, Caturla M J and Untiedt C 2018 Influence of Relativistic Effects on the Contact Formation of Transition Metals *Phys. Rev. Lett.* **120** 076

[14] Wang Y, Li M and Xu J 2017 Mechanical properties of spinodal decomposed metallic glass composites *Scripta Materialia* **135** 41–5

[15] Weinberger C R and Cai W 2012 Plasticity of metal nanowires *J. Mater. Chem.* **22** 3277

[16] Zhou L G and Huang H 2004 Are surfaces elastically softer or stiffer? *Appl. Phys. Lett.* **84** 1940–2

[17] Fujii A, Tsutsui M, Kurokawa S and Sakai A 2005 Break conductance of noble metal contacts *Physical Review B* **72** 045407

[18] Ternes M, Gonz, aacute, lez C, eacute, sar, Lutz C P, Hapala P, Giessibl F J, Jel, iacute, nek P and Heinrich A J 2011 Interplay of Conductance, Force, and Structural Change in Metallic Point Contacts *Physical Review Letters* **106** 016802

[19] Ternes M, Lutz C P, Hirjibehedin C F, Giessibl F J and Heinrich A J 2008 The Force Needed to Move an Atom on a Surface *Science* **319** 1066–9

[20] Xu F, Qin Q, Mishra A, Gu Y and Zhu Y 2010 Mechanical properties of ZnO nanowires under different loading modes *Nano Res.* **3** 271–80

[21] Lee S-W, Han S M and Nix W D 2009 Uniaxial compression of fcc Au nanopillars on an MgO substrate: The effects of prestraining and annealing *Acta Materialia* **57** 4404–15

[22] Greer J R, Oliver W C and Nix W D 2005 Size dependence of mechanical properties of gold at the micron scale in the absence of strain gradients *Acta Materialia* **53** 1821–30

[23] Wu B, Heidelberg A and Boland J J 2005 Mechanical properties of ultrahigh-strength gold nanowires *Nat Mater* **4** 525–9

[24] Hoffmann S, Utke I, Moser B, Michler J, Christiansen S H, Schmidt V, Senz S, Werner P, Gösele U and Ballif C 2006 Measurement of the Bending Strength of Vapor−Liquid−Solid Grown Silicon Nanowires *Nano Lett.* **6** 622–5

[25] Lu Yang, Song Jun, Huang Jian Yu, and Lou Jun 2011 Fracture of Sub-20nm Ultrathin Gold Nanowires *Advanced Functional Materials* **21** 3982–9

[26] Zhang H, Tersoff J, Xu S, Chen H, Zhang Q, Zhang K, Yang Y, Lee C-S, Tu K-N, Li J and Lu Y 2016 Approaching the ideal elastic strain limit in silicon nanowires *Sci Adv* **2**

[27] Pustan M, Paquay S, Rochus V and Golinval J-C 2011 Modeling and finite element analysis of mechanical behavior of flexible MEMS components *Microsyst Technol* **17** 553–62

[28] Fujisawa N, Ogura T and Hirose A 2016 A Method for Studying the Nano-Scale Stress-Strain Response of a Material by Nanoindentation *Mater. Trans.* **57** 1006–9

[29] Broglie L de 1927 La mécanique ondulatoire et la structure atomique de la matière et du rayonnement *J. Phys. Radium* **8** 225–41

[30] de Broglie L 1970 The reinterpretation of wave mechanics *Found Phys* **1** 5–15

[31] Williams D B and Carter C B 2009 *Transmission Electron Microscopy* (Springer US, Boston, MA)

[32] Tanaka N 2017 Structure and Imaging of a Transmission Electron Microscope (TEM) *Electron Nano-Imaging: Basics of Imaging and Diffraction for TEM and STEM* ed N Tanaka (Tokyo: Springer Japan) pp 17–28

[33] Sainath G, Rohith P and Choudhary B K 2017 Size dependent deformation behaviour and dislocation mechanisms in 〈1 0 0〉 Cu nanowires *Philosophical Magazine* **97** 2632–57

[34] Cao H, Rui Z and Yang F 2020 Mechanical properties of Cu nanowires: Effects of cross-sectional area and temperature *Materials Science and Engineering: A* **791** 139644

[35] Shan-Shan L, Yu-Hua W and Zi-Zhong Z 2008 The elastic properties and energy characteristics of Au nanowires: an atomistic simulation study *Chinese Phys. B* **17** 2621–6

[36] Wen Y-H, Zhang Y, Wang Q, Zheng J-C and Zhu Z-Z 2010 Orientation-dependent mechanical properties of Au nanowires under uniaxial loading *Computational Materials Science* **48** 513–9

[37] Nasr Esfahani M and Alaca B E 2019 A Review on Size-Dependent Mechanical Properties of Nanowires *Adv. Eng. Mater.* **21** 1900192

[38] Yao Y and Chen S 2016 Surface effect in the bending of nanowires *Mechanics of Materials* **100** 12–21

[39] Miller R E and Shenoy V B 2000 Size-dependent elastic properties of nanosized structural elements *Nanotechnology* **11** 139–47

[40] Koh S J A and Lee H P 2006 Molecular dynamics simulation of size and strain

rate dependent mechanical response of FCC metallic nanowires *Nanotechnology* **17** 3451

[41] Wang X, Zheng S, Shinzato S, Fang Z, He Y, Zhong L, Wang C, Ogata S and Mao S X 2021 Atomistic processes of surface-diffusion-induced abnormal softening in nanoscale metallic crystals *Nat Commun* **12** 5237

[42] Cuenot S, Frétigny C, Demoustier-Champagne S and Nysten B 2004 Surface tension effect on the mechanical properties of nanomaterials measured by atomic force microscopy *Physical Review B* **69** 165410

[43] Zhu Y, Qin Q, Xu F, Fan F, Ding Y, Zhang T, Wiley B J and Wang Z L 2012 Size effects on elasticity, yielding, and fracture of silver nanowires: In situ experiments *PHYSICAL REVIEW B* 7

[44] Jing G Y, Duan H L, Sun X M, Zhang Z S, Xu J, Li Y D, Wang J X and Yu D P 2006 Surface effects on elastic properties of silver nanowires: Contact atomic-force microscopy *Physical Review B* **73** 235409

[45] Chen C Q, Shi Y, Zhang Y S, Zhu J and Yan Y J 2006 Size Dependence of Young's Modulus in ZnO Nanowires *Phys. Rev. Lett.* **96** 075505

[46] Zhu Y, Xu F, Qin Q, Fung W Y and Lu W 2009 Mechanical Properties of Vapor−Liquid−Solid Synthesized Silicon Nanowires *Nano Lett.* **9** 3934–9

[47] Stan G, Krylyuk S, Davydov A V and Cook R F 2010 Compressive Stress Effect on the Radial Elastic Modulus of Oxidized Si Nanowires *Nano Lett.* **10** 2031–7

[48] Oshima Y, Kurui Y and Takayanagi K 2010 One-by-One Introduction of Single Lattice Planes in a Bottlenecked Gold Contact during Stretching *J. Phys. Soc. Japan* **79** 054702

[49] Oshima Y and Kurui Y 2013 In situ TEM observation of controlled gold contact

failure under electric bias *Physical Review B* **87** 081404

[50] Sharvin Y V 1965 A Possible Method for Studying Fermi Surfaces *Eksp. Teor. Fiz.* **48** 2

[51] Ao Z M, Li S and Jiang Q 2008 The determination of Young's modulus in noble metal nanowires *Appl. Phys. Lett.* **93** 081905

[52] Zhang J, Ishizuka K, Tomitori M, Arai T, Hongo K, Maezono R, Tosatti E and Oshima Y 2021 Peculiar Atomic Bond Nature in Platinum Monatomic Chains *Nano Lett.* **21** 3922–8

[53] Liu C, Hongo K, Maezono R, Zhang J and Oshima Y 2023 Stiffer Bonding of Armchair Edge in Single-Layer Molybdenum Disulfide Nanoribbons *Advanced Science* 2303477

[54] Bu Y, Wu Y, Lei Z, Yuan X, Liu L, Wang P, Liu X, Wu H, Liu J, Wang H, Ritchie R O, Lu Z and Yang W 2024 Elastic strain-induced amorphization in high-entropy alloys *Nat Commun* **15** 4599

[55] Agraït N 2003 Quantum properties of atomic-sized conductors *Physics Reports* **377** 81–279

[56] Xu W and Dávila L P 2017 Size dependence of elastic mechanical properties of nanocrystalline aluminum *Materials Science and Engineering: A* **692** 90–4

[57] Comtet J, Lainé A, Niguès A, Bocquet L and Siria A 2019 Atomic rheology of gold nanojunctions *Nature* **569** 393–7

[58] Diao J, Gall K, Dunn M L and Zimmerman J A 2006 Atomistic simulations of the yielding of gold nanowires *Acta Materialia* **54** 643–53

[59] Heyer J-K, Brinckmann S, Pfetzing-Micklich J and Eggeler G 2014 Microshear deformation of gold single crystals *Acta Materialia* **62** 225–38

[60] Marszalek P E, Greenleaf W J, Li H, Oberhauser A F and Fernandez J M 2000 Atomic force microscopy captures quantized plastic deformation in gold nanowires *Proceedings of the National Academy of Sciences of the United States of America* **97** 6282–6

[61] Deng C and Sansoz F 2009 Near-Ideal Strength in Gold Nanowires Achieved through Microstructural Design *ACS Nano* **3** 3001–8

[62] Ogata S, Li J, Hirosaki N, Shibutani Y and Yip S 2004 Ideal shear strain of metals and ceramics *Phys. Rev. B* **70** 104104

[63] Taylor G I 1997 The mechanism of plastic deformation of crystals. Part I.—Theoretical *Proceedings of the Royal Society of London. Series A, Containing Papers of a Mathematical and Physical Character* **145** 362–87

[64] Liu J, Fan X, Zheng W, Singh D J and Shi Y 2020 Nanocrystalline gold with small size: inverse Hall–Petch between mixed regime and super-soft regime *Philosophical Magazine* **100** 2335–51

[65] Navarro V, de la Fuente O R, Mascaraque A and Rojo J M 2008 Uncommon Dislocation Processes at the Incipient Plasticity of Stepped Gold Surfaces *Phys. Rev. Lett.* **100** 105504

Publications

[1]. J. Liu, J. Zhang, T. Arai, M. Tomitori and Y. Oshima "Critical shear stress of gold nanocontacts estimated by in situ transmission electron microscopy equipped with a quartz length-extension resonator"
Appl. Phys. Express 14 (2021) 075006.

[2]. J. Liu, J. Zhang, K. Aso, T. Arai, M. Tomitori and Y. Oshima "Estimation of local variation in Young's modulus over a gold nanocontact using microscopic

nanomechanical measurement method"
Nanotechnology 36 (2025) 015703.

Presentations

International Conference (Oral)

1. "Critical shear stress of gold nanocontact measured by TEM combined with a quartz resonator", J. Liu, J. Zhang, T. Arai, M. Tomitori, Y. Oshima. The 22nd international vacuum congress (IVC-22), Mon-E1-8, 12th, September, 2022, Sapporo, Japan.
2. "Evolution of local mechanical response of Au nanomaterials measured from dynamic TEM observation", J. Liu, J. Zhang, K. Aso, T. Arai, M. Tomitori, Y. Oshima. The 20th International Microscopy Congress(IMC20), #0499, 12th, September, 2023, Busan, Korea.
3. "Estimation of local Young's modulus in nanomaterials using microscopic nanomechanical measurement method", J. Liu, J. Zhang, K. Aso, T. Arai, M. Tomitori, Y. Oshima. The 10th International Symposium on Surface Science (ISSS10), 3C06, 22nd, October, 2024, Kitakyushu, Japan.

International Conference (Poster)

1. "Critical shear stress of gold nanocontact measured by TEM combined with a quartz resonator", J. Liu, J. Zhang, T. Arai, M. Tomitori, Y. Oshima. The 9th International Symposium on Surface Science, 01PS-26 (Nanotechnology and nanomaterials), 1st, December, 2021, Takamatsu, Japan.
2. "Measurement of critical shear stress of gold nanocontacts by in-situ transmission electron microscopy equipped with a quartz resonator" J. Liu, J. Zhang, T. Arai, M. Tomitori, Y. Oshima. The Material Research Meeting 2021 (MRM2021), D5-PR13-07, 13th, December, 2021, Yokohama.

Domestic Conference (Oral)

1. "Critical shear stress of gold nanocontact measured by TEM combined with a quartz resonator" J. Liu, J. Zhang, T. Arai, M. Tomitori, Y. Oshima. 2021 The 82nd JSAP Autumn Meeting, 13a-N301-5, 13th, September, 2021, Online.
2. "Estimation of Critical Shear Stress of Au nanocontacts using microscopic

nanomechanics measurement method" J. Liu, J. Zhang, T. Arai, M. Tomitori, Y. Oshima. JAIST International symposium of Nano-Materials for Novel Devices, B-15, 11th, January, 2024, Kanazawa.

Domestic Conference (Poster)

1. "水晶振動子を組み込んだ TEM 法による金ナノ接点の臨界せん断応力サイズ依存性の研究" J. Liu, J. Zhang, T. Arai, M. Tomitori, Y. Oshima. 69st Spring Meeting of the Japan Society of Applied Physics, 25p-P03-5, 25th, March, 2022, Aoyama Gakuin University.
2. "Measurement of Local Young's Modulus of Gold Nanomaterials by In-situ TEM Observation" J. Liu, J. Zhang, K. Aso, T. Arai, M. Tomitori, Y. Oshima. The 80th Annual Meeting of the Japanese Society of Microscopy, P-M_47 6, 3rd-5th, June, 2024, Makuhari Messe, Chiba.